Mechanistic Modeling of Cell Signaling Heterogeneity and Chemokine Gradients in Cancer

by

Phillip Spinosa

A dissertation submitted in partial fulfillment
of the requirements for the degree of
Doctor of Philosophy
(Chemical Engineering)
in the University of Michigan
2019

Doctoral Committee:

Professor Jennifer J. Linderman, Chair
Professor Gary D. Luker
Associate Research Scientist Kathryn E. Luker
Associate Professor Sunitha Nagrath
Associate Professor Greg Thurber

Phillip Spinosa
spinospc@umich.edu
ORCID iD: 0000-0002-9353-9085

Acknowledgements

Words cannot fully express my gratitude to my advisor Jennifer Linderman. When I began the graduate program, I had no idea what to expect. I did not have any family or close friends who had gone through similar programs who could speak to the experience. I knew I needed an advisor who could be that support system and train me to think critically. She is a shining example of what it means to be an educator, hard worker, and professional. I will forever be proud to say that I came from her lab.

I am honored to be the inaugural student to put Kathy Luker on my dissertation committee. She is a leader in the lab who knows how to drive students to progress forward in any circumstance. Thank you for your patience in teaching me the ropes of imaging. I am delighted to be an author on your first senior-author publication.

Gary Luker taught me every medical-related fact that I needed to know to be successful here at Michigan. His genuine compassion for his work bled over onto how I view my own. He was a true joy to work alongside, and always willing to prioritize his students.

Greg Thurber and Sunitha Nagrath provided input throughout my graduate work to steer me in fruitful directions. Greg taught a drug distribution course that I will carry with me into my career. Sunitha was always willing to lend an ear when I had questions.

My parents were my foundation who encouraged me along this journey. I would not have had the guts to do this without them telling me I could. They travelled to watch me in many marathons over the past few years, and I was so proud to finish Boston in 2018, drenched, with them at the finish line (with a blanket). They have looked out for my physical and mental health in so many instances that I can never repay them – they are my role models.

Angelo’s support was there whenever I needed it. Both of us made sacrifices for me to get to this point. Whether we were vacationing on a beach, floating down a river, or just enjoying each other’s company, I was happy we were doing it together. I cannot wait to see what the future holds.

Thank you to my friends at Blue Lion Fitness! Being able to forget about science for an hour every morning at 6am was both exhilarating and therapeutic. Now that I am leaving town, who will be the fastest?

For any question about the program or planning of departmental events, Susan Hamlin, Kelly Raickovich, and the rest of the chemical engineering staff were a godsend.

Thank you to my lab mates in both the Linderman and Luker labs, both past and present. The scientific advice, lab banter, and get-togethers made this journey a fun one.

Lastly, to my friend circle I have made here at Michigan, thank you for the countless bouts of emotional support. Genesis, David, Martin, Kathy, and even Joe – the occasional glass of red wine with you made these five years some to remember. To those not named here, I am grateful our paths crossed and wish everyone the best of luck in their future endeavors.

TABLE OF CONTENTS

List of Figures

List of Tables

List of Appendices

Abstract

Heterogeneity in cancer can give rise to rare subpopulations of cells that are unlike the bulk average of the cancer cell population, such as metastatic cells which promote the formation of secondary tumors at distant sites. These subpopulations of cells can dramatically affect the progression of the disease. Recent work suggests that heterogeneity in cancer cell populations assessed by clonal analysis cannot fully account for differences in single cell behaviors. Nonclonal heterogeneity, such as variability due to the cellular microenvironment, can play a key role in promoting cancer behaviors. Signaling heterogeneity to downstream kinase effectors is one manifestation of nonclonal heterogeneity. Seemingly-identical cancer cells activate heterogeneous signaling to extracellular signal-regulated kinase (ERK) and Akt, two kinases implicated in cancer growth, survival, proliferation, and metastasis. The mechanistic drivers that promote signaling heterogeneity remain unclear and understanding them is crucial in effectively treating cancer. Advancements in single-cell experimental techniques and computational modeling can elucidate how the spatiotemporal tumor microenvironment shapes cancer cell behavior. In this thesis, we construct mechanistic computational models coupled to experimental data to understand the major drivers of nonclonal heterogeneity in cancer. First, we built a single-cell computational model to explain the heterogeneity in cell signaling responses to ERK and Akt that we observed in breast cancer cells in experiments. The model predicted that the pre-existing signaling state of cancer cells controls signaling responses through chemokine receptor CXCR4, a critical receptor in cancer initiation and metastasis, and that these pre-existing states are shaped by environmental stimuli. The model also predicted that targeted therapies currently under clinical investigation may inadvertently potentiate pro-metastatic signaling through CXCR4. Second, we expanded our computational model to test its robustness in predicting signaling through another key receptor in cancer proliferation, epidermal growth factor receptor (EGFR). Our model predicted single-cell signaling

responses in two breast cancer cell lines of various mutational backgrounds to different doses of both CXCR4 and EGFR stimuli. The robustness of our model solidified our hypothesis that variation in cell signaling stems from extrinsic noise in three key pathway components: phosphatidylinositol-3-kinase (PI3K), Ras, and mammalian target of rapamycin complex 1 (mTORC1). Third, we built a spatial model of the tumor microenvironment to understand the impact of circadian rhythms and heterogeneity in the spatial tumor composition in promoting metastasis. We found that the magnitude of chemokine gradients, which can act as the molecular highway directing cancer cells where to invade and metastasize, varies throughout the course of the day with the circadian rhythm such that therapies may be more or less effective based on time of administration. Additionally, the spatial arrangement of a tumor with regard to cells secreting and scavenging these chemokines, which can vary tumor-to-tumor or within a single tumor, has a marked impact on the direction of chemokine gradients. We found that specific arrangements of cells in tumors promote chemokine gradients that can direct cancer cells to intravasate and metastasize. Overall, this thesis builds on our knowledge of heterogeneity in cancer and provides suggestions for clinical opportunities.

Chapter 1 Introduction

1.1 Motivation

Cancer is a heterogeneous disease. Seemingly identical cells can respond to their environment differently than one another. Heterogeneity in the tumor microenvironment can impact cellular responses and give rise to aggressive subpopulations of cells that can control overall cancer progression. Currently, many cancer therapies, including chemotherapy and targeted therapy, often fail to fully contain or kill these subpopulations. In order to effectively target aggressive subpopulations, we need an understanding of the biological mechanisms that promote their existence and survival. In this thesis, I elucidate mechanisms that drive spatiotemporal heterogeneity in cancer cell responses and microenvironments with implications for strategic targeted therapies.

1.2 Receptor Biology

1.2.1 Chemokine receptor CXCR4 and its ligand CXCL12

Chemokine receptor CXCR4 is a G-protein coupled receptor (GPCR) involved in normal development and physiology that is expressed on immune cells and cells in the central nervous system (1–5). Chemokine ligand binds to CXCR4 and elicits downstream G-protein signaling that can drive directed cell migration from low to high concentrations, a process called chemotaxis (6,7). Cancers of various types, including brain, breast, and prostate, are known to overexpress CXCR4 (8). CXCR4 is implicated in cancer initiation and metastasis in more than 20 different malignancies and is correlated with poor prognosis. The CXCR4 inhibitor balixafortide has shown favorable results in a Phase I clinical trial as an adjuvant therapy for advanced metastatic breast cancer (9), reinforcing the need to understand CXCR4 biology.

Chemokine CXCL12 is a small, 10-kDa protein that exists in six different isoforms that can bind CXCR4 in humans (10,11). The three most abundant isoforms in humans are CXCL12-α, CXCL12-β, and CXCL12-γ. These isoforms are formed due to alternative splicing and are comprised of the same 89 amino acids on the N-terminus; they differ in length and composition on the C-terminus end. All isoforms of CXCL12 contain many basic residues and are therefore positively charged (12). The positive charge allows CXCL12 isoforms to nonspecifically bind to negatively-charged glycosaminoglycans (GAGs) on cell membranes (13–15). There are two major functional differences between the isoforms: they have different affinities for GAGs, and they are secreted at different rates from fibroblasts, the major producers of CXCL12 (13,14,16–18). In Chapter 4, we discuss how these differences can promote gradients of CXCL12 in the tumor microenvironment conducive to CXCR4-mediated chemotaxis.

CXCR4 expression and CXCL12 concentrations vary temporally (about 2-3 fold) with the circadian rhythm (19–22). The natural blood dynamics of CXCL12 levels indicate that CXCL12 gradients between tissue and the vasculature can vary in magnitude throughout the day (14). The fact that CXCL12 gradients are time-dependent highlights how cancer cells may be more prone to metastasize at specific times of day (20), and perhaps therapeutic agents against CXCR4 would be most efficacious at specific times of day (23).

1.2.2 CXCR7 biology

CXCR7, now referred to as ACKR3, is an atypical chemokine receptor that can also bind CXCL12 but does not elicit G-protein signaling upon ligand binding (24,25). The binding interaction between CXCR7 and CXCL12 has a 10-fold higher affinity than the interaction between CXCR4 and CXCL12 (24). CXCR7 acts as a CXCL12 scavenger by rapidly binding, internalizing, and degrading CXCL12 (14,16,26–28). CXCR7 is highly expressed on tumor vasculature and deeper within tumor tissue in nearly all breast tumors, but is not expressed on normal breast epithelia or vasculature (29). The spatial composition of tumors with regards to the localization of fibroblasts which secrete CXCL12 and CXCR7-positive cells which scavenge the ligand is conducive to micro-

scale gradients of CXCL12 which may elicit chemotaxis of CXCR4-positive cells. In Chapter 4, we discuss how the spatial localization of cells forms CXCL12 gradients in the tumor microenvironment. We implicate the spatial arrangement of CXCR7 within the tumor as a potential marker for cancer aggressiveness and propensity to create conditions conducive for metastasis.

1.2.3 Epidermal growth factor receptor biology

Epidermal growth factor receptor (EGFR) is a receptor tyrosine kinase involved in cell growth and proliferation (30,31). Upon binding ligand, one of which is epidermal growth factor (EGF), the receptor dimerizes, internalizes, and elicits downstream signaling (31–33). EGFR is overexpressed in a many solid tumors, including breast, head-and-neck, non-small-cell lung, renal, ovarian, and colon cancer (34,35), and is thus a target for cancer therapies. In Chapter 2, we integrate a computational model with single-cell experimental data to illustrate how signaling through EGFR promotes a cellular memory effect in CXCR4 signaling. In Chapter 3, we further test the computational model by incorporating receptor-ligand dynamics for EGFR and predicting downstream signaling through this receptor.

1.3 Cell signaling pathways

Cell signaling pathways are the networks that allow cells to interpret information about their environments (36). Generally, signaling pathways are activated by a receptor-ligand interaction at the cell surface. The signal is then transduced downstream to intracellular kinases, and activation of these kinases promotes gene expression. Cell signaling pathways are vital for proper normal physiological development, but are often dysregulated in diseases, including cancer (37). Throughout this thesis, we focus on receptor-mediated Akt, ERK, and mTORC1/2 activation, all of which are implicated in numerous cancer phenotypes.

1.3.1 PI3K/Akt signaling

Phosphatidylinositol-3-kinase (PI3K)/Akt is a signaling pathway activated by many different receptors including both CXCR4 and EGFR (Figure 1.1) (32,38–40). PI3K/Akt signaling is implicated in many cellular functions such as cell growth, metabolism, division, and survival (41,42). The signaling pathway is initiated by activation of PI3K, which phosphorylates the lipid phosphatidylinositol 4,5-biphosphate (PIP2) to form phosphatidylinositol 3,4,5-triphosphate (PIP3) (43). PIP3 then catalyzes the activation of phosphoinosotide-dependent kinase 1 (PDK1) which phosphorylates the Thr^{308} site on Akt. This only partially activates Akt (44). Full activation of Akt requires activation on the Ser^{473} site, which is done by mechanistic target of rapamycin complex 2 (mTORC2). The activation of mTORC2 is poorly defined in literature, but most studies agree it is PI3K-dependent (45,46). In Chapters 2 and 3, we build a computational model capable of predicting PI3K/Akt signaling in single-cells with implications for targeted therapeutics.

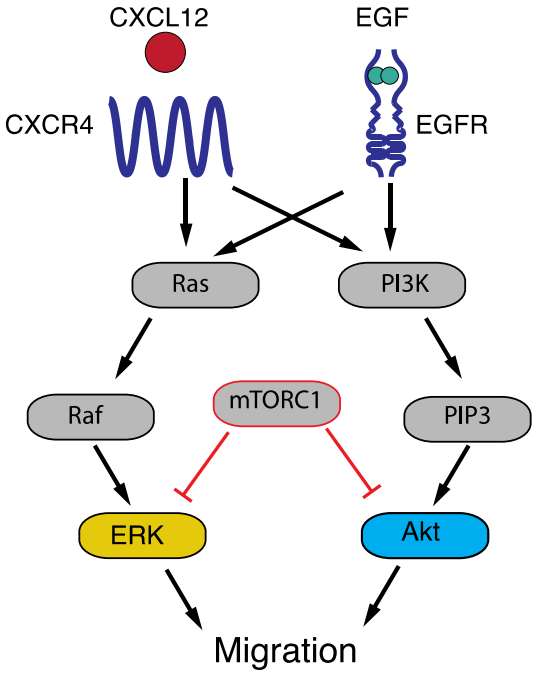

Figure 1.1 CXCR4 and EGFR signal to ERK and Akt can drive cell migration

When CXCR4 and EGFR are liganded with CXCL12 or EGF, respectively, they promote ERK and Akt signaling. ERK and Akt signaling are associated with a variety of cancer phenotypes, one of which is cell migration.

1.3.2 MAPK/ERK signaling

The mitogen-activated protein kinase (MAPK)/extracellular signal-regulated kinase (ERK) signaling pathway, also referred to as the Ras/Raf/MEK/ERK signaling pathway, is signaling cascade which promotes cell growth, division, and survival (47,48). MAPK/ERK signaling is downstream of a variety of families of receptors, including both CXCR4 and EGFR (Figure 1.1) (32,38,49,50). The pathway is initiated by the activation of Ras, a small GTPase inside cells. Ras activates Raf, which scaffolds with the kinase MEK to activate downstream ERK (51,52). In addition, Raf is inhibited by active Akt, identifying a crosstalk mechanism by which activation of one pro-survival pathway can directly inhibit another (53,54). In Chapters 2 and 3, we build a computational model of the MAPK/ERK signaling pathway in conjunction with PI3K/Akt signaling to understand the mechanisms driving single-cell responses through these pathways.

1.3.3 mTORC1/2 signaling

Mechanistic target of rapamycin (mTOR) is a protein kinase subunit downstream of many receptors and is involved in cell growth and metabolism (55). mTOR can bind to a variety of other intracellular proteins to form two important complexes termed mTOR complex 1 (mTORC1) and mTOR complex 2 (mTORC2) (56). mTORC1 controls the balance between anabolism, the synthesis of complex molecules from simpler ones, and catabolism, the breakdown of complex molecules into simpler ones (55,57). mTORC2 is involved in regulating cytoskeletal rearrangement and has been linked to cell migration, among other cancer phenotypes (58–60). Unregulated mTORC1/2 signaling can promote cancer progression (55).

mTORC1 and mTORC2 intersect with the PI3K/Akt and MAPK/ERK pathways (61). mTORC1 functions as a major regulator of both PI3K/Akt and MAPK/ERK signaling by inhibiting both pathways (Figure 1.1) (62,63). mTORC1 can prevent the formation of

mTORC2 by removing a required component of mTORC2, mSIN1 (64,65). Because the major role of mTORC2 is to activate Akt on the Ser^{473} site (60), mTORC1 can inhibit Akt signaling. Additionally, mTORC1 negatively regulates the MAPK pathway upstream of ERK (62). These inhibitory mechanisms position mTORC1 as a central regulator of Akt and ERK signaling.

1.3.4 Targeted inhibition of kinase signaling

Specific kinases within cell signaling pathways present viable targets for cancer therapy due to their roles in oncogenic phenotypes (66). Trametinib is a MEK inhibitor which abrogates ERK signaling and was approved for certain patients with metastatic melanoma in 2013 (67). Ridaforolimus is an mTOR inhibitor which acutely inhibits mTORC1 but only prolonged exposure to the drug decreases mTORC2 activity (56). Using the computational model developed in Chapter 2, we predict how these pharmacologic inhibitors actually potentiate pro-metastatic signaling in pathways that were not the direct target. In Chapter 3, we perform simulations that suggest that a PI3K inhibitor may potentiate ERK signaling in subsets of breast cancer cells. Modeling coupled to experiments allows us elucidate the mechanistic behavior of dynamic cell signaling systems with implications for therapeutic efficacy.

1.4 Heterogeneity in cancer

1.4.1 Clonal vs. nonclonal heterogeneity

Biological systems and diseases are inherently heterogeneous, and cancer is no exception. Heterogeneity in cancer promotes the formation of small subpopulations of cells that are unlike the tumor bulk. These subpopulations can drive cancer progression, drug resistance, and recurrence (68–70). Biological heterogeneity generally falls into one of two categories: clonal and nonclonal (69). Clonal heterogeneity encompasses genomic variability between cells, accounting for differences in mutational backgrounds and transient gene expression (71). Clonal heterogeneity is transmitted to daughter cells since its source lies in DNA. Nonclonal heterogeneity comprises functional plasticity in phenotypes related to cellular environment, such as autocrine and paracrine

interactions (68). Clonal heterogeneity is more well-studied than nonclonal heterogeneity, but evidence suggests that the two work in tandem to diversify cell populations and promote survival in stressful conditions (68,70,72). In this thesis, we focus primarily on understanding nonclonal heterogeneity with an emphasis on its origins and tunability.

1.4.2 Cell signaling heterogeneity

One manifestation of nonclonal heterogeneity is signaling heterogeneity. Signaling heterogeneity describes how, when stimulated with a ligand, seemingly identical cells expressing the target receptor elicit downstream kinase responses along a continuum from no to high activation (73–77). The failure of ligand-receptor binding to activate downstream kinases in some cells exemplifies how purely genetic analyses cannot be fully predictive of tumor behavior or efficacy of targeted therapies. Some studies choose to ignore single-cell behaviors and only capture the behavior of the population average (74,78,79), or they choose to only analyze the small fraction of cells that respond and ignore the rest, whether in regards to signaling or a phenotype driven by signaling (80). Signaling heterogeneity may explain heterogeneity in a variety of cellular phenotypes, such as migration or responsiveness to cancer therapies. For example, several studies show how cells in engineered microenvironments stimulated with gradients of chemokines drive chemotaxis in only a subset of cells (16,17,81). Additionally, since cell signaling states can affect efficacy of targeted therapies or immunotherapies, cell signaling heterogeneity may explain why some cells respond to cancer treatments and some do not (68). Studying the mechanisms which drive signaling heterogeneity in the context of the tumor microenvironment can unlock new treatment strategies to target cell signaling in the subset of cells driving progression of the disease.

1.4.3 Single-cell experimental approaches to detect signaling heterogeneity

Single-cell experimental approaches have enabled examination of signaling heterogeneity without lumping behaviors into bulk population averages. Tsien et. al developed a fura-2 calcium probe to examine single-cell calcium dynamics and found

that mitosis can promote functional signaling differences between daughter cells (76). Kumagai et. al used Förster resonance energy transfer (FRET) reporters to uncover that basal ERK activity in single tumor cells was indicative of the ability to form tumors (82). Using kinase translocation reporters, Miura et. al uncovered that heterogeneity in p38-mediated cross-inhibition was the driver behind stochastic cell death following UV stress (83). These technologies enable the study of single cell signaling and the phenotypes that emerge from specific signaling motifs. However, there is still a gap in our understanding of the underlying mechanisms which drive these heterogeneous signaling behaviors and how can control them, as well as how to best analyze data without discounting the behavior of small subpopulations.

1.4.4 Origins of signaling heterogeneity: intrinsic vs. extrinsic noise

A major question in understanding the sources of signaling heterogeneity is whether the heterogeneity is due to intrinsic or extrinsic noise. Intrinsic noise encompasses the inherent stochasticity of biological events and becomes increasingly important as the number of molecules involved decreases (84–86). If we posit that signaling heterogeneity is due to purely intrinsic noise, we assume that the ability of cells to respond or not to a ligand stimulus is due to random fluctuations in chemical kinetics of signaling. Extrinsic noise refers to variation in identically-regulated entities between cells (73,87,88). If we posit that signaling heterogeneity is due to purely extrinsic noise, we assume that the ability of cells to respond or not to a ligand stimulus is due to cell-to-cell variability in, for example, active kinase levels. This question regarding the type of noise present in cell signaling also asks about our ability to control the heterogeneity. Heterogeneity set by intrinsic noise cannot easily be controlled since it is due to stochastic fluctuations likely at the molecular scale. Heterogeneity set by extrinsic noise may have a higher potential for intervention because we have the ability to inhibit the expression of certain kinases or certain aspects of the cellular microenvironment.

1.4.5 Incorporating heterogeneity in computational models of cell signaling

The methods and assumptions used in computational models to generate cell signaling heterogeneity are important because they imply where we believe the source of the heterogeneity originates. Ordinary differential equation (ODE) models are common for studying cell signaling because they can simulate continuous, time-dependent kinetic interactions of multiple components in a complex network based on a set of parameters (89,90). ODE models generally incorporate heterogeneity by adding intrinsic or extrinsic noise to the system, or both.

One approach to incorporate signaling heterogeneity to an ODE model is by adding intrinsic noise (stochastic fluctuations). Using a semi-stochastic model, Lee et. al recapitulated heterogeneous NFκB signaling dynamics at a variety of stimulus dose concentrations of lipopolysaccharide (91). Another common method of incorporating intrinsic noise is the Gillespie algorithm (87), which uses a Monte Carlo framework to add intrinsic noise (92,93). However, recent work suggests that much signaling heterogeneity can be explained using extrinsic noise without the need to invoke stochastic origins (73,94,95).

Extrinsic noise in cell signaling networks is appreciated as the major driver of signaling heterogeneity in a number of recent studies (77,88,96,97). The theory that extrinsic noise is necessary to explain signaling heterogeneity assumes that cells are in different pre-existing states, and, when challenged with a ligand stimulus, respond differently because of these different pre-existing states (98). Kim et. al used ODE modeling with extrinsic noise to simulate ERK and Akt signaling heterogeneity with implications for therapy efficacy (73). Wang et. al showed that extrinsic “colored” noise was the major driver of variability in p53 oscillations compared to intrinsic “white” noise (95). However, current methods of using extrinsic noise in cell signaling networks to explain heterogeneous responses fail to provide a structural framework for allowing cells to dynamically adjust to new cellular environments. In Chapters 2 and 3, we use extrinsic noise in our computational model to predict how cell states are altered due to changes in recent environmental stimuli.

1.5 Approaches

1.5.1 Kinase translocation reporters (KTRs)

In this thesis, we build computational models of cell signaling networks based on single-cell data gathered using the KTR technology adapted by the Gary and Kathryn Luker lab. KTRs function by converting phosphorylation into a nucleocytoplasmic shuttling event in single cells. As a kinase is phosphorylated, the reporter shuttles into the cytoplasm, and as the kinase is dephosphorylated, the reporter shuttles into the nucleus (99,100). The Luker lab multiplexed two existing KTRs, the Akt KTR and the ERK KTR, in MDA-MB-231, SUM 159, and Vari068 breast cancer cells (77). These cells additionally contain an H2B-Cherry nucleus for image analysis purposes. By imaging a cell population in real time, we can gain dynamic signaling outputs for both ERK and Akt in single cells responding to a bolus ligand dose. These data can elucidate the range of heterogeneous ERK and Akt responses in single cells to calibrate a computational model of cell signaling.

1.5.2 Conditional signaling model incorporating extrinsic noise

In Chapters 2 and 3, we build an ODE model to provide mechanistic causality for the range of signaling responses through ERK and Akt in breast cancer cells using extrinsic noise. Our model, which we named the Conditional Signaling Model (CSM), simulates the cascade of phosphorylation events that occur upon CXCR4 or EGFR stimulation and culminates with ERK and Akt activation dynamics. The CSM contains three modules: receptor-ligand dynamics, signaling dynamics, and reporter dynamics. We use the CSM to develop a signaling landscape, which simulates how pre-existing cell states govern responsiveness through ERK and Akt upon ligand stimulation. Importantly, the CSM provides a framework for understanding how cells dynamically edit their signaling responses in the presence of growth factors or targeted kinase therapies.

1.5.3 Spatiotemporal model of CXCL12 gradients in the tumor microenvironment

Chemokine gradients *in vivo* can promote chemotaxis and metastasis, but are difficult to measure because they exist in a dynamic environment and are governed by multiple competing mechanisms. In Chapter 4, we build a computational model to simulate dynamic CXCL12 gradients in a primary tumor based on a host of known mechanisms. We use a 3D square lattice grid structure to place cells in discrete compartments to simulate the cellular architecture of a primary tumor environment. We simulate both CXCL12-secreting cells (fibroblasts) as well as CXCR7-positive cells. As the simulation progresses, fibroblasts secrete CXCL12 into the grid compartment that they occupy at a rate dictated by the circadian rhythm, the ligand diffuses by a partial differential equation (PDE), and CXCR7-positive cells contain a set of ODEs which allow CXCL12-CXCR7 binding, internalization, and ligand degradation. Additionally, a blood vessel through the center of the grid allows us to simulate how both the blood and local fibroblasts in primary tumors supply CXCL12 to the tumor microenvironment and how gradients form between deep within tissue and the local vasculature. This model predicts how circadian fluctuations edit CXCL12 gradient magnitudes over the course of a day, and how heterogeneity in the spatial composition of tumors, such as the ratio of fibroblasts to CXCR7-positive cells, can shape CXCL12 gradient direction and magnitude.

1.6 Thesis summary

In this thesis, we build computational models focusing on the emergence of heterogeneity in cancer and its tunability. In Chapter 2, we construct the conditional signaling model (CSM) to understand how pre-existing cell states govern heterogeneous signaling from CXCR4 to Akt and ERK and how cellular memory tunes subsequent signaling responses. In Chapter 3, we assess the capability of the model to predict heterogeneous cell states consistent with another receptor system, EGFR, to test model robustness. In Chapter 4, we construct a spatial model of a portion of a primary tumor to determine how heterogeneity in the makeup of the microenvironment influences CXCL12 gradient direction and magnitude. Overall, we uncover mechanisms

driving heterogeneity in cancer that can inform new treatment strategies targeting key subpopulations of cells controlling disease progression.

1.7 References

1. Aiuti BA, Webb IJ, Bleul C, Springer T, Gutierrez-Ramos J. The Chemokine SDF-1 Is a chemoattractant for human CD34+ hematopoietic progenitor cells and provides a new mechanism to explain the mobilization of CD34+ progenitors to peripheral blood. J Exp Med. 1997;185(1):111–20.
2. Förster R, Kremmer E, Schubel A, Breitfeld D, Kleinschmidt A, Nerl C, et al. Intracellular and surface expression of the HIV-1 coreceptor CXCR4/fusin on various leukocyte subsets: rapid internalization and recycling upon activation. J Immunol. 1998;160:1522–31.
3. Zou Y, Kottman A, Kuroda M, Taniuchi I, Littman D. Function of the chemokine receptor CXCR4 in heaematopolesis and in cerebellar development. Nature. 1998;393:595–9.
4. Tanabe S, Heesen M, Yoshizawa I, Berman MA, Luo Y, Bleul CC, et al. Functional expression of the CXC-chemokine receptor-4/fusin on mouse microglial cells and astrocytes. J Immunol. 1997;159:905–11.
5. Teixidó J, Martínez-Moreno M, Díaz-Martínez M, Sevilla-Movilla S. The good and bad faces of the CXCR4 chemokine receptor. Int J Biochem Cell Biol. 2018;95:121–31.
6. Fernandis AZ, Prasad A, Band H, Klösel R, Ganju RK. Regulation of CXCR4-mediated chemotaxis and chemoinvasion of breast cancer cells. Oncogene. 2004;23:157–67.
7. Nagasawa T. CXC chemokine ligand 12 (CXCL12) and its receptor CXCR4. J Mol Med. 2014;92:433–9.
8. Cojoc M, Peitzsch C, Polishchuk L, Telegeev G, Dubrovska A. Emerging targets in cancer management: role of the CXCL12/CXCR4 axis. Onco Targets Ther. 2013;6:1347–61.
9. Pernas S, Martin M, Kaufman PA, Gil-Martin M, Pardo PG, Lopez-Tarruella S, et al. Balixafortide plus eribulin in HER2-negative metastatic breast cancer: a phase 1, single-arm, dose-escalation trial. Lancet Oncol. 2018;19:812–24.
10. Yu L, Cecil J, Peng S-B, Schrementi J, Kovacevic S, Paul D, et al. Identification and expression of novel isoforms of human stromal cell-derived factor 1. Gene. 2006;374:174–9.
11. Zhao S, Chang SL, Linderman JJ, Feng FY, Luker GD. A Comprehensive Analysis of CXCL12 Isoforms in Breast Cancer. Transl Oncol. 2014;7(3):429–38.
12. Janowski M. Functional diversity of SDF-1 splicing variants. Cell Adhes Migr. 2009;3(3):243–9.
13. Laguri C, Sadir R, Rueda P, Baleux F, Gans P, Arenzana-Seisdedos F, et al. The novel CXCL12gamma isoform encodes an unstructured cationic domain which regulates bioactivity and interaction with both glycosaminoglycans and CXCR4. PLoS One. 2007;2(10):e1110.
14. Spinosa PC, Luker KE, Luker GD, Linderman JJ. The CXCL12/CXCR7 signaling axis, isoforms, circadian rhythms, and tumor cellular composition dictate gradients in tissue. PLoS One. 2017;12(11).
15. Gschwandtner M, Trinker MU, Hecher B, Adage T, Ali S, Kungl AJ. Glycosaminoglycan silencing by engineered CXCL12 variants. FEBS Lett.

2015;589:2819–24.
16. Chang SL, Cavnar SP, Takayama S, Luker GD, Linderman JJ. Cell, Isoform, and Environment Factors Shape Gradients and Modulate Chemotaxis. PLoS One. 2015;10(4):e0123450.
17. Cavnar SP, Ray P, Moudgil P, Chang SL, Luker KE, Linderman JJ, et al. Microfluidic source-sink model reveals effects of biophysically distinct CXCL12 isoforms in breast cancer chemotaxis. Integr Biol. 2014;6(5):564–76.
18. Rueda P, Balabanian K, Lagane B, Staropoli I, Chow K, Levoye A, et al. The CXCL12γ chemokine displays unprecedented structural and functional properties that make it a paradigm of chemoattractant proteins. PLoS One. 2008;3(7).
19. Ella K, Csépányi-kömi R, Káldi K. Circadian regulation of human peripheral neutrophils. Brain Behav Immun. 2016;57:209–21.
20. Pick R, He W, Chen C-S, Scheiermann C. Time-of-Day-Dependent Trafficking and Function of Leukocyte Subsets. Trends Immunol. 2019;40(6):524–37.
21. Nakao A. Temporal Regulation of Cytokines by the Circadian Clock. J Immunol Res. 2014;2014:1–4.
22. Lucas D, Battista M, Frenette PS. Haematopoietic stem cell release is regulated by circadian oscillations. 2008;452(March).
23. Gery S, Koeffler H. Circadian rhythms and cancer. Cell Cycle. 2010;9(6):1097–103.
24. Balabanian K, Lagane B, Infantino S, Chow KYC, Harriague J, Moepps B, et al. The Chemokine SDF-1/CXCL12 Binds to and Signals through the Orphan Receptor RDC1 in T Lymphocytes. J Biol Chem. 2005;280(42):35760–6.
25. Rajagopal S, Kim J, Ahn S, Craig S, Lam CM, Gerard NP, et al. B-arrestin- but not G protein-mediated signaling by the “decoy” receptor CXCR7. PNAS. 2010;107(2):628–32.
26. Bonecchi R, Graham GJ. Atypical chemokine receptors and their roles in the resolution of the inflammatory response. Front Immunol. 2016;7(224):1–7.
27. Luker KE, Lewin SA, Mihalko LA, Schmidt BT, Winkler JS, Coggins NL, et al. Scavenging of CXCL12 by CXCR7 promotes tumor growth and metastasis of CXCR4-positive breast cancer cells. Oncogene. 2012;31(45):4750–8.
28. Luker KE, Steele JM, Mihalko LA, Ray P, Luker GD. Constitutive and chemokine-dependent internalization and recycling of CXCR7 in breast cancer cells to degrade chemokine ligands. Oncogene. 2010;29(32):4599–610.
29. Miao Z, Luker KE, Summers BC, Berahovich R, Bhojani MS, Rehemtulla A, et al. CXCR7 (RDC1) promotes breast and lung tumor growth in vivo and is expressed on tumor-associated vasculature. Proc Natl Acad Sci U S A. 2007;104(40):15735–40.
30. Sasaki T, Hiroki K, Yamashita Y. The role of epidermal growth factor receptor in cancer metastasis and microenvironment. Biomed Res Int. 2013;3.
31. Mancino M, Bianco C, De Feo G, De Luca A, Caponigro F, Normanno N, et al. Epidermal growth factor receptor (EGFR) signaling in cancer. Gene. 2006;366(1):2–16.
32. Wee P, Wang Z. Epidermal growth factor receptor cell proliferation signaling pathways. Cancers (Basel). 2017;9(5):1–45.
33. Dawson JP, Berger MB, Lin C, Schlessinger J, Lemmon MA, Ferguson KM.

Epidermal Growth Factor Receptor Dimerization and Activation Require Ligand-Induced Conformational Changes in the Dimer Interface. Mol Cell Biol. 2005;25(17):7734–42.
34. Herbst R. Review of epidermal growth factor receptor biology. Int J Radiat Oncol Biol Phys. 2004;59(2):21–6.
35. Bethune G, Bethune D, Ridgway N, Zhaolin X. Epidermal growth factor receptor (EGFR) in lung cancer: an overview and update. J Thorac Dis. 2010;2(1):48–51.
36. Uings IJ, Farrow SN. Cell receptors and cell signalling. J Clin Pathol - Mol Pathol. 2000;53(6):295–9.
37. Hanahan D, Weinberg RA. Hallmarks of cancer: the next generation. Cell [Internet]. 2011;144(5):646–74. Available from: http://www.cell.com/article/S0092867411001279/fulltext
38. Teicher BA, Fricker SP. CXCL12 (SDF-1)/CXCR4 Pathway in Cancer. Clin Cancer Res. 2010;16(11):2927–31.
39. Döring Y, Pawig L, Weber C, Noels H. The CXCL12/CXCR4 chemokine ligand/receptor axis in cardiovascular disease. Front Physiol. 2014;5(212):1–23.
40. Domanska UM, Kruizinga RC, Nagengast WB, Timmer-Bosscha H, Huls G, De Vries EGE, et al. A review on CXCR4/CXCL12 axis in oncology: No place to hide. Eur J Cancer. 2013;49(1):219–30.
41. Manning B, Cantley L. AKT/PKB Signalling: Navigating the Network. Cell. 2017;169:1261–74.
42. Sun X, Cheng G, Hao M, Zheng J, Zhou X, Zhang J, et al. CXCL12/CXCR4/CXCR7 chemokine axis and cancer progression. Cancer Metastasis Rev. 2010;29(4):709–22.
43. Franke TF. PI3K/Akt: Getting it right matters. Oncogene. 2008;27:6473–88.
44. Yudushkin I. Getting the Akt Together: Guiding Intracellular Akt Activity by PI3K. Biomolecules. 2019;9(67):1–14.
45. Gan X, Wang J, Su B, Wu D. Evidence for direct activation of mTORC2 kinase activity by phosphatidylinositol 3,4,5-trisphosphate. J Biol Chem. 2011;286(13):10998–1002.
46. Yang G, Murashige DS, Humphrey SJ, James DE. A Positive Feedback Loop between Akt and mTORC2 via SIN1 Phosphorylation. Cell Rep. 2015;12(6):937–43.
47. Burotto M, Chiou V, Lee J, Kohn E. The MAPK pathway across different malignancies: A new perspective. Cancer. 2014;120(22):3446–56.
48. McCubrey J, Steelman L, Chappell W, Abrams S, Wong E, Chang F, et al. Roles of the Raf/MEK/ERK pathway in cell growth, malignant transformation and drug resistance. Biochim Biophys Acta. 2007;1773:1263–84.
49. Lagane B, Chow KYC, Balabanian K, Levoye A, Harriague J, Planchenault T, et al. CXCR4 dimerization and 2-arrestin mediated signaling account for the enhanced chemotaxis to CXCL12 in WHIM syndrome. Blood. 2008;112(1):34–44.
50. Luker K, Gupta M, Luker G. Imaging CXCR4 signaling with firefluy luciferase complementation. Anal Chem. 2008;80(14):5565–73.
51. Margolis B, Skolnik E. Activation of Ras by Receptor Tyrosine Kinases. J Am Soc Nephrol. 1994;5(6):1288–99.
52. Wortzel I, Seger R. The ERK cascade: Distinct functions within various subcellular

organelles. Genes and Cancer. 2011;2(3):195–209.
53. Moelling K, Schad K, Bosse M, Zimmermann S, Schweneker M. Regulation of Raf-Akt cross-talk. J Biol Chem. 2002;277(34):31099–106.
54. Zimmermann S, Moelling K. Phosphorylation and Regulation of Raf by Akt (Protein Kinase B). Science (80-). 1999;286:1741–4.
55. Saxton RA, Sabatini DM. mTOR Signaling in Growth, Metabolism, and Disease. Cell. 2017;168(6):960–76.
56. Vilar E, Perez-Garcia J, Tabernero J. Pushing the envelope in the mTOR pathway. The second generation of inhibitors. Mol Cancer Ther. 2011;10(3):395–403.
57. Son SM, Park SJ, Lee H, Siddiqi F, Lee JE, Menzies FM, et al. Leucine Signals to mTORC1 via Its Metabolite Acetyl-Coenzyme A. Cell Metab. 2019;29:192–201.
58. Jacinto E, Loewith R, Schmidt A, Lin S, Rüegg MA, Hall A, et al. Mammalian TOR complex 2 controls the actin cytoskeleton and is rapamycin insensitive. Nat Cell Biol. 2004;6(11):1122–8.
59. Angliker N, Rüegg M a. In vivo evidence for mTORC2-mediated actin cytoskeleton rearrangement in neurons. Bioarchitecture. 2013;3(4):113–8.
60. Oh WJ, Jacinto E. mTOR complex 2 signaling and functions. Cell Cycle. 2011;10(14):2305–16.
61. Mendoza M, Emrah Er E, Blenis J. The Ras-ERK and PI3K-mTOR Pathways: Cross-talk and Compensation. Trends Biochem Sci. 2011;36(6):320–8.
62. Posada IMD, Lectez B, Siddiqui FA, Oetken-Lindholm C, Sharma M, Abankwa D. Opposite feedback from mTORC1 to H-ras and K-ras4B downstream of SREBP1. Sci Rep. 2017;7(1):1–14.
63. Ebner M, Sinkovics B, Szczygieł M, Ribeiro DW, Yudushkin I. Localization of mTORC2 activity inside cells. J Cell Biol. 2017;216(2):343–53.
64. Yuan H, Guan K. The Sin1 PH domain connects mTORC2 to PI3K. Cancer Discov. 2015;5(11):1127–9.
65. Liu P, Gan W, Inuzuka H, Lazorchak AS, Gao D, Arojo O, et al. Sin1 phosphorylation impairs mTORC2 complex integrity and inhibits downstream Akt signalling to suppress tumorigenesis. Nat Cell Biol. 2013;15(11):1340–50.
66. Charles Sawyers. Targeted Cancer Therapy. Nature. 2004;432:294–297.
67. Banks M, Crowell K, Proctor A, Jensen BC. Cardiovascular Effects of the MEK Inhibitor, Trametinib: A Case Report, Literature Review, and Consideration of Mechanism. Cardiovasc Toxicol. 2017;17(4):487–93.
68. Stanta G, Bonin S. Overview on Clinical Relevance of Intra-Tumor Heterogeneity. Front Med. 2018;5(85):1–10.
69. Dagogo-Jack I, Shaw AT. Tumour heterogeneity and resistance to cancer therapies. Nat Rev Clin Oncol. 2018;15:81–94.
70. Meacham CE, Morrison SJ. Tumor heterogeneity and cancer cell plasticity. Nature. 2013;501(7467):328–37.
71. McGranahan N, Swanton C. Clonal Heterogeneity and Tumor Evolution: Past, Present, and the Future. Cell. 2017;168:613–28.
72. Marusyk A, Polyak K. Tumor heterogeneity: causes and consequences. Biochim Biophys Acta. 2010;1805(1):1–28.
73. Kim E, Kim J, Smith MA, Haura EB, Alexander R, Anderson A. Cell signaling

heterogeneity is modulated by both cell-intrinsic and -extrinsic mechanisms: An integrated approach to understanding targeted therapy. PLoS Biol. 2018;16(3):1–29.
74. Altschuler SJ, Wu LF. Cellular Heterogeneity: Do Differences Make a Difference? Cell. 2010;141:559–63.
75. Irish JM, Hovland R, Krutzik PO, Perez OD, Bruserud Ø, Gjertsen BT, et al. Single Cell Profiling of Potentiated Phospho-Protein Networks in Cancer Cells. Cell. 2004;118:217–28.
76. Tsien RY, Poenie M. Fluorescence ratio imaging: a new window into intracellular ionic signaling. Vol. 11, Trends in Biochemical Sciences. 1986. p. 450–5.
77. Spinosa PC, Humphries BA, Lewin Mejia D, Buschhaus JM, Linderman JJ, Luker GD, et al. Short-term cellular memory tunes the signaling responses of the chemokine receptor CXCR4. Sci Signal. 2019;12(589).
78. Pappalardo F, Russo G, Candido S, Pennisi M, Cavalieri S, Motta S, et al. Computational modeling of PI3K/AKT and MAPK signaling pathways in melanoma cancer. PLoS One. 2016;11(3):1–10.
79. Abdallah BY, Horne SD, Stevens JB, Liu G, Ying AY, Vanderhyden B, et al. Single cell heterogeneity: Why unstable genomes are incompatible with average profiles. Cell Cycle. 2013;12(23):3640–9.
80. Poon M, Marx S, Gallo R, Badimon J, Taubman M, Marks A. Rapamycin inhibits vascular smooth muscle cell migration. J Clin Invest. 1996;98(10):2277–83.
81. Kim BJ, Hannanta-anan P, Chau M, Kim YS, Swartz MA, Wu M. Cooperative roles of SDF-1α and EGF gradients on tumor cell migration revealed by a robust 3D microfluidic model. PLoS One. 2013;8(7):e68422.
82. Kumagai Y, Naoki H, Nakasyo E, Kamioka Y, Kiyokawa E, Matsuda M. Heterogeneity in ERK activity as visualized by in vivo FRET imaging of mammary tumor cells developed in MMTV-Neu mice. Oncogene. 2015;34:1051–7.
83. Miura H, Kondo Y, Matsuda M, Aoki K. Cell-to-Cell Heterogeneity in p38-Mediated Cross-Inhibition of JNK Causes Stochastic Cell Death. Cell Rep. 2018;24:2658–68.
84. Thattai M, Oudenaarden A Van. Intrinsic noise in gene regulatory networks. PNAS. 2001;98(15):8614–9.
85. Singh A, Soltani M. Quantifying intrinsic and extrinsic variability in stochastic gene expression models. PLoS One. 2013;8(12).
86. Hilfinger A, Paulsson J. Separating intrinsic from extrinsic fluctuations in dynamic biological systems. PNAS. 2011;108(29):12167–72.
87. Iwamoto K, Shindo Y, Takahashi K. Modeling Cellular Noise Underlying Heterogeneous Cell Responses in the Epidermal Growth Factor Signaling Pathway. PLoS Comput Biol. 2016;12(11):1–18.
88. Filippi S, Barnes CP, Kirk PDW, Kudo T, Kunida K, McMahon SS, et al. Robustness of MEK-ERK Dynamics and Origins of Cell-to-Cell Variability in MAPK Signaling. Cell Rep. 2016;15(11):2524–35.
89. Linderman JJ. Modeling of G-protein-coupled receptor signaling pathways. J Biol Chem. 2009;284(9):5427–31.
90. Eungdomrong, Narat J. and Iyengar R. Modeling Cell Signaling Networks. Biol Cell. 2004;96(5):355–62.

91. Lee D, Ding Y, Jayaraman A, Kwon J. Mathematical Modeling and Parameter Estimation of Intracellular Signaling Pathway: Application to LPS-induced NFκB Activation and TNFα Production in Macrophages. Processes. 2018;6(21):1–19.
92. Gillespie DT. Exact stochastic simulation of coupled chemical reactions. J Phys Chem. 1977;81(25):2340–61.
93. Gillespie DT. A general method for numerically simulating the stochastic time evolution of coupled chemical reactions. J Comput Phys. 1976;22:403–34.
94. Sumit M, Takayama S, Linderman JJ. New insights into mammalian signaling pathways using microfluidic pulsatile inputs and mathematical modeling. Integr Biol. 2017;9(1):6–21.
95. Wang DG, Wang S, Huang B, Liu F. Roles of cellular heterogeneity, intrinsic and extrinsic noise in variability of p53 oscillation. Sci Rep. 2019;9:1–11.
96. Cheng Z, Taylor B, Ourthiague DR, Hoffmann A. Distinct single-cell signaling characteristics are conferred by the MyD88 and TRIF pathways during TLR4 activation. Sci Signal. 2015;8(385).
97. Ooi HK, Ma L. Modeling heterogeneous responsiveness of intrinsic apoptosis pathway. BMC Syst Biol. 2013;7(65):1–18.
98. Yao J, Pilko A, Wollman R. Distinct cellular states determine calcium signaling response. Mol Syst Biol. 2016;12(12):894.
99. Regot S, Hughey JJ, Bajar BT, Carrasco S, Covert MW. High-sensitivity measurements of multiple kinase activities in live single cells. Cell. 2014;157(7):1724–34.
100. Kudo T, Jeknic S, Macklin DN, Akhter S, Hughey JJ, Regot S, et al. Live-cell measurements of kinase activity in single cells using translocation reporters. Nat Protoc. 2017;13(1):155–69.

Chapter 2 Short-term Cellular Memory Tunes the Signaling Responses of the Chemokine Receptor CXCR4

This chapter is a published work:

Spinosa PC, Humphries BA, Lewin Mejia D, Buschhaus JM, Linderman JJ, Luker GD, et al. Short-term cellular memory tunes the signaling responses of the chemokine receptor CXCR4. Sci Signal. 2019;12(589).

2.1 Abstract

The chemokine receptor CXCR4 regulates fundamental processes in development, normal physiology, and diseases including cancer. Small subpopulations of CXCR4-positive cells drive the local invasion and dissemination of malignant cells during metastasis, emphasizing the need to understand the mechanisms controlling responses at the single cell level to receptor activation by the chemokine ligand CXCL12. Using single cell imaging, we discovered that short-term cellular memory of changes in environmental conditions tuned CXCR4 signaling to Akt and ERK, two kinases activated by this receptor. Conditioning cells with growth stimuli before CXCL12 exposure increased the number of cells that initiated CXCR4 signaling and the amplitude of Akt and ERK activation. Data-driven, single-cell computational modeling revealed that growth factor conditioning modulated CXCR4-dependent activation of Akt and ERK by decreasing extrinsic noise (pre-existing cell-to-cell differences in kinase activity) in PI3K and mTORC1. Modeling established mTORC1 as critical for tuning single-cell responses to CXCL12-CXCR4 signaling. Our single-cell model predicted how combinations of extrinsic noise in PI3K, Ras, and mTORC1 superimposed on different driver mutations in the ERK and/or Akt pathways to bias CXCR4 signaling. Computational experiments correctly predicted that selected kinase inhibitors used for cancer therapy shifted subsets of cells to states that were more permissive to CXCR4 activation, suggesting that such drugs may inadvertently potentiate pro-metastatic

CXCR4 signaling. Our work establishes how changing environmental inputs modulate CXCR4 signaling in single cells and provides a framework to optimize the development and use of drugs targeting this signaling pathway.

2.2 Introduction

Pre-existing cellular states, rather than stochasticity, dictate the ability of individual cells to signal in response to an input stimulus (1). Because of variations in pre-existing states, individual cells within a population exhibit heterogeneous activation of signaling pathways, and subsets of cells expressing the target receptor fail to signal at all in response to uniform input of a specific ligand (2–8). The fact that extracellular ligand may not activate signaling through a target receptor confounds reliability of biomarkers based on protein expression instead of function for selection of targeted drugs. Additional heterogeneity in signaling outputs arises because cells adapt signaling responses based on changes in environmental conditions over time, indicating that context shapes plasticity in pre-existing cellular states. Context-dependent flexibility and intercellular heterogeneity in signaling allows single cells to survive under stressful conditions, hampering the ability to treat cancer and other diseases in which subpopulations of cells drive critical steps in pathogenesis. Discovering mechanisms that shift cells to states that are more or less responsive to receptor signaling promises to improve the ability to control cell behaviors for therapy and optimize responses to molecularly-targeted drugs.

We focused on identifying mechanisms underlying responsiveness of cells to signal through chemokine receptor CXCR4 and its ligand, CXCL12. CXCL12-CXCR4 binding is essential for normal development and also promotes cancer initiation and metastasis in more than 20 different malignancies (9–11). We previously observed that only a small subset of CXCR4-positive cells migrates toward a uniform gradient of CXCL12 (12), making this ligand-receptor pair an ideal model to investigate cellular states controlling heterogeneous signaling. The CXCR4 inhibitor balixafortide has shown promising results in a Phase I clinical trial as an adjuvant therapy for advanced metastatic breast

cancer (13), reinforcing the need to understand signaling through this receptor to help identify patients likely to respond to this therapy and potential causes for treatment failure. CXCR4 activates the downstream effector kinases Akt and ERK, which mediate cell proliferation, survival, and chemotaxis (14). Akt and ERK are components of the most commonly activated oncogenic signaling pathways [phosphatidyl-inositol-3-kinase (PI3K)/Akt/mTOR and mitogen activated protein kinase (MAPK)] in cancer (14,15). Thus, understanding how cells edit responsiveness to CXCR4 signaling to Akt and ERK will advance our understanding of cell signaling and inform clinical applications of CXCR4-targeted therapies.

We combined single-cell fluorescent reporters and single-cell computational modeling to identify mechanisms through which changes in environmental conditions modulate CXCL12-CXCR4 signaling. Recent signaling inputs shift the intracellular state based on extrinsic noise in PI3K, Ras, and mTORC1, generating a short-term cellular memory that regulates subsequent CXCR4-mediated signaling to Akt and ERK. The computational model predicted how intersections among genetic mutations in pathway components, growth factor-induced cellular memory, and kinase inhibitors tune the ability of cells to signal through CXCR4. These data provide new insights into how cells adapt to dynamic changes in environmental conditions and how clinical treatments alter cell states and signaling by CXCR4.

2.3 Methods

2.3.1 Cell Culture

We cultured the breast cancer cell lines MDA-MB-231, which express constitutively active KRAS and BRaf (16), and SUM-159, which express constitutively active PI3K and HRAS (16), as described previously (17). Vari-068 cells (a gift from Sofia Merajver, University of Michigan) are patient-derived, triple-negative breast cancer cells adapted to cell culture. These cells have an inactivating mutation in *PTEN*. We cultured these cells as described previously (18). In the conditioning phase of our experiments, we

cultured control cells in low (1%) FBS media to suppress proliferation, thereby reducing the effects of cell cycle on signaling heterogeneity.

2.3.2 Fluorescent reporter construction

We constructed the kinase translocation reporter plasmid, pHAEP, in a PiggyBac transposon vector with CAG promoter based in part on plasmid pHGEA (gift of K. Aoki, Okazaki Institute for Integrative Bioscience) (19). To optimize two-photon imaging of KTR reporters for Akt and ERK we fused the kinase substrates to fluorescent proteins Aquamarine (20) and mCitrine (21), respectively and replaced the histone-2B marker with mCherry to improve brightness and photostability. We also replaced the IRES to blasticidin resistance marker with a P2A sequence followed by a puromycin resistance marker. We assembled the plasmid using HiFi assembly (NEB, Ipswich, MA, USA) with synthetic double stranded DNA fragments (GenBlocks, IDT, Coralville, IA, USA) or double stranded DNA amplified from pHGEA as illustrated in Figure A1 A. We constructed the CXCR4-mTagBFP2 (Evrogen, Moscow, Russia) in lentiviral expression vector pLVX-Ef1α (Clontech/Takara, Kusatsu, Shiga, Japan).

2.3.3 Cell engineering

To generate cells stably expressing the pHAEP construct, we co-transfected each cell line with the pHAEP transposon and Super PiggyBac transposase vector (System Biosciences, Palo Alto, CA, USA) using FuGene HD (Promega, Milwaukee, WI, USA). We selected batch populations of stable cells with 4 µg/ml puromycin. For MDA-MB-231 and SUM-159 cells, we transduced cells stably expressing the pHAEP reporter with lentiviral vector for CXCR4-mTagBFP and sorted BFP-positive cells by flow cytometry.

2.3.4 Time-lapse two photon microscopy and image processing

To prepare cells for time-lapse microscopy, we seeded cells (1.2×10^5 MDA-MB-231 cells, 6.5×10^4 SUM159 cells, or 2.0×10^5 Vari-068 cells) in 35 mm dishes with a 20 mm glass bottom (Cellvis, Mountain View, CA, USA) in 2 ml of imaging base media (FluoroBrite DMEM media (A1896701, ThermoFisher Scientific, Waltham, MA USA),

1% GlutaMax, 1% PenStrep and 1% sodium pyruvate) supplemented with 10% FBS (HyClone). For SUM-159 cells, we also added 0.05% insulin (Sigma I9278) and 0.01% hydrocortisone (10mg/ml, 70% ethanol/water). Forty-eight hours after seeding, we changed to 1% FBS in imaging base media for all cell types. On the next day, four hours before imaging, we conditioned cells by adding 200 µl FBS (final concentration 10%), EGF (final concentration 1, 10 or 30 ng/ml) (R&D Systems, Minneapolis, MN, USA), ridaforolimus (Selleck Chemicals, Houston, TX, USA) (final concentration 10 nM), or trametinib (Selleck Chemicals) (final concentration 100 nM) to their existing media. For extended conditioning, we added 200 µl FBS seven hours prior to imaging.

We imaged cells with an Olympus FVMPE-RS upright microscope, 25x NIR-corrected objective, and four channel detection (blue, cyan, yellow, red) with a live cell imaging chamber (Okolab, San Bruno, CA, USA). Laser settings were: mTagBFP2 excitation at 800 nm, laser power 6%; Aquamarine and mCitrine excitation 920 nm, laser power 6%; and mCherry excitation 1040, laser power 11%. We optimized the fluorophores, optical filters, and scan protocol to achieve negligible crosstalk between detector channels. We acquired four emission channels with pairs of detectors separated by a 552 nm dichroic mirror. We collected blue (channel 1) and cyan (channel 2) emissions with the following filters and dichroic mirror: channel 1 435/50 nm, channel 2 480/40 nm, and 485 nm dichroic mirror). We collected yellow (channel 3) and red (channel 4) emissions (light > 552 nm) with the following filters and dichroic mirror: channel 3 540/40 nm, channel 4 641/75 nm, and 596 nm dichroic mirror). The microscope is equipped with tunable IR laser and a fixed 1040 nm laser. We acquired initial images of CXCR4-BFP with simultaneous excitation at 800 nm (mTagBFP) and 1040 nm (mCherry). We then immediately acquired repeated scans using sequential excitation by line at 920 nm (aquamarine and mCitrine) and 1040 nm (mCherry). We acquired images as a multi-area time lapse scanned every two minutes for four images prior to addition of CXCL12 (10 ng/ml final concentration) and every two minutes thereafter for a total of 1 hour. We developed custom MATLAB code to automatically segment cells; calculate the KTR cytoplasmic to nuclear ratio in each cell; measure intensity of CXCR4-mTagBFP; and track individual cells. The segmentation algorithm identified nuclei with adaptive

thresholding followed by watershed segmentation. The extended minima from the nuclear watershed were used to seed watershed segmentation of a mask of the combined KTR channels, which yielded cytoplasmic segmentation in good agreement with the contours of individual cells in confluent monolayers. Nuclei were used for tracking individual cells during the time lapse imaging. For KTR reporters, we calculated the ratio of median fluorescence intensities in cytoplasm to the nucleus (CNR), expressed as the $\log_2$ of the CNR, and output data as pairs of Akt and ERK KTR measurements for each cell with a complete time track (generally 300 to 500 cells per image). For cells engineered to express CXCR4-mTagBFP, we used only cells with detectable blue fluorescence for computational modeling. We discarded from the analysis the small number of cells undergoing mitosis during imaging because we could not track identities of these cells throughout the entire time course of an experiment.

2.3.5 Computational model: receptor dynamics

We constructed a computational conditional signaling model (CSM) of CXCR4-mediated Akt and ERK signaling using ordinary differential equations to generate predicted signaling outcomes. The CSM contains receptor, signaling, and reporter dynamics. A schematic including all connectivity in the CSM is drawn in Figure A3. All equations, parameters, and initial conditions can be found in Appendix Tables A1-A5.

Receptor dynamics (CXCR4 trafficking following CXCL12 stimulation) are as described previously (22–24). Briefly, CXCL12 in the extracellular space binds to CXCR4. Upon receptor phosphorylation and β-arrestin recruitment to the plasma membrane, the receptor-ligand complex is internalized, trafficked to endosomes, and destined for degradation. Because β-arrestin is an adapter protein ubiquitously involved in desensitizing many different GPCRs (25,26), we assume it is in large excess and do not model it explicitly. CXCR4 not bound to CXCL12 can be internalized upon phosphorylation and β-arrestin recruitment, but the receptor is recycled to the cell surface rather than degraded.

2.3.6 Computational model: signaling dynamics

The CXCR4-CXCL12 complex promotes signaling through Akt and ERK in a mechanism involving feedback loops and crosstalk that restrain signaling. The model includes a cascade of events leading to phosphorylation of ERK and both the Thr^{308} and Ser^{473} sites in Akt needed for full activation (27–29). The PI3K/Akt pathway is initiated when CXCL12-CXCR4 complexes, whether phosphorylated or not, promote G-protein activation (30). To account for both ligand-independent and non-CXCL12 induced G-protein activation, we incorporated a basal rate of G-protein activation. Activated G-proteins organize subunits of phosphoinositide 3-kinase (PI3K) into their active state (31). Activated PI3K phosphorylates the membrane lipid PIP_2 to form PIP_3 (31,32). PIP_3 has two major roles in Akt signaling. First, it activates PDK1 by binding and forming a complex. The active form of PDK1 recruits and phosphorylates Thr^{308} in Akt, phosphorylated or not at Ser^{473} (32,33). The Ser^{473} site in Akt is activated by a separate kinase, mTORC2. We assumed that phosphorylation of either site in Akt is independent of the phosphorylation of the other, consistent with Pezze *et al.* (33). mTORC2 activation is generally thought to be PI3K-dependent (34,35). In our model, we proposed that mTORC2 is activated and recruited to the plasma membrane by PIP_3, the second role for this lipid in the model and consistent with the results of Gan *et al.* (36). mTORC1 opposes mTORC2 formation (37). Although many studies have emphasized the importance of mTORC1 opposing PI3K formation through IRS-1 and thus halting mTORC2 formation (38,39), mTORC1 can more directly inhibit mTORC2 formation. The subunit on mTORC2 that promotes docking to PIP_3 and thus mTORC2 activation, mSIN1, is phosphorylated and inactivated by a target of mTORC1, activated and phosphorylated S6K (40,41). This phosphorylation event detaches mSIN1 from mTORC2, preventing mTORC2 from attaching to the plasma membrane and becoming activated (42). These dynamics closely follow uncompetitive inhibition. Therefore, we model the activation of mTORC2 with PIP_3 acting as the enzyme, inactive mTORC2 as the substrate, and mTORC1 as an uncompetitive inhibitor. Akt phosphorylated at both Thr^{308} and Ser^{473} and phosphorylated ERK promote mTORC1 activation (43–45). This activation involves many species, including TSC1/2 and RHEB, which were not

modeled here explicitly for simplicity. Instead, we assumed that Akt phosphorylated at both Thr^{308} and Ser^{473} and phosphorylated ERK promote activation of mTORC1.

The MAPK signaling pathway is initiated with activation of Ras by active G-proteins (46). Because mTORC1 can oppose activation of Ras (47), we incorporated this relationship in our model. Without mTORC1 inhibition of Ras activation, the model did not accurately recapitulate coordinate regulation of Akt and ERK dynamics. Ras promotes activation of the Raf/MEK complex (48). MDA-MB-231 cells also have a Raf mutation, for which we accounted with a GPCR-independent Raf activation reaction and by setting this parameter to 0 when modeling cells without this mutation. Additionally, Raf is inhibited by active Akt (49). Activated Raf/MEK promotes the phosphorylation of ERK (50). Other previously reported negative feedback mechanisms, such as feedback from ERK to Sos, Raf, and MEK, were lumped into ERK activation rate constants and were not included explicitly in the CSM because they were not required to reproduce critical behaviors seen in our experiments.

2.3.7 Computational model: reporter dynamics

To connect active kinase concentrations (Akt phosphorylated at both Thr^{308} and Ser^{473} and phosphorylated ERK) to their respective reporters in the CSM, we use a set of published ordinary differential equations (51). Briefly, the reporters exist in two locations, the nucleus or cytoplasm, and have two states in both locations, phosphorylated or unphosphorylated. The reporters are phosphorylated and dephosphorylated according to Michaelis-Menten kinetics and are transported between nucleus and cytoplasm by mass action kinetics. To determine the CNR in individual cells in our model, we calculated the ratio of each reporter (phosphorylated and unphosphorylated) in the cytoplasm to the nucleus, and we expressed this variable in $\log_2$ format. The single-cell cytoplasmic to nuclear ratio (CNR) of each reporter was the output of our model.

2.3.8 Computational model: extrinsic noise

Extrinsic noise is now appreciated as a major driver of cell signaling heterogeneity (43,52–54). In the CSM, extrinsic noise encompassed cellular conditions driven by mutations, metabolism, mitogenic signals, or any other external force acting on signaling components. The model incorporated extrinsic noise in three molecules, PI3K, Ras, and mTORC1, to predict the heterogeneous single-cell CXCR4-mediated Akt and ERK responses. A first-order rate constant for each of these molecules describes their activation independently of CXCR4 signaling. One important assumption of this approach is that the extrinsic noise rate parameters were constant over the time frame of our experiments. We believed that this assumption was reasonable because CXCR4 signaling activated PI3K, Ras, and mTORC1 dynamically by the explicit mechanisms in the CSM rather than by the extrinsic noise terms, which incorporated signaling not due to CXCR4 stimulation. Values for the extrinsic noise rate constants for PI3K, Ras, and mTORC1 could not be compared directly because they depended on the inactive states of each respective kinase, which existed in different concentrations in the cell. Because we modeled the activation of all kinases from their respective inactive states in the ERK and Akt signaling cascades, the concentration of each active kinase approached the total concentration of each kinase in the cell as the extrinsic noise rate parameter increases.

2.3.9 Computational model: solution and calibration

The CSM was solved using MATLAB function *ode15s*. At the start of a simulation, the model was run in the absence of CXCL12 to calculate the steady-state concentrations of all model species. Next, a dose of CXCL12 was given and downstream signaling dynamics occurred as described above and by the differential equations in Appendices A2-A3.

First-pass model parameters were obtained from literature as documented in Appendix Table A4. We performed Latin Hypercube sampling (LHS) (55) as a search strategy for efficient parameter selection using the first-pass model parameters and a +/- 50% variation to find a suitable baseline parameter set. We used moderate values for

extrinsic noise parameters and performed a least-square fit to calibrate the model to the mode cell in the experiment with control conditioned MDA-MB-231 cells treated with 10 ng/ml CXCL12 to find a baseline parameter set that could span the range of responses using only variation in extrinsic noise rate parameters. We then used the same baseline parameter set for every cell in all of our simulations, and varied only the three extrinsic noise rate parameters to generate signaling heterogeneity.

2.3.10 Determining the conditional signaling state of experimental cells

By varying the extrinsic noise parameters for PI3K, Ras, and mTORC1, we used the CSM to generate over 12,000 possible CXCR4-mediated Akt and ERK responses. To determine the conditional state of cells in our experiments, we calculated the residuals of each paired Akt and ERK experimental cell response to each of the predicted paired Akt and ERK responses from the CSM. We determined the conditional state of each experimental cell from the predicted cell to which it shared the minimum squared residual. In this manner, each individual experimental cell was now associated with a set of extrinsic noise parameters $\{k_{PI3K}, k_{Ras}, k_{mTORC1}\}$ that defined the conditional signaling state of that cell predicted by the CSM. Occupancy maps in Figures 2.4-2.6 and Figure A6 B are an illustration of the probability of experimental cells occupying a conditional state in the CSM. For each cell in an experiment, we calculated a fit score which was the reciprocal of the sum of the squared residuals for experimental Akt and ERK KTRs compared with the simulated Akt and ERK KTR at each conditional state in the CSM. We normalized fit scores for each experimental cell to their sum over all CSM conditional states. We set a lower bound (0.0005) below which fit scores were set to 0. We calculated the probability of occupancy of each CSM conditional state as the sum of the fit scores for all cells at that condition, normalized to the sum of fit scores for all cells to all CSM conditional states. For illustration purposes, these values were multiplied by one million cells.

2.4 Results

2.4.1 Growth factor conditioning potentiates subsequent CXCR4 signaling

CXCL12 signaling through CXCR4 activates the mitogen activated protein kinase (MAPK) and phosphatidylinositol-3-kinase (PI3K) pathways (Figure 2.1A). These pathways activate ERK and Akt, respectively. To capture CXCR4 signaling to ERK and Akt in single cells, we stably expressed fluorescent reporters that measured the activities of these kinases (kinase translocation reporters, KTRs) (51,56). KTRs reversibly translocate from nucleus to cytoplasm based on the phosphorylation of a specific substrate for each kinase. Quantifying the ratios of fluorescence intensities in cytoplasm to nucleus provides analog, independent measurements of kinase activity for ERK and Akt in single cells. Reporter-expressing breast cancer cells stably expressed histone 2B fused to mCherry (H2B-mCherry) to mark the cell nuclei and enable image segmentation and analysis and CXCR4 fused to a blue fluorescent protein (CXCR4-mTagBFP), allowing us to identify levels of tagged CXCR4 in each cell (Figure A1 A).

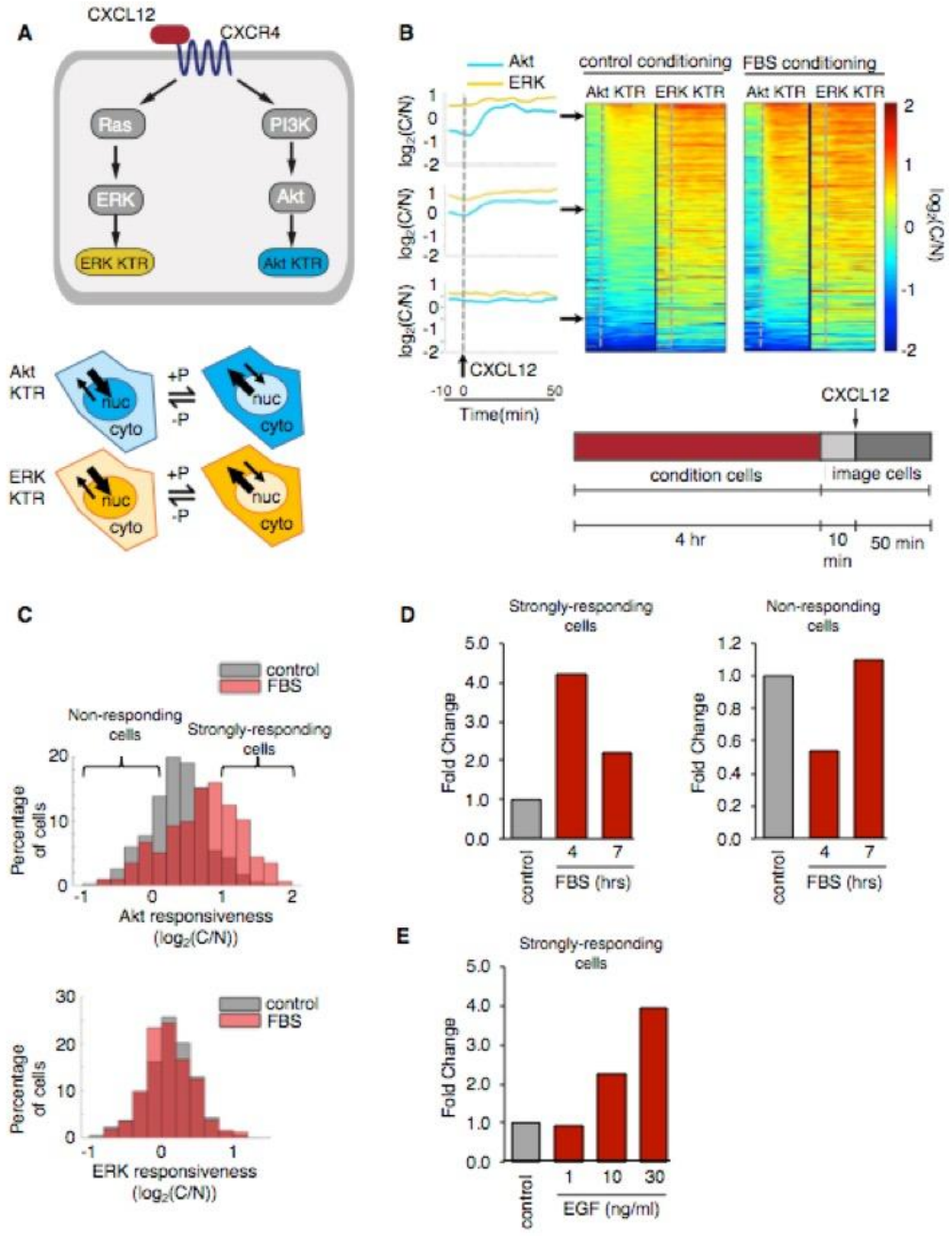

Figure 2.1 Conditioning cells with a growth stimulus potentiates subsequent CXCR4 signaling

(A) CXCL12 binds to CXCR4 and elicits downstream Akt and ERK activation. Separate kinase translocation reporters (KTRs) for Akt (aquamarine) and ERK (citrine) were stably expressed in breast cancer cells. Phosphorylation and dephosphorylation of the kinase substrate drives the reporter into the cytoplasm or nucleus, respectively. (B) Cells were conditioned for 4 hours with or without growth stimuli or kinase inhibitors.

Single-cell, time-lapse imaging was performed for 10 minutes before and 50 minutes after addition of 10 ng/ml CXCL12. Single cell time tracks (control conditioning: n=347 cells, FBS conditioning: n=312 cells) show CXCR4-dependent activation of Akt and ERK in MDA-MB-231 breast cancer cells quantified as $\log_2$ of cytoplasmic to nuclear ratio (C/N) of fluorescence intensities for each KTR in individual cells and displayed on a pseudocolor scale. (C) Quantification of Akt and ERK activation in cells conditioned with FBS before CXCL12 stimulation (control conditioning: n=347 cells, FBS conditioning: n=312 cells). Strong activation was defined by ≥ 1 increase in $\log_2$(C/N) unit. (D) Quantification of Akt and ERK activation in cells conditioned with FBS for 4 (n=312 cells) or 7 (n=367 cells) hours compared to control conditioning (n=347 cells) before CXCL12 stimulation). (E) Quantification of Akt and ERK activation in cells that were conditioned with various concentrations of epidermal growth factor (EGF) for 4 hours before CXCL12 stimulation (control conditioning: n=347cells, 1ng/ml EGF conditioning: 354 cells, 10ng/ml EGF conditioning: 370 cells, 30ng/ml EGF conditioning: 358 cells).

Using live-cell imaging to quantify the dynamics of Akt and ERK KTRs in single cells, we observed heterogeneous CXCR4 signaling in MDA-MB-231 breast cancer cells treated with 10 ng/ml CXCL12 as the only stimulus (Figure A1B). Single-cell responses ranged from strong activation of both Akt and ERK to undetectable signaling despite expression of CXCR4 (Figure 2.1B). MDA-MB-231 cells typically exhibited greater activation of Akt than ERK because mutant KRas and BRaf (16) in these cells constitutively drive ERK signaling, reducing the dynamic range for activation by CXCR4.

Because cells under normal physiological conditions signal in the context of multiple signaling inputs, we hypothesized that treatment of cells with a different growth factor would generate a short-term memory (57) that modified subsequent CXCL12-CXCR4 signaling. To test this hypothesis, we conditioned cells for four hours with fetal bovine serum (FBS) before adding CXCL12. FBS conditioning produced a transient increase in Akt activity that resolved essentially to baseline within four hours, returning cells to an imaging appearance indistinguishable from control (Figure A1C). Single-cell time-tracks showed that FBS conditioning increased by four-fold the number of MDA-MB-231 cells with strong activation of Akt in response to CXCL12 (Figure 2.1B-D). FBS conditioning also reduced the number of non-responding cells by 50%. Conditioning with FBS did not substantially alter the activation of ERK by CXCL12-CXCR4 signaling likely because of constitutive activation of this kinase in MDA-MB-231 cells (Figure 2.1B-D). Extending

FBS conditioning to seven hours before adding CXCL12 produced only a two-fold increase in cells with strong activation of Akt and did not change the number of nonresponding cells, establishing a time-dependence aspect to the cellular memory of prior signaling inputs and identifying seven hours as a near-end point for this form of cell signaling memory (Figure 2.1D). We next examined the extent to which conditioning with epidermal growth factor (EGF) modified subsequent CXCL12-CXCR4 signaling responses. Similar to FBS, conditioning with various concentrations of EGF transiently activated Akt and ERK, but the activities of these kinases returned to baseline within four hours. Subsequent addition of CXCL12 increased the number of cells with strong CXCR4-mediated activation of Akt, in a manner proportional to the concentrations of EGF used for conditioning (Figure 2.1E). Regardless of experimental condition, CXCL12 did not activate Akt or ERK signaling in cells lacking CXCR4-BFP (Figure A1D-E), indicating these cells express little to no endogenous CXCR4 as we reported previously (58). The amount of CXCR4-BFP on single cells did not account for intercellular heterogeneity in signaling, and conditioning did not alter expression or localization of the fluorescent receptor (Figure A1D). These data demonstrate that prior growth stimuli tune responses of cells to CXCR4 signaling through a mechanism downstream of the receptor.

2.4.2 Computational modeling predicts single-cell signaling dynamics

The intracellular state of cells downstream of receptors involves a complex network of signaling components that is difficult to intuit with experiments alone. We hypothesized that conditioning with growth factors changed the intracellular state, thereby altering subsequent CXCR4 signaling. To uncover mechanisms that control the responsiveness of cells to CXCL12-CXCR4 beyond what experiments could alone provide, we used ordinary differential equations to construct a computational single-cell conditional signaling model (CSM) of CXCR4-mediated activation of Akt and ERK. Two key features of experimental signaling data informed the construction of the CSM. First, the lack of correlation between basal activity and CXCL12-mediated activation of either kinase in single cells (Figure A2 A-C) indicated that different regulators controlled basal kinase activity versus responses of single cells to CXCL12. Second, a trend between

activation of Akt and ERK by CXCR4 in single cells (Figure A2 A-C) suggested that a component common to both PI3K and MAPK pathways regulated the responsiveness of both kinases. We constructed the framework of the CSM based on these experimental observations and previously published data (Figure 2.2A, Figure A3).

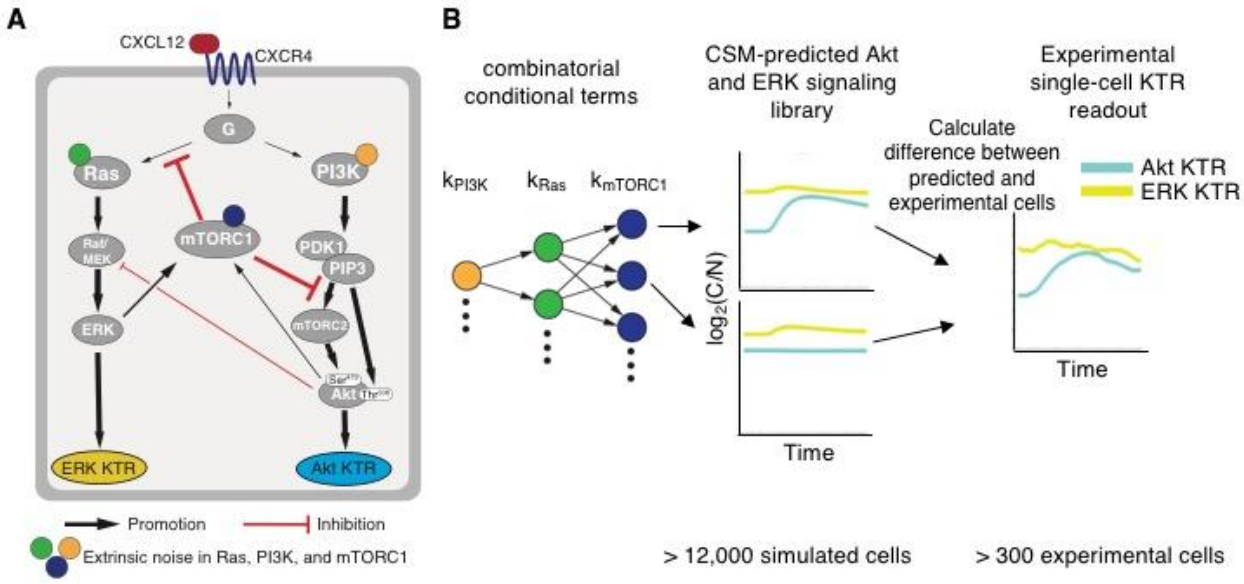

Figure 2.2 The computational conditional signaling model (CSM) predicts CXCR4-mediated Akt and ERK signaling responses, establishing a framework for understanding the range of heterogeneous signaling data

(A) The CXCL12-CXCR4 interaction elicits G-protein signaling to activate Akt and ERK but can be restrained by negative feedback and crosstalk mechanisms. mTORC1 functions as a central regulator of signaling because it can inhibit the activation of both Akt and ERK. Extrinsic noise in phosphatidylinositol-3-kinase (PI3K), Ras, and mTORC1 promotes activation of Akt and/or ERK in the absence of CXCR4-mediated signaling. Signaling kinetics cover a range of time scales with thicker arrows and lines qualitatively indicating faster reaction rates. A complete list of differential equations, initial conditions, and parameters is available in Appendix Tables A1-A5. (B) To encompass heterogeneous signaling responses of single cells in both Akt and ERK, we varied extrinsic noise parameters for PI3K, Ras, and mTORC1 in the CSM. By running combinations of these three parameters, we generated a model library of >12,000 predicted paired Akt and ERK responses. We performed a least-square fit of experimentally-determined Akt and ERK responses from the KTRs to predicted responses to derive the PI3K, Ras, and mTORC1 extrinsic noise parameters that best describe each single cell in the experiments.

In addition to CXCR4 signaling outputs (Figure 2.2A), the CSM included extrinsic noise to account for signaling heterogeneity in a cell population (2,5,52,59–61). In this context, extrinsic noise refers to pre-existing cell-to-cell differences in kinase activity. We used the two observations in the experimental data described above to determine the components of the signaling pathways that needed to contain extrinsic noise. PI3K, Ras, and mTORC1 constituted the main sources of heterogeneity in CXCR4 signaling because our data suggested that basal levels of upstream activators of Akt (PI3K) and ERK (Ras), as well as a downstream regulator common to both pathways (mTORC1), varied from cell-to-cell. Additionally, PI3K, Ras, and mTORC1 have roles external to CXCR4 signaling relating to confluency, metabolism, or local mitogenic signals (43,52,53,62). Heterogeneity was mathematically incorporated in the CSM in the form of a conditional term on these three pathway components (Figure A4) that set the baseline activities of Akt and ERK in each cell in the absence of any stimulation. We used the CSM with various combinations of extrinsic noise parameters for PI3K, Ras, and mTORC1, referred to as the conditional signaling state, to generate a library of predicted Akt and ERK signaling responses to CXCL12 independent of the presence and type of conditioning stimulus (Figure 2.2B). We used this library of predicted signaling behavior as a framework for understanding the heterogeneous signaling data seen in experiments.

2.4.3 Maps of the signaling landscape reveal that conditional signaling states control CXCR4 responsiveness

The CSM captured the paired signaling behavior of Akt and ERK in single cells across the range of responses measured experimentally in the population (Figure 2.3A). We used the CSM to generate a map of the signaling landscape displaying the conditional signaling states that permit CXCR4 activation of Akt and ERK (Figure A5). The signaling landscape reflected individual CSM simulations at all combinations of conditional signaling states. The Akt and ERK signaling landscape predicted by the CSM contains areas in which cells can activate one, both, or neither kinase (Figure 2.3B, Figure A5). Generally, the highest CXCR4 activation of Akt occurred in those conditional signaling states with low PI3K and mTORC1 activity. By comparison, the conditional signaling

states with high PI3K, low Ras, and low mTORC1 activities showed greatest CXCR4 signaling to ERK (Figure 2.3B). The CSM predicted the cellular states that were permissive for CXCR4 signaling.

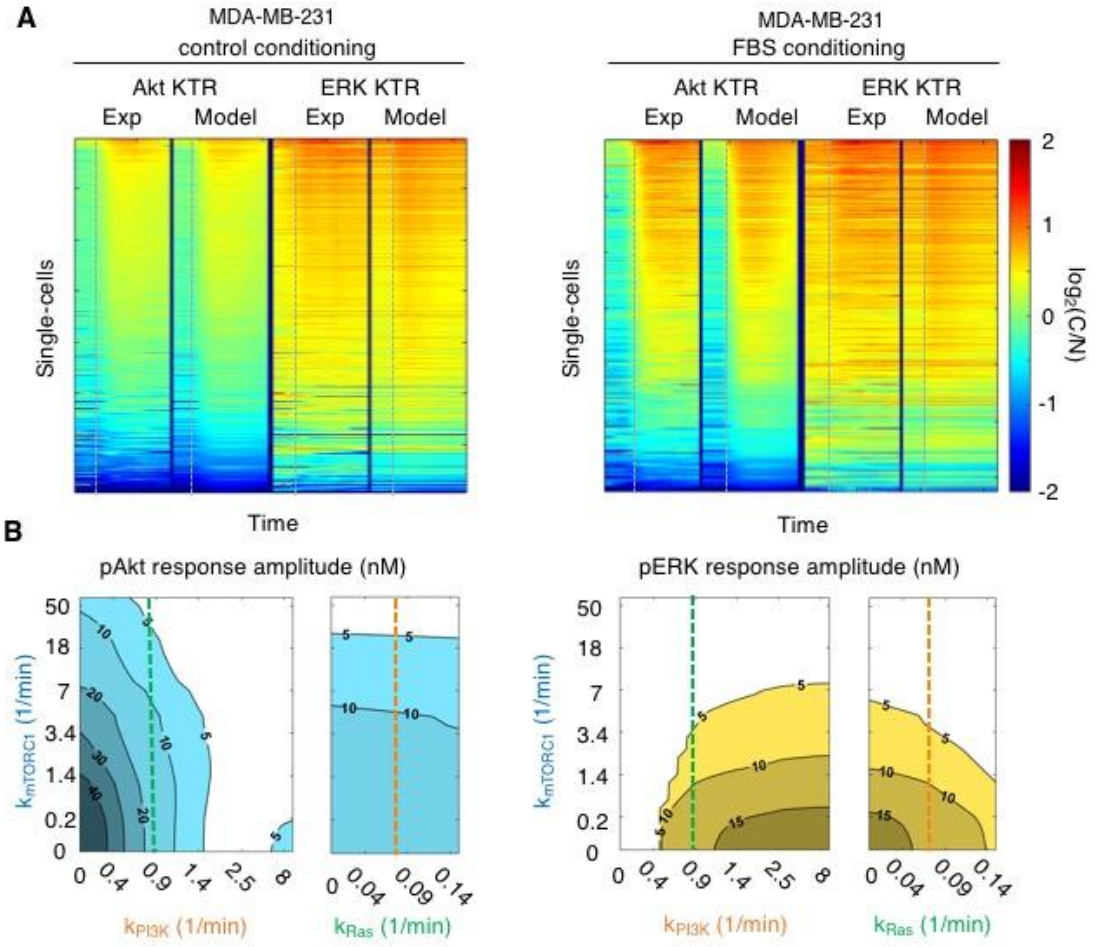

Figure 2.3 The CSM captures heterogeneous single-cell signaling responses seen in experiments and reveals the conditional signaling states controlling responsiveness to CXCR4 signaling

(A) Responses from the model library match experimentally determined control and FBS conditioned single-cell (control conditioning: n=347 cells, FBS conditioning: n=312 cells) CXCR4 signaling to Akt and ERK. Greater than 95% of cells fit the matching criteria. The gray dashed line identifies when CXCL12 was added (10 min timepoint). Images were taken every two minutes for 60 min. (B) Akt or ERK responses through CXCR4 as affected by different combinations of extrinsic noise parameters for PI3K (orange), Ras (green), and mTORC1 (blue) during simulation. Plots show a 2D plane of the entire 3D signaling landscape generated by varying three parameters (k_{PI3K}, k_{Ras},

and k_{mTORC1}) combinatorically. Green and orange dotted lines denote the value on the third axis.

2.4.4 MDA-MB-231 cells occupy tunable conditional signaling states

The CSM provides a framework to organize complex signaling behavior and extract conditional information from cell populations. We constructed occupancy maps to illustrate distributions of experimental cells in the CSM signaling landscape. Under control conditioning, MDA-MB-231 cells occupied a region of the signaling landscape with moderate PI3K, Ras, and mTORC1 activities (Figure 2.4A). Akt and ERK signaling responsiveness from Figure 2.3B is shown as the underlay on the occupancy maps and illustrates regions of the signaling landscape containing cells in which CXCR4 activates Akt and/or ERK. When conditioned with FBS for four hours before CXCL12 stimulation, MDA-MB-231 cells shifted to a region of the signaling landscape with lower PI3K and mTORC1 activities, which favored CXCR4-mediated activation of Akt (Figure 2.4B). Using the CSM-predicted Akt and ERK signaling behaviors that matched experimental data, the percentage of cells activating Akt in response to CXCL12 increased after FBS conditioning compared to control (Figure 2.4C). Conditioning with three different concentrations of EGF also decreased PI3K and mTORC1 activities in a dose-dependent manner compared to control (Figure A6 A, B). We conclude that conditioning cells with growth factors alters the conditional signaling states consistent with a decrease in PI3K and mTORC1 activity. These shifts in conditional signaling state provide a mechanism underlying the ability of growth factor conditioning to enhance numbers of cells responding to CXCL12 and amplitude of signaling to Akt.

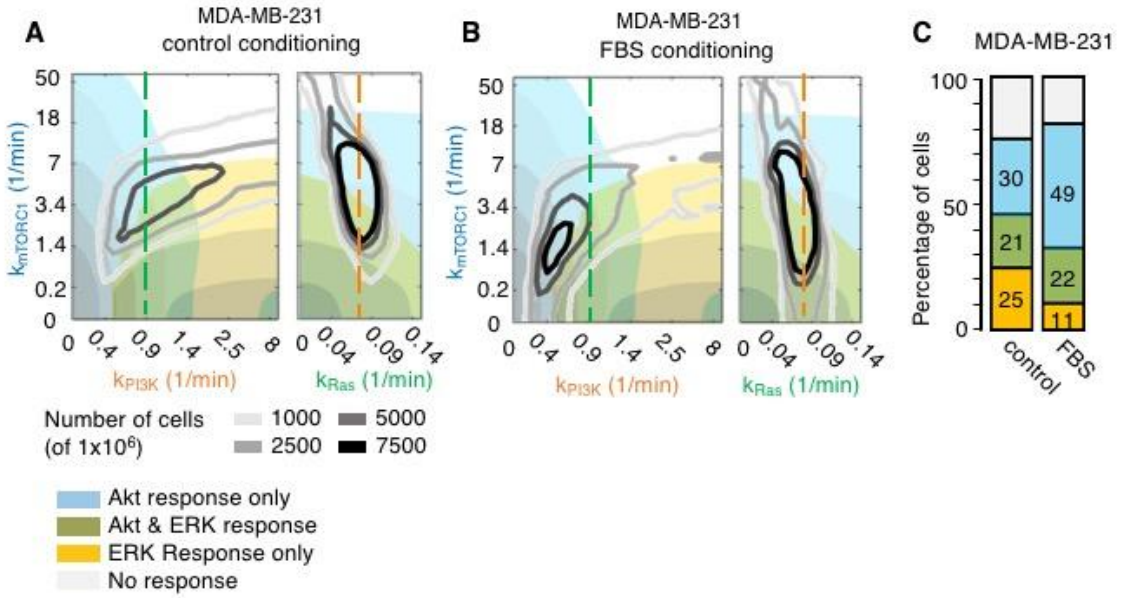

Figure 2.4 FBS conditioning shifted the conditional signaling state of MDA-MB-231 breast cancer cells to a region more permissive to CXCL12-CXCR4 signaling to Akt

(A to C) Occupancy maps (normalized to contain 1 x 10^6 cells) illustrate combinations of extrinsic noise parameters (conditional signaling state) corresponding to regions of 3D signaling landscape (CSM output) where experimental cells most frequently match. Contour lines display numbers of cells out of 1 x 10^6. Occupancies were summed in the third dimension for purposes of viewing the map in two dimensions. Cyan and yellow underlays illustrate regions of responsiveness for Akt and ERK, respectively. Green and orange lines illustrate the specific Ras and PI3K planes, respectively, corresponding to the responsiveness underlays. Occupancy maps are shown for MDA-MB-231 cells that received control conditioning (A) or FBS conditioning (B) before CXCR4 stimulation. (C) Quantification of cells with each signaling response. We defined responses in the computational model as >5 nM increases in kinase activity for Akt or ERK.

2.4.5 Vari-068 and SUM-159 cells occupy tunable conditional signaling states distinct from MDA-MB-231 cells

In contrast to MDA-MB-231 cells, many breast cancers harbor mutations in upstream activators of Akt (63). We tested the CSM on cells with constitutive activation of signaling to Akt, which we expected to occupy different conditional states in the signaling landscape than MDA-MB-231 cells. In patient-derived Vari-068 cells with mutant PTEN, CXCR4 signals primarily through ERK rather than Akt (Figure A6 C),

which is distinct from MDA-MB-231 cells. Vari-068 cells occupy a region of the signaling landscape with high PI3K and moderate Ras (Figure 2.5A). Because PTEN degrades phosphatidylinositol-3,4,5-phosphate (PIP_3) and a loss-of-function mutation in PTEN is present in Vari-068 cells, the model represented Vari-068 cells as having high PI3K activity. When conditioned with FBS for four hours before the addition of CXCL12, Vari-068 cells shifted to a region of the signaling landscape with lower mTORC1 but similar PI3K and Ras activities (Figure 2.5B). Cells in this state showed potentiated ERK signaling (Figure 2.5C, Figure A6 C). These results define a signaling paradigm in which mTORC1 controls overall cellular permissiveness for CXCR4 signaling, and conditioning with growth factors reduces mTORC1-mediated restraint mechanisms on ERK and Akt signaling. Conditioning breast cancer cells with growth factors decreases PI3K and mTORC1 activity to potentiate subsequent CXCR4-mediated signaling to Akt and ERK but cannot overcome activating mutations in upstream components of these pathways. Genetic mutations define the subset of conditional signaling states available to cells, but conditioning with growth factors further tunes the signaling state of any single cell.

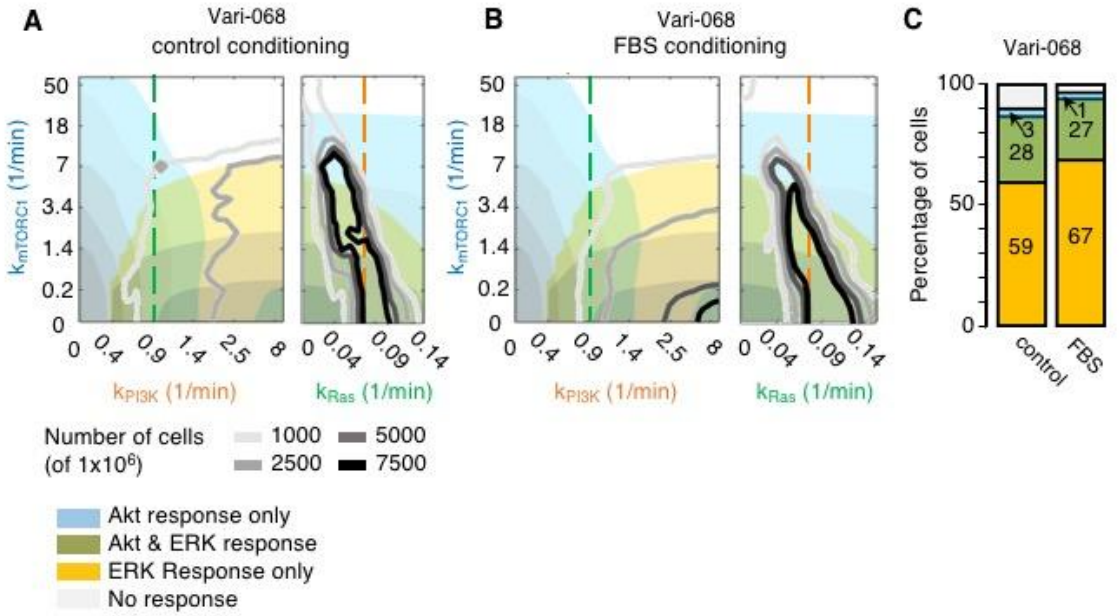

Figure 2.5 Genetic mutations set the subset of conditional states available to cells, but these states can be tuned to further edit signaling behavior

(A) Occupancy map shown as contour lines is a 3D histogram which (normalized to contain 1 x 10^6 cells) illustrates combinations of extrinsic noise parameters (conditional signaling state) corresponding to regions of the 3D signaling landscape (CSM output) where experimental cells most frequently match. Cyan and yellow underlays illustrate regions of responsiveness for Akt and ERK, respectively. Green and orange lines illustrate the specific Ras and PI3K planes, respectively, corresponding to the responsiveness underlays. Occupancy map shown for patient-derived Vari-068 cells (which have an inactivating mutation in PTEN) that received control conditioning before CXCR4 stimulation. (B) Occupancy map shown as contour lines (normalized to contain 1 x 10^6 cells) illustrates combinations of extrinsic noise parameters corresponding to regions of the 3D signaling landscape where experimental cells most frequently match. Cyan and yellow underlays illustrate regions of responsiveness for Akt and ERK, respectively. Green and orange lines illustrate the specific Ras and PI3K planes, respectively, corresponding to the responsiveness underlays. Occupancy maps are shown for patient-derived Vari-068 cells that received FBS conditioning before CXCR4 stimulation. (C) Quantification of cells with each signaling response. We defined responses from the computational model as >5 nM increases in kinase activity for Akt or ERK.

We next investigated the extent to which CXCR4 signals to Akt and ERK in cells with activating mutations in both PI3K and MAPK pathways. Similar to Vari-068 cells, CXCR4 in SUM-159 cells, which have constitutively active HRas (an upstream activator of ERK) and PI3K, signals primarily to ERK rather than Akt (Figure 2.6A-B, Figure A6 C), indicating that the ERK pathway remains inducible in the presence of an upstream activating mutation. SUM-159 cells occupy a region of the signaling landscape with high PI3K activity due to the activating mutation in this kinase and moderate Ras and mTORC1 activities (Figure 2.6A). The CSM revealed that despite activating mutations in both MAPK and PI3K pathways, the PI3K/Akt pathway generally dominated and was almost uninducible by CXCL12 in these cells. Signaling in breast cancer cells with genetic mutations in Akt, ERK, or both is therefore tuned both by these mutations and growth factor availability. A summary cartoon illustrates the conditional states of the breast cancer cell types we tested, showing how genetic mutations and growth factor conditioning stimuli shift cell signaling states to various regions of the signaling landscape (Figure 2.6C). Genetic mutations dictate the subset of conditional signaling

states available from the set of all possible states predicted from the CSM, and growth factor availability further tunes the states within that subset that single cells will occupy.

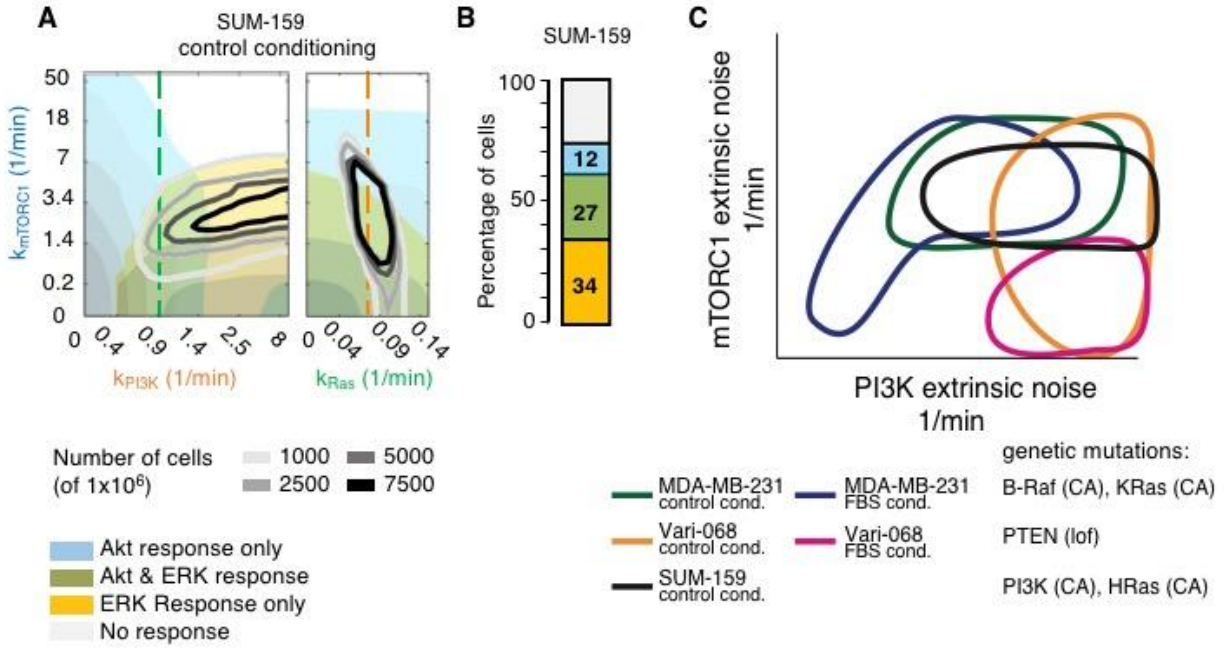

Figure 2.6 SUM-159 cells occupy conditional signaling states with ERK responsiveness

(A) Occupancy map shows where experimental cells most frequently match model predictions. Cyan and yellow underlays illustrate regions of responsiveness for Akt and ERK, respectively. Green and orange lines illustrate the specific Ras and PI3K planes, respectively, corresponding to the responsiveness underlays. Occupancy map is shown for SUM-159 cells (which have activating mutations in both ERK and Akt) that received control conditioning. (B) Summary of the percentage of cells with each signaling response. We defined responses from the computational model as >5 nM increases in kinase activity for Akt or ERK. (C) A summary of how genetic mutations and growth factor conditioning interact to tune cellular responsiveness in Akt and ERK by shifting the conditional signaling state at the single-cell scale. CA: constitutive activation; lof: loss of function.

2.4.6 MEK inhibition potentiates subsequent CXCR4-mediated Akt signaling in a subset of cells

We applied the CSM to predict the responsiveness of cells treated with two therapeutic agents relevant to CXCR4 signaling, the MEK inhibitor trametinib and the mTORC1 inhibitor ridaforolimus. The CSM predicted that conditioning with trametinib would block

ERK signaling but potentiate CXCR4 signaling to Akt in a subset of cells (Figure A7 A, B). In the CSM, inhibiting MEK decreases ERK-mediated mTORC1 activation and releases restraint on mTORC2 to activate Akt. A simulated dose response of trametinib conditioning revealed that larger doses of trametinib increased the activation of Akt in MDA-MB-231 cells (Figure 2.7A). We experimentally confirmed the CSM predictions, demonstrating that conditioning MDA-MB-231 cells with trametinib for four hours heterogeneously potentiated CXCR4 signaling to Akt (Figure 2.7B). Difference maps illustrate areas of change of peak activation with inhibitor conditioning compared to control (Figure 2.7C). The CSM revealed that cells exhibiting enhanced Akt signaling after trametinib conditioning were those with low PI3K and mTORC1 activity, which corresponded to cells in states predisposed to be highly responsive to CXCL12 with control conditioning. By comparison, CXCR4 signaling in other, non-responsive states were not affected by trametinib (Figure 2.7C). Notably, trametinib-treated cells occupied similar regions of the signaling landscape as cells that received control conditioning, confirming that the simulated inhibitor treatment did not shift conditional signaling states and only affected responsiveness at each state.

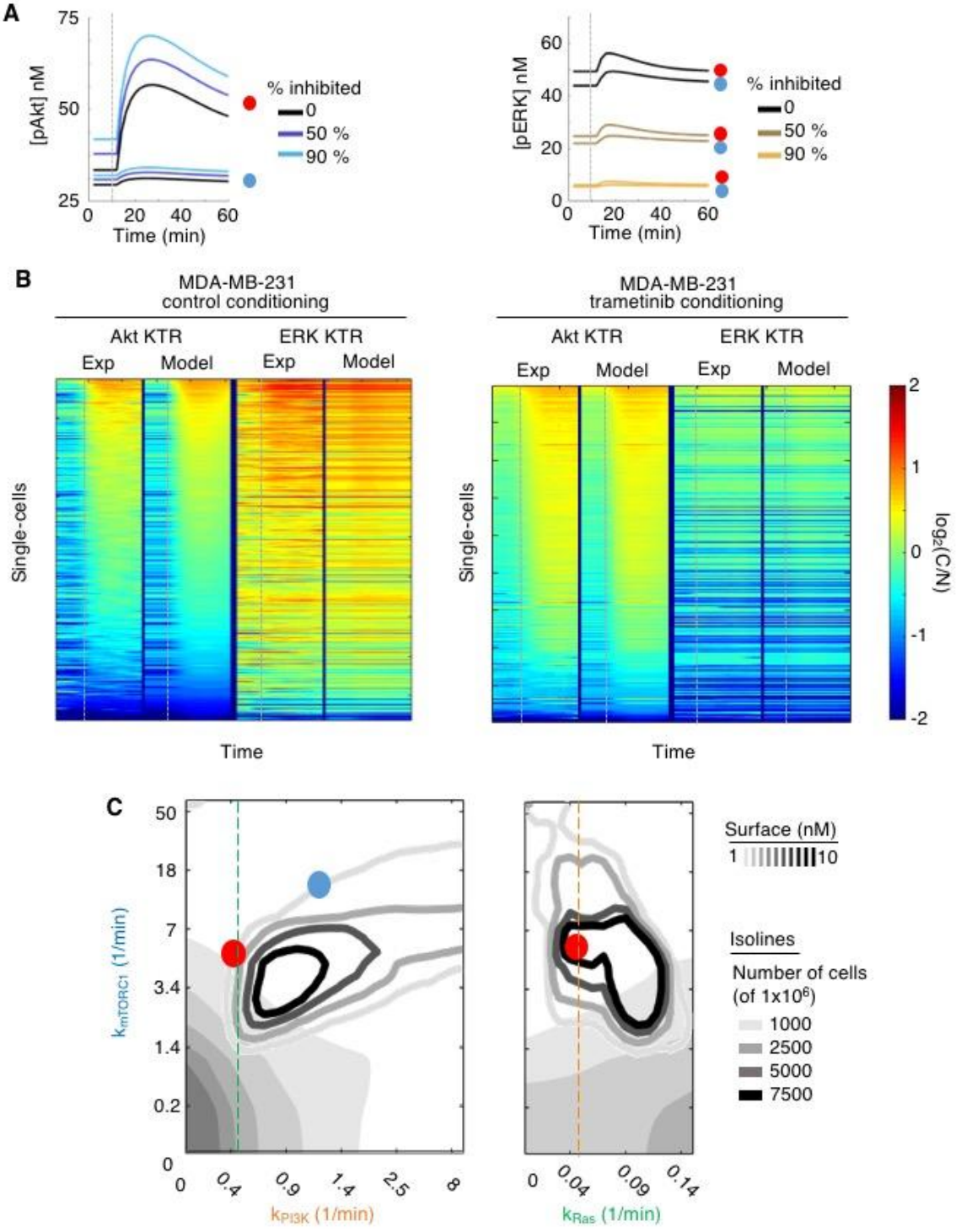
A
[pAkt] nM
75
50
25
0 20 40 60
Time (min)
% inhibited
0
50 %
90 %
[pERK] nM
60
40
20
0
0 20 40 60
Time (min)
% inhibited
0
50 %
90 %
B
MDA-MB-231
control conditioning
MDA-MB-231
trametinib conditioning
Akt KTR
ERK KTR
Exp
Model
Exp
Model
Single-cells
Time
log2(C/N)
2
1
0
-1
-2
C
50
18
7
3.4
1.4
0.2
0
0 0.4 0.9 1.4 2.5 8
kmTORC1 (1/min)
kPI3K (1/min)
0 0.04 0.09 0.14
kRas (1/min)
Surface (nM)
1
10
Isolines
Number of cells
(of 1x10^6)
1000
2500
5000
7500

Figure 2.7 Computational modeling correctly predicts that trametinib conditioning potentiates subsequent CXCR4-mediated Akt signaling in a subset of MDA-MB-231 cells.

(A) The CSM predicts Akt (left) and ERK (right) signaling dynamics at simulated concentrations of trametinib conditioning that inhibit 50% or 90% of MEK activity relative to control prior to CXCR4 stimulation. The predicted signaling dynamics denoted by the red and blue dots correspond to different conditional signaling states and correspond to the dots in C. (B) The CSM accurately predicts single-cell experimental CXCR4-mediated Akt and ERK signaling dynamics for trametinib conditioning (N=447 cells) on MDA-MB-231 cells (control conditioning, N=429 cells). Trametinib conditioning was modeled as a 50% decrease in the rate of MEK-mediated phosphorylation of ERK, consistent with noncompetitive inhibition kinetics. (C) Difference maps show the CSM-predicted change in peak Akt activation between the control conditioned and trametinib conditioned cells at each conditional signaling state. Shaded gray surface contours show regions in signaling landscape with conditional signaling states that position trametinib-conditioned cells for the listed increases in peak Akt activation (nM). Contour lines display numbers of cells out of one million occupying conditional signaling states after matching experimental trametinib-conditioned cells to the CSM. Green and orange lines illustrate the specific Ras and PI3K planes, respectively, of the CSM corresponding to the responsiveness underlays. Red dots indicate conditional signaling states that were permissive to Akt signaling under control conditioning. Blue dots indicate conditional states that were not permissive to Akt signaling under control conditioning. The red and blue dots from C correspond with those in A.

2.4.7 mTORC1 inhibition potentiates subsequent CXCR4-mediated Akt and ERK signaling

A simulated dose response of ridaforolimus conditioning potentiated CXCR4 signaling to both Akt and ERK in a dose-dependent manner MDA-MB-231 cells (Figure 2.8A, Figure A7 C). In the CSM, inhibition of mTORC1 releases restraint on both mTORC2 and Ras, thereby activating both Akt and ERK. Difference maps indicated enhanced CXCR4 signaling to Akt in cells with low PI3K activity, and all cells exhibited enhanced ERK signaling (Figure 2.8B). We experimentally confirmed CSM predictions, demonstrating that conditioning MDA-MB-231 cells for four hours with ridaforolimus potentiated CXCL12-dependent activation of both Akt and ERK (Figure A7 D). Again, the conditional signaling states of ridaforolimus-treated cells were similar to those of cells that received control conditioning. These data establish that targeted kinase inhibitors can potentiate CXCR4 signaling in subpopulations of cells.

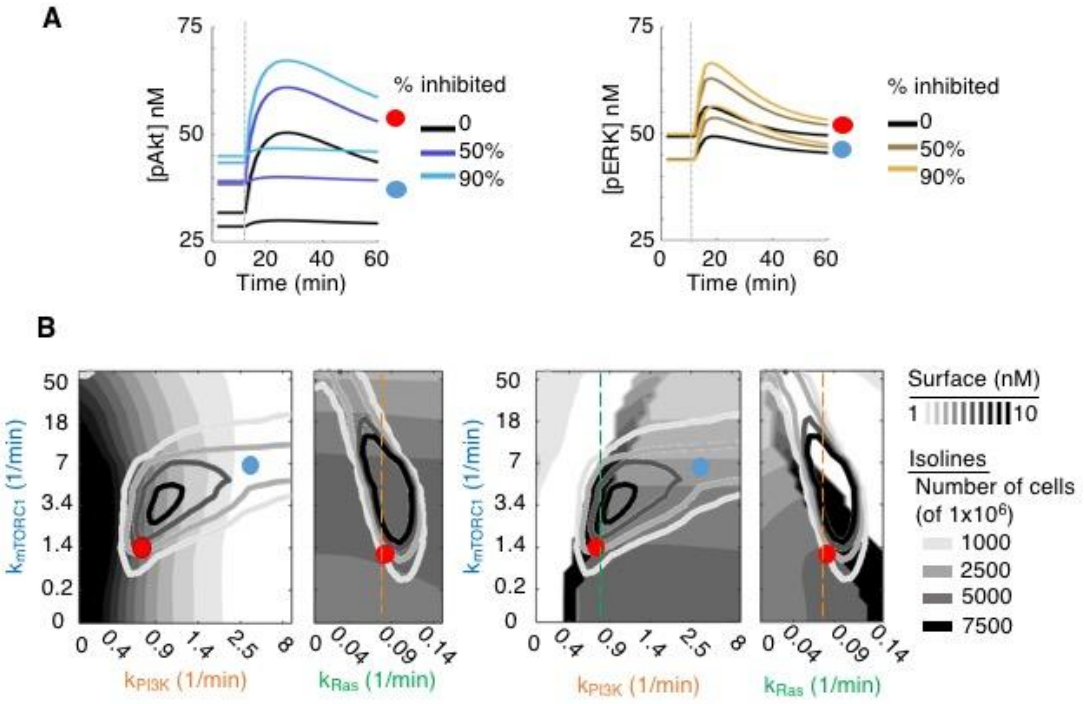

Figure 2.8 Computational modeling correctly predicts that conditioning with the mTORC1 inhibitor ridaforolimus potentiates subsequent CXCR4-mediated Akt and ERK signaling in MDA-MB-231 cells

(A) The CSM predicts Akt (left) and ERK (right) signaling dynamics at simulated concentrations of ridaforolimus conditioning that inhibit mTORC1 activity by 50% or 90% relative to control prior to CXCR4 stimulation. The predicted signaling dynamics denoted by the red and blue dots correspond to cells able to respond and not respond in Akt under control conditioning, respectively. (B) Difference maps show the CSM-predicted change in peak Akt (left) and peak ERK (right) activation between the control conditioned and ridaforolimus conditioned cells at each conditional signaling state. Shaded gray surface contours show regions in signaling landscape with conditional signaling states that position ridaforolimus-conditioned cells for the listed increases in peak activation (nM). Contour lines display numbers of cells out of one million occupying conditional signaling states after matching experimental ridaforolimus-conditioned cells to the CSM. Green and orange lines illustrate the specific Ras and PI3K planes, respectively, of the CSM corresponding to the responsiveness underlays. The red and blue dots from B correspond to those in A. The CSM-predicted signaling dynamics are from 50% inhibition of mTORC1.

2.5 Discussion

Rather than representing hard-wired pathways that always generate the same output, signaling networks in single cells produce heterogeneous responses shaped by changing environmental conditions and signaling inputs. Our work demonstrates that although cells adapt signaling based on short-term memories of prior inputs, these adaptations are predictable based on a specific set of rules. We used one parameter set to simulate single-cell paired Akt and ERK signaling dynamics for entire populations of cells and introduced heterogeneity by adding extrinsic noise to only three pathway components: PI3K, Ras, and mTORC1. The ability of the CSM to predict heterogeneous basal states and responsiveness of single cells in multiple breast cancer cell types with only extrinsic noise in three pathway components suggests that the model captures the major drivers of CXCR4 signaling to Akt and ERK.

Local intracellular and extracellular conditions tune signaling responses in individual cells. As a consequence, gradients of growth factors or kinase inhibitors in vivo may drive heterogeneous signaling outcomes. We showed that conditional effects such as genetic mutations, growth factors, and kinase inhibitors all collectively tuned responsiveness of cells to CXCL12-CXCR4 signaling and activation of Akt and ERK. We propose that cells exist on a signaling landscape based on conditional states. The signaling landscape, which accounts for CXCR4 signaling dynamics at all possible cellular conditional states, defines the output of the CSM. Genetic mutations force cells into distinct regions within the signaling landscape. Conditioning cells with growth factors allows cells to shift within these regions to potentiate signaling, whereas conditioning with kinase inhibitors modifies the cell signaling potential in each state but preferentially affects cells already existing in states poised to signal. We showed that trametinib potentiated only subsequent CXCR4-mediated Akt signaling in cells with low PI3K and mTORC1 activities, which constituted a small fraction of cells in the population. As an active enzyme, even modest increases in Akt signaling and function in small numbers of cells can drive the pathogenesis of processes critical to cancer progression (64), making behaviors of “outlier” single cells relevant for disease and therapy.

We built the CSM to explore the entire design space (the single-cell signaling landscape) potentially occupied by experimental cells. By mapping experimental cells onto the signaling landscape, we assigned mechanisms for heterogeneous CXCR4 signaling responses observed in experiments and discovered how conditioning tuned these responses. The CSM predicted that trametinib not only would produce the expected outcome of suppressing ERK, but also produce the off-target consequence of enhancing CXCR4-mediated activation of Akt. Similarly, we predicted that ridaforolimus would potentiate both Akt and ERK signaling, two pathways that promote cancer growth and metastasis. These results highlight how targeted cancer therapies may potentiate CXCR4 signaling, a driver of tumor growth and metastasis, and how our computational model can predict such outcomes.

Cell signaling networks contain central nodes that store integrated information about multiple inputs and use this information to regulate responses to new signaling inputs. Our data indicate that mTORC1 functions as one of these central nodes, holding information about prior signaling to control subsequent activation of Akt and ERK. Although negative regulation of ERK by mTORC1 remains poorly characterized in literature, our CSM and single-cell imaging experiments demonstrate this as a crucial mechanism that drives coordinate regulation of Akt and ERK.

Although robust and predictive, the computational model we present here points to additional research opportunities relevant to heterogeneity in single cell signaling. To establish heterogeneity among cells, the CSM incorporated extrinsic noise in three pathway components: PI3K, Ras, and mTORC1. However, specific molecular mechanisms driving noise in these pathway components remain to be identified. The cell cycle plays a role in cell signaling variability (19), but other environmental inputs likely also shape signaling responsiveness, such as hypoxia, pH, metabolism, energy levels, or other signaling stimuli. Mathematically, the source of the noise in our model is embedded in a first-order kinetic rate constant. Understanding the causes of extrinsic noise in these molecules will highlight potential approaches to tune CXCR4 signaling for

therapy. This work focused only on the tunability of CXCR4 signaling. Because our data suggest that signaling heterogeneity can originate downstream of receptors, we posit that other signaling pathways can be tuned by a similar mechanism. In integrated 3D environments with mixed cellular composition, we predict cells will occupy some signaling states in the CSM-predicted signaling landscape that remain unoccupied in 2D monocultures. Because the equations in the CSM unrelated to extrinsic noise describe kinetic reactions independent of cellular geometry, we expect the model will predict behaviors in mixed cell environments and complex tissues. We realize that environmental context may alter the initial conditions of some model species, such as CXCR4 abundance. Our future studies will advance into 3D environments and mouse models of cancer, where heterogeneous CXCR4 signaling responses are critical to mechanisms of metastasis and response to targeted therapies.

2.6 References

1. Yao J, Pilko A, Wollman R. Distinct cellular states determine calcium signaling response. Mol Syst Biol. 2016;12(12):894.
2. Kim E, Kim J, Smith MA, Haura EB, Alexander R, Anderson A. Cell signaling heterogeneity is modulated by both cell-intrinsic and -extrinsic mechanisms: An integrated approach to understanding targeted therapy. PLoS Biol. 2018;16(3):1–29.
3. Altschuler SJ, Wu LF. Cellular Heterogeneity: Do Differences Make a Difference? Cell. 2010;141:559–63.
4. Irish JM, Hovland R, Krutzik PO, Perez OD, Bruserud Ø, Gjertsen BT, et al. Single Cell Profiling of Potentiated Phospho-Protein Networks in Cancer Cells. Cell. 2004;118:217–28.
5. Snijder B, Pelkmans L. Origins of regulated cell-to-cell variability. Nat Rev Mol Cell Biol. 2011;12(2):119–25.
6. Hughey JJ, Lee TK, Lipniacki T, Quake SR, Covert MW. Single-cell NF-kB dynamics reveal digital activation and analogue information processing. Nature. 2010;466:267–72.
7. Gaudet S, Miller-Jensen K. Redefining signaling pathways with an expanding single-cell toolbox. Trends Biotechnol. 2016;34(6):458–69.
8. Gross SM, Rotwein P. Akt signaling dynamics in individual cells. J Cell Sci. 2015;128(14):2509–19.
9. Cojoc M, Peitzsch C, Polishchuk L, Telegeev G, Dubrovska A. Emerging targets in cancer management: role of the CXCL12/CXCR4 axis. Onco Targets Ther. 2013;6:1347–61.
10. Sobolik T, Su Y, Wells S, Ayers GD, Cook RS. CXCR4 drives the metastatic phenotype in breast cancer through induction of CXCR2 and activation of MEK and PI3K pathways. Mol Biol Cell. 2014;25.
11. Ozawa P, Ariza C, Ishibashi C, Fujita T, Banin-Hirata B, Oda J, et al. Role of CXCL12 and CXCR4 in normal cerebellar developmentand medulloblastoma. Int J Cancer. 2014;138:10–3.
12. Cavnar SP, Ray P, Moudgil P, Chang SL, Luker KE, Linderman JJ, et al. Microfluidic source-sink model reveals effects of biophysically distinct CXCL12 isoforms in breast cancer chemotaxis. Integr Biol. 2014;6(5):564–76.
13. Pernas S, Martin M, Kaufman PA, Gil-Martin M, Pardo PG, Lopez-Tarruella S, et al. Balixafortide plus eribulin in HER2-negative metastatic breast cancer: a phase 1, single-arm, dose-escalation trial. Lancet Oncol. 2018;19:812–24.
14. Sun X, Cheng G, Hao M, Zheng J, Zhou X, Zhang J, et al. CXCL12/CXCR4/CXCR7 chemokine axis and cancer progression. Cancer Metastasis Rev. 2010;29(4):709–22.
15. Domanska UM, Kruizinga RC, Nagengast WB, Timmer-Bosscha H, Huls G, De Vries EGE, et al. A review on CXCR4/CXCL12 axis in oncology: No place to hide. Eur J Cancer. 2013;49(1):219–30.
16. Hollestelle A, Elstrodt F, Nagel JHA, Kallemeijn WW. Phosphatidylinositol-3-OH Kinase or RAS Pathway Mutations in Human Breast Cancer Cell Lines. Mol Cancer Res. 2007;5(2):195–201.

17. Chen Y, Humphries B, Brien R, Gibbons AE, Chen Y, Qyli T, et al. Functional Isolation of Tumor-Initiating Cells using Microfluidic-Based Migration Identifies Phosphatidylserine Decarboxylase as a Key Regulator. Sci Rep. 2018;8(244):1–13.
18. Gilani RA, Phadke S, Bao LW, Lachacz EJ, Dziubinski ML, Brandvold KR, et al. UM-164: a potent c-Src/p38 kinase inhibitor with in vivo activity against triple negative breast cancer. Clin Cancer Res. 2016;
19. Maryu G, Matsuda M, Aoki K. Multiplexed Fluorescence Imaging of ERK and Akt Activities and Cell-cycle Progression. Cell Struct Funct. 2016;41:81–92.
20. Vincent P, Merola F, Bousmah Y. Minimum set of mutations needed to optimize cyan fluorescent proteins for live cell imaging. Mol Biosyst. 2013;9:258–67.
21. Griesbeck O, Baird GS, Campbell RE, Zacharias DA, Tsien RY. Reducing the Environmental Sensitivity of Yellow Fluorescent. J Biol Chem. 2001;276(31):29188–94.
22. Chang SL, Cavnar SP, Takayama S, Luker GD, Linderman JJ. Cell, Isoform, and Environment Factors Shape Gradients and Modulate Chemotaxis. PLoS One. 2015;10(4):e0123450.
23. Coggins NL, Trakimas D, Chang SL, Ehrlich A, Ray P, Luker KE, et al. CXCR7 Controls Competition for Recruitment of β-Arrestin 2 in Cells Expressing Both CXCR4 and CXCR7. PLoS One. 2014;9(6):e98328.
24. Spinosa PC, Luker KE, Luker GD, Linderman JJ. The CXCL12/CXCR7 signaling axis, isoforms, circadian rhythms, and tumor cellular composition dictate gradients in tissue. PLoS One. 2017;12(11).
25. Smith JS, Rajagopal S. The β-Arrestins: Multifunctional regulators of G protein-coupled receptors. J Biol Chem. 2016;291(17):8969–77.
26. DeWire SM, Ahn S, Lefkowitz RJ, Shenoy SK. β-Arrestins and Cell Signaling. Annu Rev Physiol. 2007;69(1):483–510.
27. Manning B, Cantley L. AKT/PKB Signalling: Navigating the Network. Cell. 2017;169:1261–74.
28. Song G, Ouyang G, Bao S. The activation of Akt/PKB signaling pathway and cell survival. J Cell Mol Med. 2005;9(1):59–71.
29. Alessi DR, Andjelkovic M, Caudwell B, Cron P, Morrice N, Cohen P, et al. Mechanism of activation of protein kinase B by insulin and IGF-1. EMBO J. 1996;15(23):6541–51.
30. Lamb TD. Stochastic simulation of activation in the G-protein cascade of phototransduction. Biophys J. 1994;67(4):1439–54.
31. Hatakeyama M, Kimura S, Naka T, Kawasaki T, Yumoto N, Ichikawa M, et al. A computational model on the modulation of mitogen-activated protein kinase (MAPK) and Akt pathways in heregulin-induced ErbB signalling. Biochem J. 2003;373(2):451–63.
32. Jain P, Bhalla US. Signaling logic of activity-triggered dendritic protein synthesis: An mTOR gate but not a feedback switch. PLoS Comput Biol. 2009;5(2).
33. Pezze PD, Ruf S, Sonntag AG, Langelaar-Makkinje M, Hall P, Heberle AM, et al. A systems study reveals concurrent activation of AMPK and mTOR by amino acids. Nat Commun. 2016;7:1–19.
34. Mendoza M, Emrah Er E, Blenis J. The Ras-ERK and PI3K-mTOR Pathways:

Cross-talk and Compensation. Trends Biochem Sci. 2011;36(6):320–8.
35. Yang G, Murashige DS, Humphrey SJ, James DE. A Positive Feedback Loop between Akt and mTORC2 via SIN1 Phosphorylation. Cell Rep. 2015;12(6):937–43.
36. Gan X, Wang J, Su B, Wu D. Evidence for direct activation of mTORC2 kinase activity by phosphatidylinositol 3,4,5-trisphosphate. J Biol Chem. 2011;286(13):10998–1002.
37. Julien L-A, Carriere A, Moreau J, Roux PP. mTORC1-Activated S6K1 Phosphorylates Rictor on Threonine 1135 and Regulates mTORC2 Signaling. Mol Cell Biol. 2010;30(4):908–21.
38. Yoon M-S. The Role of Mammalian Target of Rapamycin (mTOR) in Insulin Signaling. Nutrients. 2017;9(11):1176.
39. Yoneyama Y, Inamitsu T, Chida K, Iemura S-I, Natsume T, Tatsuya M, et al. Serine phosphorylation by mTORC1 promotes IRS-1 degradation through SCF β-TRCP E3 ubiquitin ligase. iScience. 2018;5:20487.
40. Liu P, Gan W, Inuzuka H, Lazorchak AS, Gao D, Arojo O, et al. Sin1 phosphorylation impairs mTORC2 complex integrity and inhibits downstream Akt signalling to suppress tumorigenesis. Nat Cell Biol. 2013;15(11):1340–50.
41. Liu P, Guo J, Gan W, Wei W. Dual phosphorylation of Sin1 at T86 and T398 negatively regulates mTORC2 complex integrity and activity. Protein Cell. 2014;5(3):171–7.
42. Ebner M, Sinkovics B, Szczygieł M, Ribeiro DW, Yudushkin I. Localization of mTORC2 activity inside cells. J Cell Biol. 2017;216(2):343–53.
43. Saxton RA, Sabatini DM. mTOR Signaling in Growth, Metabolism, and Disease. Cell. 2017;168(6):960–76.
44. Sulaimanov N, Klose M, Busch H BM. Understanding the mTOR signaling pathway via mathematical modeling. WIREs Syst Biol Med. 2017;9.
45. Pezze PD, Sonntag AG, Thien A, Prentzell MT. A dynamic network model of mTOR signalling reveals TSC independent mTORC2 regulation. Sci Signal. 2012;5(217):1–18.
46. Rocca GJ Della, Biesen T Van, Daaka Y, Luttrell DK, Luttrell LM, Lefkowitz RJ. Ras-dependent Mitogen-activated Protein Kinase Activation by G Protein-coupled Receptors. J Biol Chem. 1997;272(31):19125–32.
47. Posada IMD, Lectez B, Siddiqui FA, Oetken-Lindholm C, Sharma M, Abankwa D. Opposite feedback from mTORC1 to H-ras and K-ras4B downstream of SREBP1. Sci Rep. 2017;7(1):1–14.
48. Karoulia Z, Gavathiotis E, Poulikakos PI. New perspectives for targeting RAF kinase in human cancer. Nat Rev Cancer. 2017;17(11):676–91.
49. Moelling K, Schad K, Bosse M, Zimmermann S, Schweneker M. Regulation of Raf-Akt cross-talk. J Biol Chem. 2002;277(34):31099–106.
50. Zhang W, Liu HT. MAPK signal pathways in the regulation of cell proliferation in mammalian cells. Cell Res. 2002;12(1):9–18.
51. Regot S, Hughey JJ, Bajar BT, Carrasco S, Covert MW. High-sensitivity measurements of multiple kinase activities in live single cells. Cell. 2014;157(7):1724–34.
52. Yuan TL, Wulf G, Burga L, Cantley LC. Cell-to-cell variability in PI3K protein level

regulates PI3K-AKT pathway activity in cell populations. Curr Biol. 2011;21(3):173–83.
53. Cintas C, Guillermet-Guibert J. Heterogeneity of Phosphatidylinositol-3-Kinase (PI3K)/AKT/Mammalian Target of Rapamycin Activation in Cancer: Is PI3K Isoform Specificity Important? Front Oncol. 2018;7.
54. Martínez-Revollar G, Garay E, Martin-Tapia D, Nava P, Huerta M, Lopez-Bayghen E, et al. Heterogeneity between triple negative breast cancer cells due to differential activation of Wnt and PI3K/AKT pathways. Exp Cell Res. 2015;339(1):67–80.
55. Marino S, Hogue IB, Ray CJ, Kirschner DE. A Methodology for Performing Global Uncertainty and Sensitivity Analysis in Systems Biology. Vol. 254, Journal of Theoretical Biology. 2009. 178–196 p.
56. Kudo T, Jeknic S, Macklin DN, Akhter S, Hughey JJ, Regot S, et al. Live-cell measurements of kinase activity in single cells using translocation reporters. Nat Protoc. 2017;13(1):155–69.
57. Mitra T, Menon SN, Sinha S. Emergent memory in cell signaling: Persistent adaptive dynamics in cascades can arise from the diversity of relaxation time-scales. Sci Rep. 2018;8(13230):1–21.
58. Luker KE, Mihalko LA, Schmidt BT, Lewin SA, Ray P, Shcherbo D, et al. In Vivo Imaging of Ligand Receptor Binding with Gaussia Luciferase Complementation. Nat Med. 2012;18(1):172–7.
59. Kaschek D, Hahn B, Wrangborg D, Karlsson J, Kvarnström M. Heterogeneous kinetics of AKT signaling in individual cells are accounted for by variable protein concentration. Front Physiol. 2012;3(45):1–14.
60. Iwamoto K, Shindo Y, Takahashi K. Modeling Cellular Noise Underlying Heterogeneous Cell Responses in the Epidermal Growth Factor Signaling Pathway. PLoS Comput Biol. 2016;12(11):1–18.
61. Sumit M, Jovic A, Neubig RR, Takayama S, Linderman JJ. A Two-Pulse Cellular Stimulation Test Elucidates Variability and Mechanisms in Signaling Pathways. Biophys J. 2019;116:962–73.
62. Jeantet M, Tougeron D, Tachon G, Cortes U, Archambaut C, Fromont G, et al. High intra-and inter-tumoral heterogeneity of RAS mutations in colorectal cancer. Int J Mol Sci. 2016;17(12).
63. Millis S, Ikeda S, Reddy S, Gatalica Z, Kurzrock R. Landscape of Phosphatidylinositol-3-Kinase Pathway Alterations Across 19 784 Diverse Solid Tumors. JAMA Oncol. 2016;2(12):1565–73.
64. Adlung L, Kar S, Wagner M, She B, Chakraborty S, Bao J, et al. Protein abundance of AKT and ERK pathway components governs cell type- specific regulation of proliferation. Mol Syst Biol. 2017;13(1):904.

Chapter 3 Pre-existing Cellular States Control Both Epidermal Growth Factor Receptor (EGFR) and CXCR4 Signaling Heterogeneity

3.1 Abstract

Single cells within a population exhibit marked heterogeneity in signaling outcomes when stimulated identically. Previous work by our group uncovered that signaling heterogeneity following binding to the chemokine receptor CXCR4, a receptor critical in normal development and cancer progression, can be mechanistically explained by variable pre-existing intracellular states set by extrinsic noise. These pre-existing cell states vary from cell-to-cell, but CXCR4 signaling to downstream effectors ERK and Akt is deterministic given the cell state. However, a robust test of this hypothesis was lacking because we had only explored CXCR4 signaling. Here we show that given the pre-existing cell state, signaling through both CXCR4 and epidermal growth factor receptor (EGFR), a receptor tyrosine kinase implicated in cancer cell growth and proliferation, are predictable at the single-cell scale. Computational modeling of EGFR and CXCR4 signaling through ERK and Akt, coupled with time-lapse, dynamic, live cell imaging, predicts that the same set of pre-existing cell states explain signaling heterogeneity through both EGFR and CXCR4 at multiple doses of ligand and in two breast cancer cell lines. We also predict how phosphatidylinositol-3-kinase (PI3K) targeted therapies potentiate ERK signaling in certain breast cancer cells, establishing clinical utility of the computational model. Our data demonstrate that a conserved signaling motif exists for the EGFR and CXCR4 signaling systems with implications for more efficient strategies of therapeutic intervention.

3.2 Introduction

The signaling responses of individual cells to identical stimuli are often heterogeneous (1,2). Following ligand-receptor binding, cells can activate downstream effectors along a continuum from no to high activation. The fact that extracellular ligand binding may not activate downstream effectors highlights how genetic variability observed by analysis of biomarkers is not the sole driver of heterogeneity *in vivo*. The diversity of cell signaling responses within a population can promote progression of diseases such as cancer, in which signaling inputs to subpopulations of cells, such as metastatic cells, dictate patient outcome. While signaling heterogeneity is starting to be recognized even in the most homogeneous cellular conditions (3–7), a mechanism explaining the source of this heterogeneity, especially one consistent with multiple receptor-ligand systems, has yet to be proposed. Understanding the major drivers of cell signaling heterogeneity will inform new treatment strategies to target subpopulations of cells promoting cancer progression.

Recently, we developed the computational conditional signaling model (CSM) that provides a framework for understanding cell signaling heterogeneity following signaling through chemokine receptor CXCR4 (6), a G-protein coupled receptor which binds chemokine CXCL12 and has been identified as a critical target for cancer therapy (8–12). We demonstrated that cell signaling heterogeneity to downstream effectors ERK and Akt, two kinases implicated in cancer cell survival, proliferation, and metastasis (13,14), can be mechanistically explained by variability in pre-existing cell states (6). We postulate that these same pre-existing cell states, characterized by identical intracellular signaling parameter sets, can also describe signaling heterogeneity through epidermal growth factor receptor (EGFR), a receptor tyrosine kinase which binds epidermal growth factor (EGF) and is a target for cancer therapies due to the receptor's role in enhanced and uncontrolled cell proliferation (15–17). Additionally, evidence suggests that EGFR binding can enhance CXCR4-mediated chemotaxis of cancer cells, emphasizing the importance for understanding how heterogeneity in both of these pathways governs downstream signaling (18). By providing a framework for cell signaling heterogeneity

through two receptors from distinct receptor families, we gain insight into conserved signaling motifs and can predict signaling in the presence of targeted therapies.

In this work, we expand our existing computational model to test the hypothesis that pre-existing cell states control heterogeneous downstream signaling through both EGFR and CXCR4. We combined kinase translocation reporters (KTRs) (19,20) with two-photon dynamic live cell microscopy to calibrate the model and confirm model predictions. We used two breast cancer cell lines of different mutational backgrounds and various doses of both EGF and CXCL12 to test model robustness in various conditions. The model predicts how targeted therapeutics against Akt signaling can have inadvertent consequences on ERK signaling, highlighting the importance of understanding crosstalk and feedback through these pathways. Our data identify a conserved motif among EGFR and CXCR4 signaling that gives rise to heterogeneous outcomes with implications for the design of more strategic therapeutic interventions.

3.3 Methods

3.3.1 Cell culture

Cell culture for both SUM 159 and MDA-MB-231 breast cancer cells was exactly as described in Chapter 2 (6).

3.3.2 Fluorescent reporter construction

We used fluorescent reporters (KTRs) first proposed by Regot et. al (19,20) and implemented exactly as described in Chapter 2 (6).

3.3.3 Cell engineering

Cell engineering was done exactly as described in Chapter 2 (6).

3.3.4 Time-lapse two photon microscopy and image processing

Time-lapse microscopy for SUM 159 and MDA-MB-231 breast cancer cells was exactly as reported in Chapter 2 (6).

3.3.5 Computational model mechanisms

We expanded upon our computational model of heterogeneous CXCR4-mediated Akt and ERK signaling from Chapter 2 (6) by incorporating EGFR dynamics to the receptor module. The complete model includes three modules which describe the dynamics of receptors, signaling, and reporters. All equations, parameters, and initial conditions can be found in Appendix Tables B1-B5.

Receptor dynamics for CXCR4 are as described previously (21–23). We adapted a simple mechanism of EGFR binding, internalization, and degradation from literature data (24). While many models of EGFR dynamics which incorporate mechanisms such as receptor dimerization, trafficking to endosomes, and lipid rafts exist in literature (24–28), we constructed a simple model consistent with the overall behavior of EGFR signaling seen in our imaging experiments. Surface EGFR binds EGF in the extracellular space to form an EGF-EGFR complex which can be internalized and degraded by first order kinetics (24). We note that receptor tyrosine kinases like EGFR typically dimerize upon binding EGF (29), but we lump dimerization with the binding event for simplicity. Unbound EGFR internalizes and recycles according to first order kinetics (24).

Signaling dynamics in the computational model are taken from our previous work (6) with minor modifications. The signaling module describes how ligand-induced receptor activation promotes downstream ERK and Akt signaling in single cancer cells. Briefly, liganded receptor complexes (CXCL12-CXCR4 or EGF-EGFR) activate downstream signaling cascades through the ERK and Akt pathways. Since EGFR is a receptor tyrosine kinase, the EGF-EGFR complex signals directly to Ras and PI3K, whereas CXCR4 is a G-protein coupled receptor and signals to G-proteins. The ERK and Akt signaling cascades, which include the activation and deactivation of important signaling

molecules downstream of these receptors, are modeled by first order or Michaelis-Menten enzyme kinetics. In this version of the model, we modified the mechanism describing mTOR activation to simulate how mTOR is sequestered into either mTORC1 or mTORC2. mTOR in our model represents the inactive form of both mTORC1 and mTORC2, but also includes mTOR in complex species unaccounted for in our model, such as mTORC3 (30). This mTOR mechanism is supported by literature citing how rapamycin, a compound which strongly inhibits mTORC1, also inhibits mTORC2 at high drug concentrations, implying the existence of shared mTOR between the two complexes (31,32). All other kinase signaling kinetics are exactly as previously described (6).

Activated ERK and activated Akt promote the phosphorylation and translocation of the kinase translocation reporters for each kinase. We used a set of previously published ordinary differential equations (19) to describe the mechanism by which these processes occur, and these dynamics are incorporated as previously described (6). The model accounts for reporter concentrations of each kinase, ERK and Akt. The reporter can exist in the phosphorylated or unphosphorylated state in both the cytoplasm and the nucleus. The single-cell kinase activity is measured as the $\log_2$(C/N), where C represents the sum of unphosphorylated and phosphorylated cytoplasmic reporter and N represents the sum of unphosphorylated and phosphorylated nuclear reporter. We use the $\log_2$(C/N) for both ERK and Akt to compare our model predictions with experimental observations of single-cells.

3.3.6 Computational model solution

The solution to the computational model is generated using MATLAB function *ode15s*. Given the parameters, initial conditions, and rate equations described in Appendix Tables B1-B5, we run the model to steady-state concentrations of all model species in the absence of ligand stimulus. These steady-state concentrations are then used as the initial conditions for simulations of ligand-induced (EGF or CXCL12) activation of downstream ERK and Akt signaling, which occur according to the ordinary differential equations above.

3.3.7 Computational model calibration

The goal of our calibration process was to find a baseline parameter set which best fits the most common ERK and Akt responses in our KTR imaging experiment using SUM 159 cells. We can then use this baseline parameter set to account for heterogeneity using extrinsic noise, and account for another cell type (MDA-MB-231 cells) by adding a mutation parameter. The mode cell in our experiments was determined by pairing the ERK and Akt responses in single cells and performing a least-square error calculation of all single cell responses with each other. By assigning a maximum error cutoff between the given cell and all other cells in the experiment, we can tally the number of other cells in the experiment which have errors smaller than this maximum. The mode cell will be the cell with the highest tally, indicating that its paired ERK and Akt responses were similar to the most other cells.

The parameters we calibrated to find the baseline parameter set specific for the mode cell in this work were those that we have added or adjusted since the previous version of the model. These new parameters fall into one of three categories: they were directly involved in (i) mTORC1 and mTORC2 activation, (ii) mTORC1-mediated restraint, or (iii) EGFR binding and trafficking dynamics. We calibrated the category i and ii parameters to experimental KTR imaging data of SUM 159 cells stimulated with 10 ng/mL CXCL12 (Figure 3.1B), and the category iii parameters to SUM 159 cells stimulated with 1 ng/mL EGF (Figure 3.1A).

To calibrate the category i and ii parameters, which describe intracellular downstream signaling processes involving mTOR complexes, we used Latin Hypercube Sampling (LHS) as a search strategy for efficient sampling of these new parameters with +/- 50% variation from literature estimates of baseline values (33,34). We next simulated these parameter sets in our computational model, calculated the least-square difference between the experimental single-cell ERK and Akt responses of the mode cell and each predicted ERK and Akt response from the model, and chose the parameter set with the smallest error as our baseline parameter set. In the baseline parameter set, we used

the extrinsic noise parameters that described the pre-existing state of the mode SUM 159 cell from our previous work (6). All other model parameter values for the baseline parameter set were taken from our previous work (6).

To calibrate the category iii parameters, which describe EGFR dynamics, we start with the baseline parameter set from above, which defines all downstream signaling parameters. We perform a second LHS search with +/- 50% variation from literature estimates of the category iii parameters. These parameter sets are then simulated in the computational model, and the set which best fits the mode cell from the experiment is the new baseline parameter set, containing all calibrated parameters which describe the behavior of the mode ERK and Akt response in the SUM 159 cell population.

3.3.8 Various cell types in the computational model

To model MDA-MB-231 cells, we use the same parameter set as the SUM 159 cells but add in a parameter for constitutive activation of B-Raf, consistent with the known mutation in these cells (35). Additionally, we decrease k_f and increase K_D of EGF binding to EGFR for MDA-MB-231 cells as we noticed this binding interaction was weaker in MDA-MB-231 cells. The apparent binding interaction being weaker in MDA-MB-231 cells is likely due to a smaller number of high-affinity EGFR compared to SUM 159 cells. This could arise from different configurations of lipid rafts or HER2 expression, features not explicitly incorporated into our computational model (36).

3.3.9 Computational model: extrinsic noise

We incorporated signaling heterogeneity in cell populations with extrinsic noise on the single-cell scale. The same method was used as previously reported (6).

3.3.10 Determining the pre-existing state of cells in KTR experiments

We determined the pre-existing state of cells from KTR experiments by comparing single-cell ERK and Akt responses between the experiments and computational model. The computational model generates over 12,000 possible ERK and Akt responses to

any dose of either EGF or CXCL12. We calculated the residuals of the ERK and Akt responses from the experiment to all possible predicted responses from the corresponding ligand type and dose from the model. For a given experimental cell, the predicted pre-existing state which corresponds to the model responses with the minimum residual is classified as the pre-existing state of the given experimental cell. In this manner, each experimental cell is coupled to a set of extrinsic noise rate parameters which define the pre-existing cell state. Occupancy maps shown in Figures 3.4D, 3.7C and Figures B1 B, B3 C illustrate the probability density of experimental cells in pre-existing states from the computational model. To calculate the probability density, we calculate a fit score denoted as the reciprocal of the sum of the squared residuals for experimental ERK and Akt KTRs compared with the simulated ERK and Akt KTR at each of the over 12,000 pre-existing states in the model. We normalize the fit score for each experimental cell to the sum over the fit score to all model pre-existing states. Using a lower bound (0.0005), below which fit scores are set to 0, we calculate the probability of occupancy at each pre-existing cell state. These probabilities are ranked and summed to determine the probability density of experimental cells in pre-existing states, shown as projections onto two axes in the contour plots.

3.4 Results

3.4.1 EGFR and CXCR4 signaling responses to ERK and Akt are heterogeneous

EGFR and CXCR4 elicit both Akt and ERK signaling upon EGF and CXCL12 binding, respectively (17,37). To capture EGFR and CXCR4 signaling to ERK and Akt in single cells, we use cell constructs reported in Spinosa et. al (6). Briefly, we stably expressed fluorescent reporters for activities of these kinases (kinase translocation reporters, KTRs) in two breast cancer cell lines, SUM 159 and MDA-MB-231 cells. KTRs reversibly undergo a nucleocytoplasmic shuttling event based on the phosphorylation for specific substrates of each kinase. The cytoplasmic to nuclear ratio of fluorescence intensity of the KTRs in single cells is a measure of kinase activity (19,20). Both cell

lines stably express histone 2B fused to mCherry (H2B-mCherry) to mark the nucleus for image analysis purposes.

Using live-cell imaging to quantify ERK and Akt KTR dynamics in individual cells, we observed heterogeneous EGFR and CXCR4 signaling in SUM 159 breast cancer cells stimulated with 1 ng/mL EGF (Figure 3.1A) or 10 ng/mL CXCL12 (Figure 3.1B) after a fetal bovine serum (FBS) starve from normal culture conditions. ERK activation was more pronounced compared to Akt activation due to the constitutively active phosphatidylinositol-3-kinase (PI3K) in these cells. Under either EGF or CXCL12 stimulation, cells respond along a continuum from no to high activation, consistent with previously reported heterogeneous responses (6).

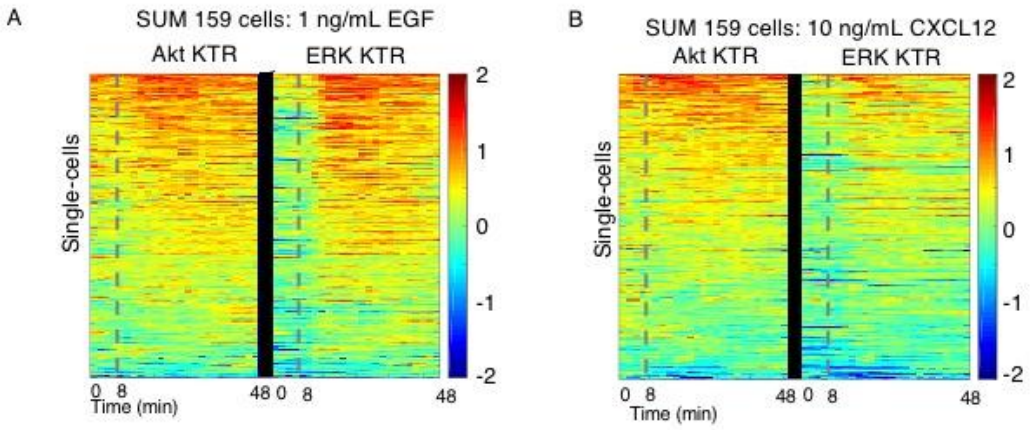

Figure 3.1 EGF signaling is heterogeneous in single cells

(A) Time tracks of Akt (left) and ERK (right) signaling in single SUM 159 cells. Left of the gray dotted line represents the basal signaling state of the cells prior to ligand stimulation. The gray dotted lines indicate when (A) EGF or (B) CXCL12 was added, and the cells were imaged for 40 minutes post-stimulation. The color indicates the log2(C/N) of the Akt and ERK KTRs at each image.

3.4.2 Computational model describes heterogeneous EGFR and CXCR4 signaling to ERK and Akt

Although different classes of receptors, both EGFR and CXCR4 signal to ERK and Akt. We hypothesized that because the range of heterogeneous EGFR signaling behaviors we observed in Figure 3.1 was similar to that previously observed with CXCR4 signaling (6), our existing computational model could be expanded to include EGFR signaling. The computational model is founded on the premise that the pre-existing cell state deterministically controls ERK and Akt responsiveness. In this model, ligand-receptor binding of either EGF-EGFR or CXCL12-CXCR4 is transduced to the single cell pre-existing state, which varies from cell-to-cell, but the resulting ERK and Akt activity is deterministic from each respective state (Figure 3.2). The pre-existing cell state is characterized by a set of intracellular downstream signaling parameters in the model that we hold identical for EGFR and CXCR4 signaling in single cells.

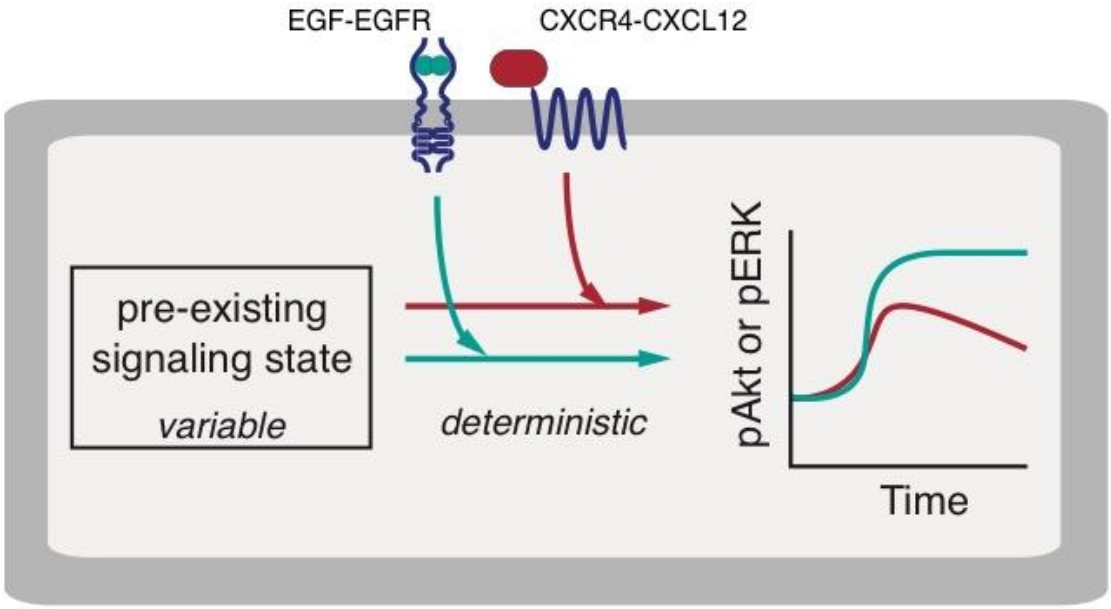

Figure 3.2 The pre-existing cell state hypothesis encompasses signaling through both EGFR and CXCR4

We hypothesize that receptor-ligand stimulation from both EGF-EGFR and CXCL12-CXCR4 interactions signals to a pre-existing state in cells. These pre-existing states are variable from cell-to-cell, but promote a deterministic output in Akt or ERK signaling, thereby generating heterogeneous responses in single cells within a population.

To test the hypothesis that variable pre-existing cell states control heterogeneity of ERK and Akt responses, we first expanded the CSM of CXCR4 signaling to include EGFR binding and intracellular trafficking dynamics (Figure 3.3A). Both the EGF-EGFR and CXCL12-CXCR4 complexes elicit downstream ERK and Akt activation through a series of crosstalk and feedback mechanisms which include mTOR dynamics (Figure 3.3B). mTORC1 acts as a major regulator of signaling as it inhibits upstream activators of the ERK and Akt pathways (38,39). Heterogeneity is incorporated in the model by adding extrinsic noise rate parameters on three key species: PI3K, Ras, and mTORC1 (3,4,6,40–43). The extrinsic noise rate parameters account for variable intracellular protein concentrations from cell to cell and define the pre-existing cell state. Mathematically, the extrinsic noise is a first-order rate parameter which activates PI3K, Ras, or mTORC1 in the absence of EGF or CXCL12. This computational model allows us to test the hypothesis that variable pre-existing states can explain signaling behaviors through both EGFR and CXCR4.

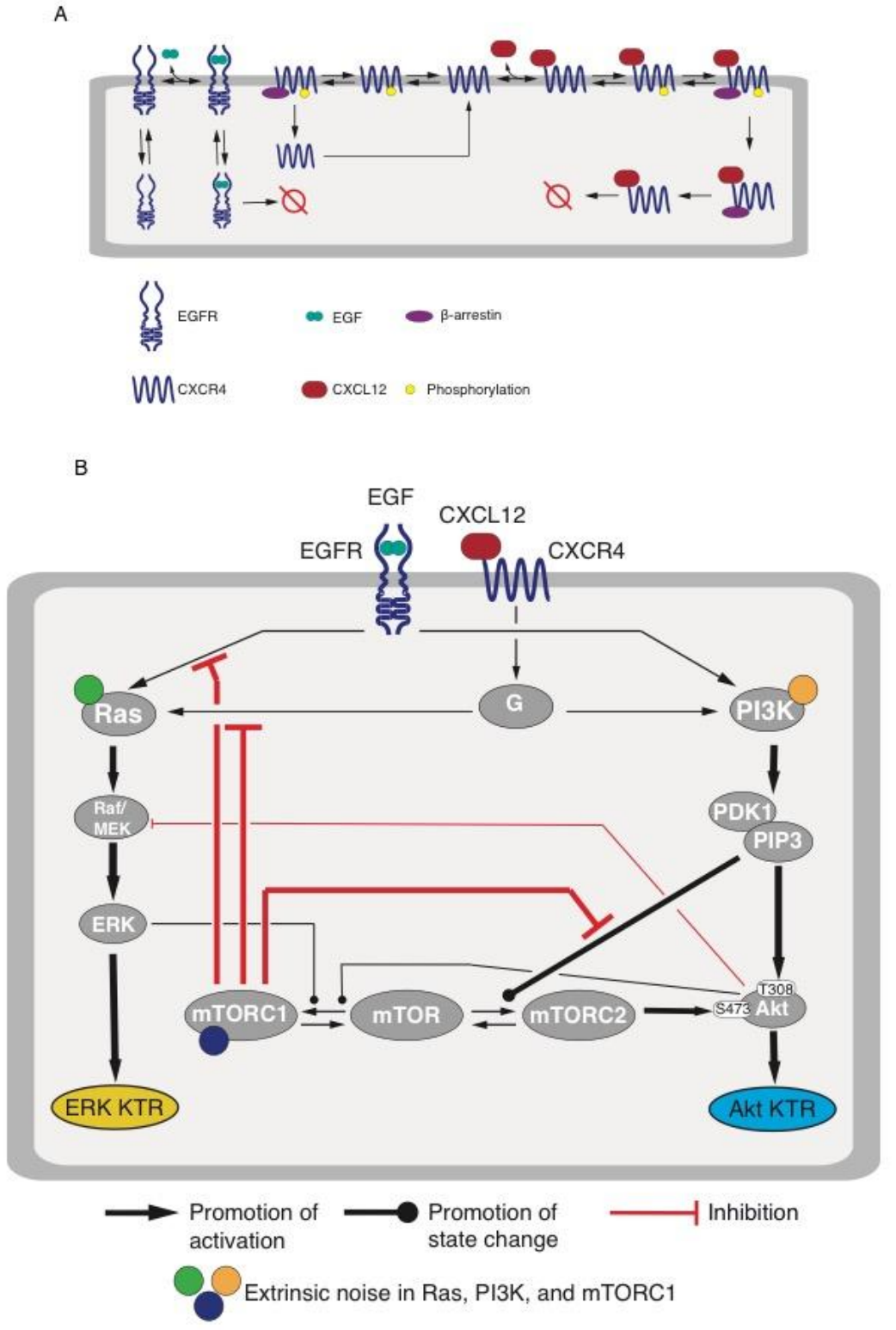
A
EGFR
EGF
β-arrestin
CXCR4
CXCL12
Phosphorylation
B
EGF
CXCL12
EGFR
CXCR4
Ras
G
PI3K
Raf/
MEK
PDK1
PIP3
ERK
T308
S473
Akt
mTORC1
mTOR
mTORC2
ERK KTR
Akt KTR
Promotion of
activation
Promotion of
state change
Inhibition
Extrinsic noise in Ras, PI3K, and mTORC1

Figure 3.3 Computational modeling combines receptor-ligand interactions with kinase signaling to downstream effectors

(A) CXCR4 and EGFR trafficking are described by ordinary differential equations detailed in Appendix Tables B1-B5. (B) The computational model is constructed according to known mechanisms of EGFR and CXCR4 signaling. Extrinsic noise in three pathway components, PI3K, Ras, and mTORC1, sets heterogeneous pre-existing states and confers distinct Akt and ERK responses in single cells. A full description of the differential equations, parameters, and initial conditions can be found in Supplementary Information.

3.4.3 The same set of pre-existing cell states explains heterogeneous EGFR- and CXCR4-mediated signaling

We next compared model predictions to the experimental data to determine whether a common set of pre-existing cell states can account for heterogeneity in EGFR and CXCR4 signaling. It must necessarily be true that the pre-existing state of cell populations under the same experimental conditions is independent of the ligand and dose used to stimulate the cells during subsequent dynamic analysis. Additionally, different cancer cell types will have different pre-existing states due to varying mutational backgrounds. We ran the computational model at various PI3K, Ras, and mTORC1 extrinsic noise states (pre-existing states) to generate a library of over 12,000 predicted EGFR- or CXCR4-mediated ERK and Akt responses (Figure 3.4A). To determine the pre-existing state of cells in any KTR imaging experiment, we perform a least-square matching process between the paired ERK and Akt responses from every single cell from an imaging experiment to all possible predicted ERK and Akt responses output from the computational model for a given ligand type (EGF or CXCL12) and dose. The predicted single-cell response that most closely matches a given experimental single-cell response retains the pre-existing state information, and we can assign this state to the given experimental cell.

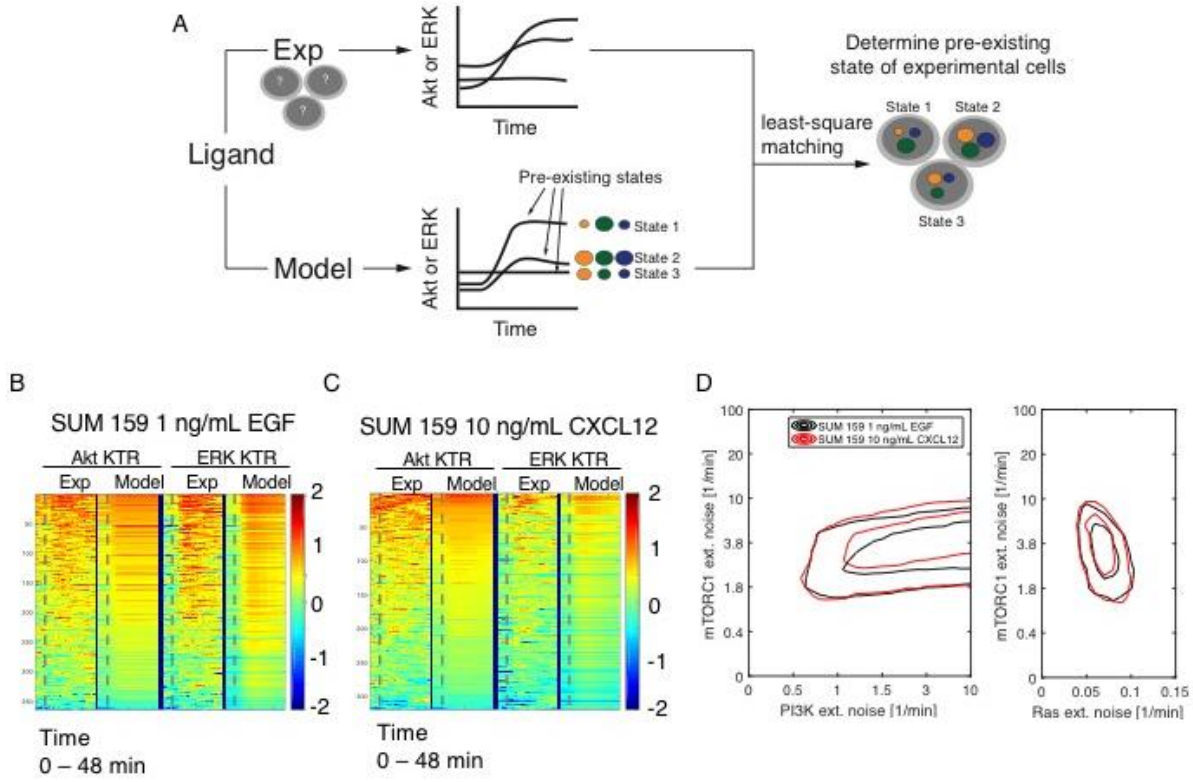

Figure 3.4 The computational model combined with KTR imaging experiments allows for the determination of the pre-existing states of single cells

(A) We combine ERK and Akt responses from imaging experiments with computational modeling to calculate the pre-existing state of each individual experimental cell. Using the model, we generate a library of possible ERK and Akt responses by varying only the extrinsic noise parameters. We perform least-square matching to determine which predicted model dynamics most closely match the ERK and Akt dynamics observed experimentally in single cells. The pre-existing state, defined as the combination of the PI3K, Ras, and mTORC1 extrinsic noise parameters, can then be back calculated from the model curve which best fit each experimental cell. (B) Akt and ERK experimental and model-predicted time tracks in single SUM 159 cells after (B) 1 ng/mL EGF and (C) 10 ng/mL CXCL12 stimulation. The color indicates the $\log_2$(C/N) of the Akt and ERK KTRs. (D) Pre-existing state occupancy maps illustrate 2D projections of the extrinsic noise states that the experimental cells occupied after least-square matching from (B) and (C). Red and black lines correspond to the 10 ng/mL CXCL12 and 1 ng/mL EGF experiments, respectively. The outer lines represent the contour holding 90% of the experimental cells, and the inner lines represent 50%.

The computational model captures the entire range of paired Akt and ERK responses of SUM 159 cells stimulated with 1 ng/mL EGF and 10 ng/mL CXCL12 (experiments presented in Figure 3.1A,B) (Figure 3.4B,C). Crucially, our model predicts that the pre-

existing states of the population of SUM 159 cells in both of these experiments are virtually the same, with high population at high PI3K activity, consistent with constitutively active PI3K in these cells, and moderate Ras and mTORC1 activity (Figure 3.4D). A similar process was performed to determine the pre-existing state of MDA-MB-231 cells. These cells have high Akt responsiveness rather than ERK due to activating mutations in K-Ras and B-Raf (35), which are upstream of ERK. Paired Akt and ERK responses from the model library match MDA-MB-231 cells from the 100 ng/mL EGF stimulation experiment, and these cells occupy a regime of moderate PI3K, Ras, and mTORC1 activity (Figure B1 A,B). Because the model predicts the same set of pre-existing cell states in two different SUM 159 cell experiments, we gain confidence in the hypothesis that the pre-existing state deterministically controls ERK and Akt signaling.

3.4.4 The pre-existing cell state controls ERK and Akt responsiveness

The computational model demonstrates that responsiveness of ERK and Akt are a function of the cellular pre-existing state. For SUM 159 cells stimulated with 1 ng/mL EGF, the highest ERK responses were seen at pre-existing states of high PI3K and low mTORC1 activity (Figure 3.5A). We also ran our computational model for MDA-MB-231 cells, which as mentioned above differ from SUM 159 cells in their mutational background, and examined Akt responses. When stimulated with 10 ng/mL EGF, these cells exhibit highest Akt responses at pre-existing states of low PI3K and low mTORC1 activity (Figure 3.5B). Notably, at high mTORC1 activity both SUM 159 cells and MDA-MB-231 cells show pre-existing states in the model with no ERK and Akt responsiveness, respectively, identifying an intracellular restraint mechanism that gives rise to no observed signaling in particular cells.

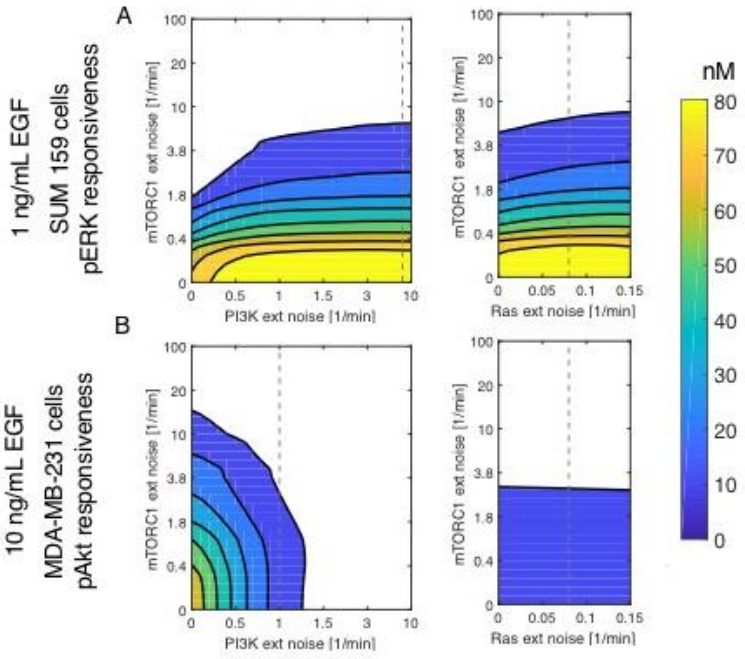

Figure 3.5 The computational model predicts Akt and ERK responsiveness of breast cancer cell lines via EGFR stimulation is a function of pre-existing state

(A) SUM 159 cells show highest ERK responses at pre-existing states characterized by high PI3K and low mTORC1 activity. (B) MDA-MB-231 cells show highest Akt responses at pre-existing states characterized by low PI3K and low mTORC1 activity. The left and right panels illustrate slices through the Ras and PI3K extrinsic noise states, respectively, with the vertical gray dashed line indicating the plane through which the complimentary panel is sliced.

3.4.5 Predicted ERK and Akt responses to higher EGF and CXCL12 doses

After calibrating our computational model and determining the set of pre-existing states of SUM 159 cells, we use the model to predict ERK and Akt signaling behavior at higher doses of both EGF and CXCL12. To predict new signaling behaviors, we assume the same set of pre-existing states as determined in Figure 3.4C, since the pre-existing state is necessarily ligand- and dose- independent. The model predicts the single cell ERK and Akt responses of SUM 159 cells stimulated with higher ligand doses of 10 ng/mL EGF and 100 ng/mL CXCL12 (Figure 3.6A). The model predictions capture the behaviors of single cells across the entire continuum of ERK and Akt responsiveness

(Figure 3.6B). MDA-MB-231 cell Akt responses to EGF or CXCL12 are similarly predicted by the model at higher ligand doses (Figure B2 A), and the model captures the range of all single-cell responses in this cell type as well (Figure B2 B), demonstrating model robustness.

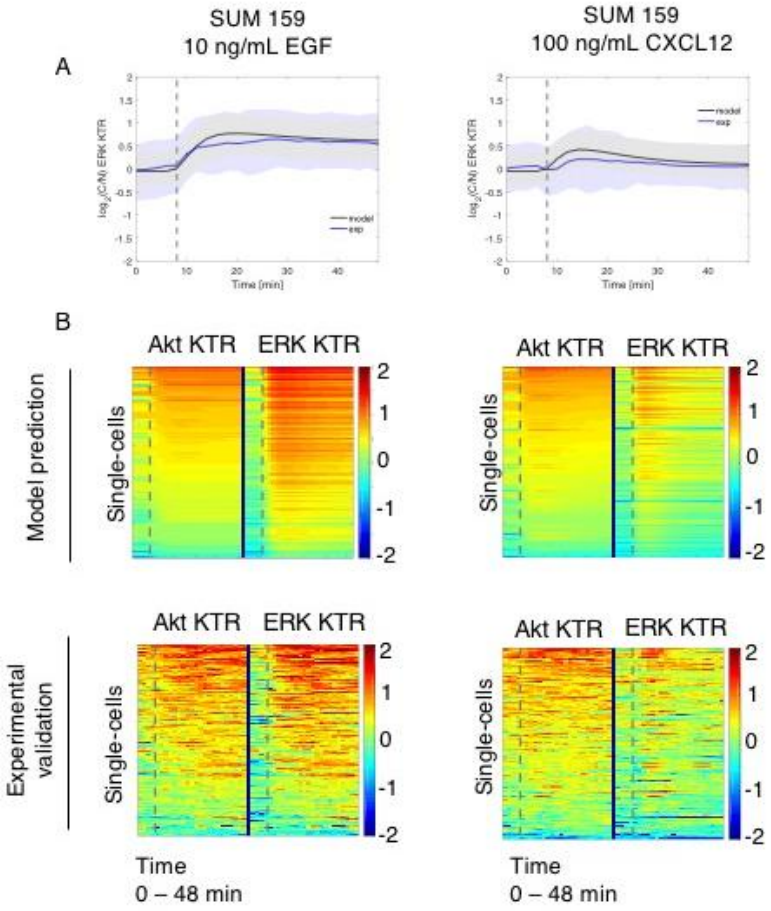

Figure 3.6 The computational model predicts SUM 159 cell Akt and ERK responses to EGF and CXCL12 at new doses given the calculated pre-existing states

(A) The median, 10th, and 90th percentile of the $\log_2$(C/N) of ERK dynamics predicted from the model for SUM 159 cells stimulated with 10 ng/mL EGF (left) and 100 ng/mL CXCL12 (right) match experimental validation. (B) Single-cell time tracks of the predicted (top) and experimental (bottom) Akt and ERK dynamics illustrate that the model captures the entire continuum of responses to EGF (left) and CXCL12 (right) stimulation seen in experiments.

3.4.6 Predicted concentrations of active ERK and Akt in single cells

After validating model signaling responses to EGFR and CXCR4, we analyzed model predictions to study heterogeneity in the concentration of active ERK and Akt in our simulations. For SUM 159 cells, model predictions of ERK responses to 10 ng/mL or 1 ng/mL EGF (Figure 3.7A) and 100 ng/mL or 10 ng/mL CXCL12 (Figure 3.7B) demonstrate the heterogeneity in the amount of active ERK in these cells following stimulation. These single SUM 159 cells map to regions within the population of SUM 159 cells (Figure 3.7C), indicating that these pre-existing states are occupied by experimental cells. The model also predicts Akt responses of single MDA-MB-231 cells at various EGF and CXCL12 doses, and illustrates how pre-existing states among this cell population confer heterogeneous signaling responses to both ligands (Figure B3 A-C). Both breast cancer cell lines contain a wide array of pre-existing cell states which control responsiveness in ERK and Akt through EGFR and CXCR4.

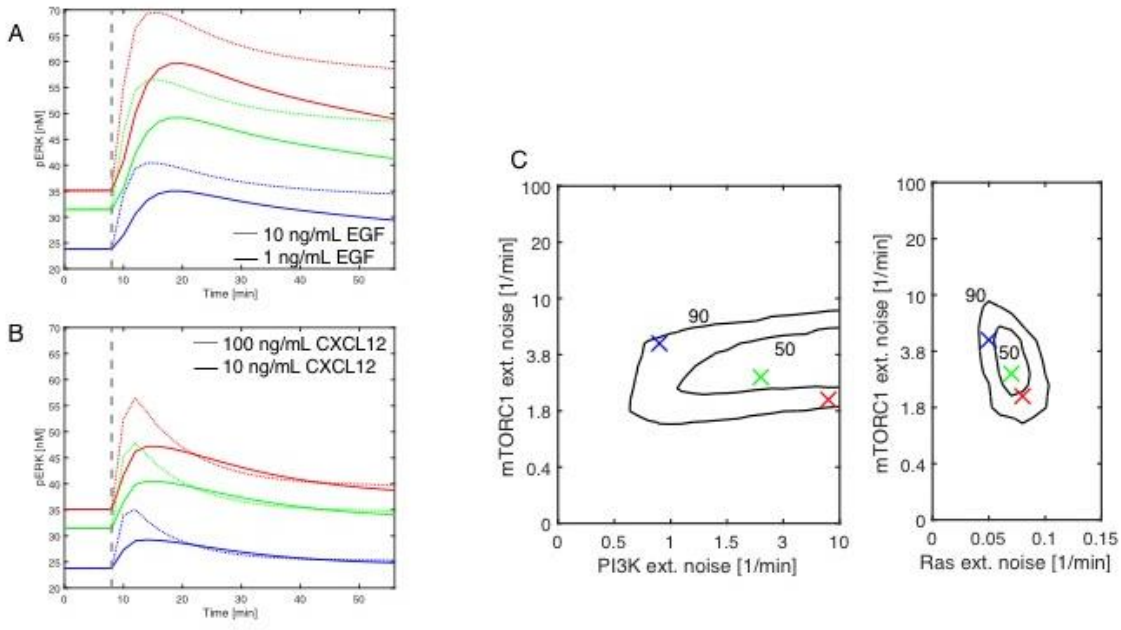

Figure 3.7 Model predictions of ERK concentrations following doses of EGFR or CXCR4 stimulation

(A) SUM 159 cells stimulated with 1 ng/mL (solid line) or 10 ng/mL (dotted line) EGF show heterogeneous predicted ERK responses. Line colors correspond to those in b and c. (B) SUM 159 cells stimulated with 10 ng/mL (solid line) or 100 ng/mL (dotted line) CXCL12 show heterogeneous predicted ERK responses. Line colors correspond to those in A and C. (C). Contour map illustrating the pre-existing states occupied by SUM 159 cells with colored x's indicating the pre-existing states shown in a and c. The

contours represent the 2D projected occupancy map of the experimental cells after being matched in the 3D model library space. The outer and inner contours represent 90 and 50 percent of experimental cells, respectively.

3.4.7 In silico PI3K inhibition of SUM 159 cells

Since SUM 159 cells harbor constitutively active PI3K, we next used the model to make predictions about the effects of PI3K inhibition on responsiveness of SUM 159 cells. Both the basal state, which is the resting ERK and Akt activity prior to ligand stimulation, and responsiveness through either kinase are affected by PI3K inhibition. The model predicts that PI3K inhibition will increase both the basal state (Figure 3.8A) and responsiveness (Figure 3.8B) of ERK in SUM 159 cells, consistent with experimental data reported in literature citing how cells bypass PI3K inhibition by activating ERK (44). Black contours represent the pre-existing states calculated in Figure 3.4D, and are shown here to demonstrate that the SUM 159 cell population exists within a regime where ERK activation is affected by PI3K inhibition. In the model, inhibition of PI3K decreases Akt activity, but releases restraint from Akt on Raf thereby activating ERK. Our model suggests a mechanism by which cells escape PI3K inhibition and upregulate another oncogenic signaling pathway, indicating that inhibiting both the ERK and Akt pathways simultaneously may be necessary even in cells which are more active in one of these pathways (44,45). The ability of the model to predict inadvertent signaling effects of PI3K inhibition highlights how the model can aid in determining the best strategies for targeted therapeutic intervention.

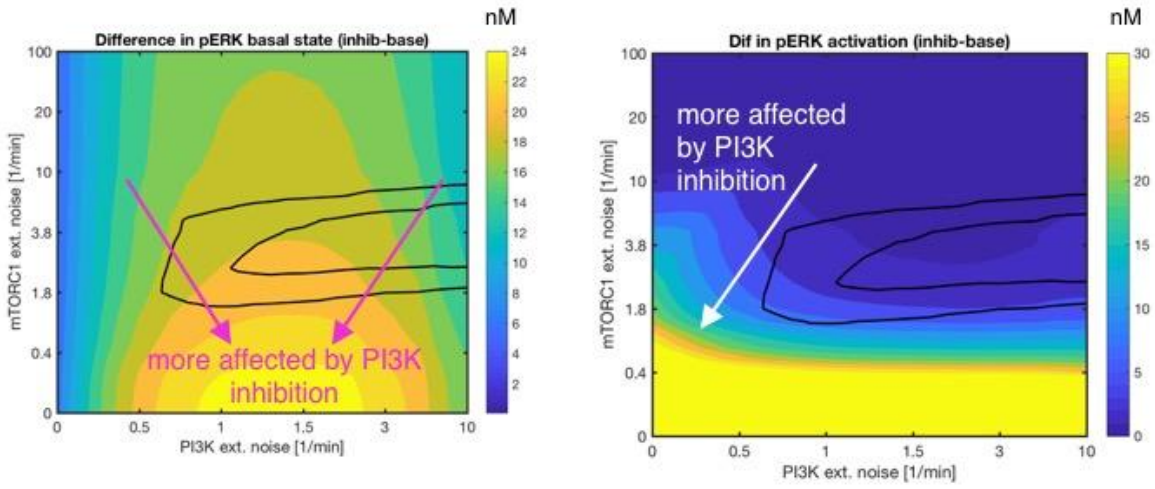

Figure 3.8 PI3K inhibition potentiates EGFR-mediated ERK signaling

(A) Contour map illustrating the change in the basal signaling level of ERK in SUM 159 cells under PI3K inhibition versus control at various pre-existing states. Color indicates the concentration (nM) difference between the basal state under inhibited conditions and control conditions. The plane of the 3D model library shown here is kRas = 0.08 1/min. The two black contours represent the pre-existing states encompassed by 90% (outer) and 50% (inner) of SUM 159 cells. (B) Contour map illustrating the change in the ERK responsiveness of SUM 159 cells under PI3K inhibition versus control at various pre-existing states after 1 ng/mL EGF stimulation. Color indicates the concentration (nM) difference between the responsiveness under inhibited conditions and the responsiveness under control conditions. Shown here is a plane of the 3D model library located at a value of kRas = 0.08 1/min. The two black contours represent the pre-existing states encompassed by 90% (outer) and 50% (inner) of SUM 159 cells.

3.5 Discussion

Cell signaling heterogeneity confounds our ability to understand and treat signaling diseases such as cancer that are driven by small subpopulations of cells. Here, we further develop and test our hypothesis that (i) the source of the heterogeneity is deterministic, not stochastic; (ii) pre-existing cellular states that vary cell-to-cell are the drivers of signaling heterogeneity. We identify a critical test of the CSM model by showing that the model framework can explain heterogeneity in ERK and Akt signaling over multiple doses of ligand to two receptor systems of different families on two cell lines of different mutational backgrounds. Using the model, we confirmed that the ERK and Akt signaling restraint mechanism through mTORC1 is conserved in the EGFR and CXCR4 receptor systems, highlighting a signaling motif which may have implications for targeted therapies of both pathways. We demonstrate the clinical utility of our model by predicting signaling outcomes following targeted therapy administration. For example, in future works, the CSM could predict signaling outcomes from combinations of inhibitors relevant for cancer therapies.

Despite the marked heterogeneity of single-cell Akt and ERK responses to an identical input stimulus, we present a computational model capable of predicting the entire range of responses of both kinases for both EGFR and CXCR4 signaling by varying only three

key parameters. These three key parameters set the activity of PI3K, Ras, and mTORC1 prior to ligand stimulation and define the cellular pre-existing state. We vary these three parameters not because of uncertainty in their values, which is a common approach in computational modeling of biological systems (46,47), but because these three kinases represent nodes which respond to biological stimuli outside of EGFR and CXCR4 signaling which are unaccounted for explicitly in our model (41,48–50). Additionally, we highlight that despite the continuum of possible responses of single cells, our model captures the range of signaling behaviors while holding all biophysical rate constants the same from cell-to-cell in the population, supporting our claim that intrinsic noise in enzyme kinetics is not the primary driver of cell signaling heterogeneity. The fact that the pre-existing cell state can predict signaling responses to both EGFR and CXCR4 stimuli provides support for the argument that variation in receptor expression is not the major driver of heterogeneous signaling responses. This work extends beyond the current paradigm of simply recapitulating cell signaling heterogeneity and examines the root mechanistic sources of variability in signaling.

Single-cell signaling responses are the outputs of robust dynamical systems that retain heterogeneity within cell populations. In the work presented here, we found the variability in the pre-existing states of single cells was always present regardless of cell type, ligand type, or ligand dose. However, pre-existing states are in constant flux with varying environmental cues. Recent work uncovered how we can edit pre-existing cell states to have more or less Akt and ERK responsiveness (6). Harnessing the full potential of controlling the pre-existing state of cell populations may unveil a host of new combination therapy strategies to treat cancer and overcome the inherent heterogeneity of cell signaling responses. In future work, our computational model can be linked to larger-scale quantitative systems pharmacology models to uncover strategies for efficient design of targeted therapeutic regimens.

3.6 References

1. Altschuler SJ, Wu LF. Cellular Heterogeneity: Do Differences Make a Difference? Cell. 2010;141:559–63.
2. Gerdes MJ, Sood A, Sevinsky C, Pris AD, Zavodszky MI, Ginty F. Emerging Understanding of Multiscale Tumor Heterogeneity. Front Oncol. 2014;4(December):1–12.
3. Kim E, Kim J, Smith MA, Haura EB, Alexander R, Anderson A. Cell signaling heterogeneity is modulated by both cell-intrinsic and -extrinsic mechanisms: An integrated approach to understanding targeted therapy. PLoS Biol. 2018;16(3):1–29.
4. Snijder B, Pelkmans L. Origins of regulated cell-to-cell variability. Nat Rev Mol Cell Biol. 2011;12(2):119–25.
5. Gaudet S, Miller-Jensen K. Redefining signaling pathways with an expanding single-cell toolbox. Trends Biotechnol. 2016;34(6):458–69.
6. Spinosa PC, Humphries BA, Lewin Mejia D, Buschhaus JM, Linderman JJ, Luker GD, et al. Short-term cellular memory tunes the signaling responses of the chemokine receptor CXCR4. Sci Signal. 2019;
7. Yao J, Pilko A, Wollman R. Distinct cellular states determine calcium signaling response. Mol Syst Biol. 2016;12(12):894.
8. Cojoc M, Peitzsch C, Polishchuk L, Telegeev G, Dubrovska A. Emerging targets in cancer management: role of the CXCL12/CXCR4 axis. Onco Targets Ther. 2013;6:1347–61.
9. Sobolik T, Su Y, Wells S, Ayers GD, Cook RS. CXCR4 drives the metastatic phenotype in breast cancer through induction of CXCR2 and activation of MEK and PI3K pathways. Mol Biol Cell. 2014;25.
10. Ozawa P, Ariza C, Ishibashi C, Fujita T, Banin-Hirata B, Oda J, et al. Role of CXCL12 and CXCR4 in normal cerebellar developmentand medulloblastoma. Int J Cancer. 2014;138:10–3.
11. Wendel C, Hemping-Bovenkerk A, Krasnyanska J, Mees ST, Kochetkova M, Stoeppeler S, et al. CXCR4/CXCL12 participate in extravasation of metastasizing breast cancer cells within the liver in a rat model. PLoS One. 2012;7(1).
12. Choi YH, Burdick MD, Strieter BA, Mehrad B, Strieter RM. CXCR4, but not CXCR7, discriminates metastatic behavior in non-small cell lung cancer cells. Mol Cancer Res. 2014;12(1):38–47.
13. Kohno M, Pouyssegur J. Targeting the ERK signaling pathway in cancer therapy. Ann Med. 2006;38(3):200–11.
14. Nitulescu GM, Van De Venter M, Nitulescu G, Ungurianu A, Juzenas P, Peng Q, et al. The Akt pathway in oncology therapy and beyond (Review). Int J Oncol. 2018;53(6):2319–31.
15. Seshacharyulu P, Ponnusamy M, Haridas D, Jain M, Ganti A, Batra SK. Targeting the EGFR signaling pathway in cancer therapy. Expert Opin Ther Targets. 2012;16(1):15–31.
16. Sigismund S, Avanzato D, Lanzetti L. Emerging functions of the EGFR in cancer. Mol Oncol. 2018;12(1):3–20.

17. Wee P, Wang Z. Epidermal growth factor receptor cell proliferation signaling pathways. Cancers (Basel). 2017;9(5):1–45.
18. Mosadegh B, Saadi W, Wang SJ, Jeon NL. Epidermal growth factor promotes breast cancer cell chemotaxis in CXCL12 gradients. Biotechnol Bioeng. 2008;100(6):1205–13.
19. Regot S, Hughey JJ, Bajar BT, Carrasco S, Covert MW. High-sensitivity measurements of multiple kinase activities in live single cells. Cell. 2014;157(7):1724–34.
20. Kudo T, Jeknic S, Macklin DN, Akhter S, Hughey JJ, Regot S, et al. Live-cell measurements of kinase activity in single cells using translocation reporters. Nat Protoc. 2017;13(1):155–69.
21. Spinosa PC, Luker KE, Luker GD, Linderman JJ. The CXCL12/CXCR7 signaling axis, isoforms, circadian rhythms, and tumor cellular composition dictate gradients in tissue. PLoS One. 2017;12(11).
22. Coggins NL, Trakimas D, Chang SL, Ehrlich A, Ray P, Luker KE, et al. CXCR7 Controls Competition for Recruitment of β-Arrestin 2 in Cells Expressing Both CXCR4 and CXCR7. PLoS One. 2014;9(6):e98328.
23. Chang SL, Cavnar SP, Takayama S, Luker GD, Linderman JJ. Cell, Isoform, and Environment Factors Shape Gradients and Modulate Chemotaxis. PLoS One. 2015;10(4):e0123450.
24. Hendriks BS, Opresko LK, Wiley HS, Lauffenburger D. Coregulation of Epidermal Growth Factor Receptor/Human Epidermal Growth Factor Receptor 2 (HER2) Levels and Locations: Quantitative Analysis of HER2 Overexpression Effects. Cancer Res. 2003;63:1130–7.
25. Wang DYQ, Cardelli L, Phillips A, Piterman N, Fisher J. Computational modeling of the EGFR network elucidates control mechanisms regulating signal dynamics. BMC Syst Biol. 2009;3:1–17.
26. Bianconi F, Baldelli E, Ludovini V, Crinò L, Flacco A, Valigi P. Computational model of EGFR and IGF1R pathways in lung cancer: A Systems Biology approach for Translational Oncology. Biotechnol Adv [Internet]. 2012;30(1):142–53. Available from: http://dx.doi.org/10.1016/j.biotechadv.2011.05.010
27. Kholodenko BN, Demin O V, Hoek JB, Kholodenko BN, Demin O V, Moehren G, et al. Quantification of Short Term Signaling by the Epidermal Growth Factor Receptor. J Biol Chem. 1999;274(42):30169–81.
28. Schmidt-Glenewinkel H, Reinz E, Eils R, Brady NR. Systems biological analysis of epidermal growth factor receptor internalization dynamics for altered receptor levels. J Biol Chem. 2009;284(25):17243–52.
29. Dawson JP, Berger MB, Lin C, Schlessinger J, Lemmon MA, Ferguson KM. Epidermal Growth Factor Receptor Dimerization and Activation Require Ligand-Induced Conformational Changes in the Dimer Interface. Mol Cell Biol. 2005;25(17):7734–42.
30. Harwood FC, Geltink RIK, Hara BPO, Cardone M, Janke L, Finkelstein D, et al. ETV7 is an essential component of a rapamycin-insensitive mTOR complex in cancer. Sci Adv. 2018;4:1–18.
31. Ballou LM, Lin RZ. Rapamycin and mTOR kinase inhibitors. J Chem Biol. 2008;1:27–36.

32. Sarbassov DD, Ali SM, Sengupta S, Sheen J, Hsu PP, Bagley AF, et al. Prolonged Rapamycin Treatment Inhibits mTORC2 Assembly and Akt/PKB. Mol Cell. 2006;159–68.
33. Marino S, Hogue IB, Ray CJ, Kirschner DE. A Methodology for Performing Global Uncertainty and Sensitivity Analysis in Systems Biology. Vol. 254, Journal of Theoretical Biology. 2009. 178–196 p.
34. McKay MD, Beckman RJ, Conover WJ. A comparison of three methods for selecting values of input variables in the analysis of output from a computer code. Technometrics. 1979;21(2):239–45.
35. Hollestelle A, Elstrodt F, Nagel JHA, Kallemeijn WW. Phosphatidylinositol-3-OH Kinase or RAS Pathway Mutations in Human Breast Cancer Cell Lines. Mol Cancer Res. 2007;5(2):195–201.
36. Klein P, Lemmon MA, Lax I, Schlessinger J. On the nature of low- and high-affinity EGF receptors on living cells. PNAS. 2006;103(15).
37. Domanska UM, Kruizinga RC, Nagengast WB, Timmer-Bosscha H, Huls G, De Vries EGE, et al. A review on CXCR4/CXCL12 axis in oncology: No place to hide. Eur J Cancer. 2013;49(1):219–30.
38. Mendoza M, Emrah Er E, Blenis J. The Ras-ERK and PI3K-mTOR Pathways: Cross-talk and Compensation. Trends Biochem Sci. 2011;36(6):320–8.
39. Posada IMD, Lectez B, Siddiqui FA, Oetken-Lindholm C, Sharma M, Abankwa D. Opposite feedback from mTORC1 to H-ras and K-ras4B downstream of SREBP1. Sci Rep. 2017;7(1):1–14.
40. Kaschek D, Hahn B, Wrangborg D, Karlsson J, Kvarnström M. Heterogeneous kinetics of AKT signaling in individual cells are accounted for by variable protein concentration. Front Physiol. 2012;3(45):1–14.
41. Yuan TL, Wulf G, Burga L, Cantley LC. Cell-to-cell variability in PI3K protein level regulates PI3K-AKT pathway activity in cell populations. Curr Biol. 2011;21(3):173–83.
42. Iwamoto K, Shindo Y, Takahashi K. Modeling Cellular Noise Underlying Heterogeneous Cell Responses in the Epidermal Growth Factor Signaling Pathway. PLoS Comput Biol. 2016;12(11):1–18.
43. Sumit M, Jovic A, Neubig RR, Takayama S, Linderman JJ. A Two-Pulse Cellular Stimulation Test Elucidates Variability and Mechanisms in Signaling Pathways. Biophys J. 2019;116:962–73.
44. Serra V, Scaltriti M, Prudkin L, Eichhorn PJA, Ibrahim YH, Chandarlapaty S, et al. PI3K inhibition results in enhanced HER signaling and acquired ERK dependency in HER2-overexpressing breast cancer. Oncogene [Internet]. 2011;30(22):2547–57. Available from: http://dx.doi.org/10.1038/onc.2010.626
45. Kuo Y-H, Chiang E-PI, Chao C-Y, Rodriguez RL, Chou P-Y, Tsai S-Y, et al. Dual Inhibition of Key Proliferation Signaling Pathways in Triple-Negative Breast Cancer Cells by a Novel Derivative of Taiwanin A. Mol Cancer Ther. 2017;16(3):480–93.
46. van Mourik S, ter Braak C, Stigter H, Molenaar J. Prediction uncertainty assessment of a systems biology model requires a sample of the full probability distribution of its parameters. PeerJ. 2014;2:e433.
47. Vanlier J, Tiemann C, Hilbers P, van Riel N. Parameter uncertainty in biochemical

models described by ordinary differential equations. Math Biosci. 2013;246(2):305–14.
48. Cintas C, Guillermet-Guibert J. Heterogeneity of Phosphatidylinositol-3-Kinase (PI3K)/AKT/Mammalian Target of Rapamycin Activation in Cancer: Is PI3K Isoform Specificity Important? Front Oncol. 2018;7.
49. Jeantet M, Tougeron D, Tachon G, Cortes U, Archambaut C, Fromont G, et al. High intra-and inter-tumoral heterogeneity of RAS mutations in colorectal cancer. Int J Mol Sci. 2016;17(12).
50. Saxton RA, Sabatini DM. mTOR Signaling in Growth, Metabolism, and Disease. Cell. 2017;168(6):960–76.

Chapter 4 The CXCL12/CXCR7 Signaling Axis, Isoforms, Circadian Rhythms, and Tumor Cellular Composition Dictate Gradients in Tissue

This chapter is a published work:

Spinosa PC, Luker KE, Luker GD, Linderman JJ. The CXCL12/CXCR7 signaling axis, isoforms, circadian rhythms, and tumor cellular composition dictate gradients in tissue. PLoS One. 2017;12(11).

4.1 Abstract

Chemokine CXCL12 gradients drive chemotaxis in a CXCR4-dependent mechanism and have been implicated in cancer metastasis. While CXCL12 gradients are typically studied in organized, defined environments, the tumor microenvironment is disorganized. *In vivo,* CXCL12 gradients depend on many factors: the number and arrangement of cells secreting and degrading CXCL12, isoform-dependent binding to the extracellular matrix, diffusion, and circadian fluctuations. We developed a computational model of the tumor microenvironment to simulate CXCL12 gradient dynamics in disorganized tissue. There are four major findings from the model. First, CXCL12-β and -γ form higher magnitude (steeper) gradients compared to CXCL12-α. Second, endothelial CXCR7+ cells regulate CXCL12 gradient direction by controlling concentrations near but not far from the vasculature. Third, the magnitude and direction of CXCL12 gradients are dependent on the local composition of secreting and scavenging cells within the tumor. We theorize that “micro-regions” of cellular heterogeneity within the tumor are responsible for forming strong gradients directed into the blood. Fourth, CXCL12 circadian fluctuations influence gradient magnitude but not direction. Our simulations provide predictions for future experiments in animal models.

Understanding the generation of CXCL12 gradients is crucial to inhibiting cancer metastasis.

4.2 Introduction

Chemokine CXCL12, alternatively called stromal cell-derived factor 1 (SDF-1), has been implicated in cancer metastasis and is a known driver of chemotaxis via chemokine receptor CXCR4 (1–4). Common sites of breast cancer metastasis, including bone, liver, and brain, express high levels of CXCL12 (3,5). Staining data demonstrate spatial heterogeneity of CXCL12 in tumors (2,6), suggesting that CXCL12 gradients exist *in vivo*. In *in vivo* models, CXCR4 antagonist AMD3100 (Plerixafor) decreases primary tumor size and/or metastatic burden, but metastatic disease is not cured (7–9). One theory of the metastatic mechanism is that cancer cells use dynamic chemokine gradients in their local environments to travel from primary to secondary tumor sites. CXCL12 gradient dynamics remain unclear, and yet understanding these gradients *in vivo* is crucial to grasping the mechanism that drives cancer cells along the metastatic cascade.

CXCL12 has two known receptors, CXCR4 and CXCR7, which are involved in responding to and forming the CXCL12 gradient, respectively (10–12). Many cell types in tumors secrete CXCL12, most notably cancer-associated fibroblasts. When CXCL12 binds to CXCR4, the receptor is internalized and a cascade of intracellular signaling events commences, culminating in a chemotactic response, cell survival, and proliferation. However, when CXCL12 binds to CXCR7, the chemokine is rapidly internalized and degraded, facilitating gradient formation (12), and a chemotactic response does not result (13). CXCR7 is expressed throughout the tumor and is substantially upregulated on tumor-associated vasculature (14–17). Endothelial CXCR7 is a key regulator of systemic CXCL12 blood plasma levels, which is unsurprising due to its location (18). However, the role of endothelial CXCR7 with regards to CXCL12 gradients in tissue is unknown. In fact, it is difficult to fathom how cancer cells use chemokine gradients to intravasate into blood vessels if endothelial CXCR7 is present

to scavenge CXCL12. Therefore, we asked how, why, and when CXCL12 gradients could be directed towards blood vessels. In this work, we study CXCL12 gradients in tumor geometries that are likely to exist *in vivo* while simultaneously examining the role of endothelial CXCR7.

Multiple mechanisms govern CXCL12 gradients *in vivo*. As CXCL12 is secreted in the tumor environment, it diffuses away, binds to extracellular matrix (ECM), and is degraded by both cellular and extracellular means. Alternative splicing generates six isoforms of CXCL12 (19), three of which are found in notable abundance in tumors and other sites in the body: CXCL12-α, -β, and -γ (20). The isoforms bind nonspecifically to ECM with different affinities based on numbers of positively charged amino acids. CXCL12-γ binds to ECM with the highest affinity, followed by CXCL12-β and CXCL12-α, respectively (21); their secretion rates from fibroblasts follow an opposite trend, with CXCL12-α being the highest (22). Binding to ECM increases the local concentration of chemokine while also affording protection from both extracellular and cellular degradation (23). Protection from degradation creates a slower effective diffusivity, thus creating isoform-specific gradients in tissue. Our group has found that CXCR4+ cancer cell migration in 2D is CXCL12 isoform-specific (22,24), but isoforms have not been examined and compared in 3D settings. In addition, CXCL12 levels in all tissues tend to vary according to the circadian rhythm up to 2-fold throughout a 24-h period (25,26), implying that tissue-level gradients are also time-dependent on this scale. The effect of circadian processes on tumor development, progression, and response to therapy is listed as a recent National Cancer Institute Provocative Question (27). Previously, we calculated that cancer cells respond to CXCL12 gradients as small as 0.002 nM/μm (22); circadian fluctuations might cause gradients to fall above and below this value throughout the course of a day. Since CXCR7 rapidly scavenges CXCL12, we questioned whether endothelial CXCR7 could modulate the effects of circadian fluctuations in the blood due to location between a tissue producing the chemokine and the vasculature. These dynamics collectively impact CXCL12 gradients in tissue.

We developed a computational model to simulate CXCL12 gradients in a tumor. We capture the geometry, cellular environment, and blood dynamics of a small tumor section and examine the magnitude, direction, and time variation of CXCL12 gradients. By studying CXCL12 gradient dynamics in a relevant, *in vivo*-like setting computationally, we can learn the major drivers of gradient formation, in particular the roles that CXCL12 isoforms, endothelial CXCR7, tumor composition, and circadian rhythms play. We seek to understand whether these mechanisms can form gradients directed into the blood despite the presence of endothelial CXCR7. Finally, we identify future experiments that can test our predictions regarding the influence of these drivers on cell migration and metastasis.

4.3 Methods

4.3.1 Model overview

Our computational model simulates CXCL12 transport in the tumor microenvironment. Cells exist in discrete locations within tumors. We use a 3D square lattice grid environment to place cells in distinct grid compartments, which allows us to alter the tumor cellular composition and distribution. We use two cell types: CXCL12-secreting cells and CXCR7+ cells. These cells represent fibroblasts and CXCR7+ tumor cells, respectively. CXCR7+ cells are dispersed throughout the tumor or lining the blood vessel, which spans the center of the grid. Each grid compartment has a side length of 10 μm, and can hold at most a single cell. The entire grid is a 200-μm cube. We simulate CXCL12 secretion, diffusion, degradation, binding, a blood vessel that can act as a source of CXCL12 for the tissue, and circadian fluctuations to depict the tumor microenvironment. Model details are given in Appendix Tables C1-C5.

4.3.2 CXCL12 secretion, diffusion, and extracellular degradation

CXCL12-secreting cells secrete CXCL12 into the grid compartment the cell occupies and the chemokine diffuses away. Cells in any given simulation only secrete one CXCL12 isoform. Diffusion is solved using an Alternating Direction Explicit method (28). We use no flux boundary conditions on the edges of the grid because we assume our

model captures the dynamics of a small piece of tumor tissue and is surrounded by repeating similar units. Extracellular degradation of chemokine occurs according to first-order kinetics (29). The timestep for secretion, diffusion, and extracellular degradation is 0.1 s.

4.3.3 CXCL12 binding to receptors and to ECM

Receptor-mediated CXCL12 uptake by CXCR7+ cells, i.e. specific binding at the cell surface and intracellular trafficking of CXCL12 and CXCR7, is described by a set of previously published ordinary differential equations (22,30). CXCR4+ cells, which can also take up CXCL12, may additionally influence CXCL12 gradients. However, we assume that most CXCL12 degradation in tumors occurs via CXCR7 for three reasons: 1) the affinity of CXCL12 is approximately two orders of magnitude greater for CXCR7 than CXCR4 (31,32), 2) CXCR7 is often colocalized with CXCL12 (33), and 3) CXCR7 and CXCR4 are expressed in approximately the same levels (14).

On every diffusion timestep (0.1 s), CXCL12 binds to ECM in its grid compartment according to first-order kinetics and characterized by dissociation constant K_D (22). Each grid compartment is associated with a free and ECM-bound CXCL12 concentration. We assume CXCR7+ cells can bind free and ECM-bound CXCL12 with the same binding parameters. When calculating CXCL12 gradients, we take the difference of the sum of the free and bound concentrations across a distance.

4.3.4 CXCL12 circadian fluctuation and transport across the blood vessel wall

The presence of CXCL12 circadian fluctuations *in vivo* is attributed to a time-dependent secretion rate from cells in the body. However, because we model only a small tumor volume ($8x10^{-3}$ mm^3), we assume that any CXCL12 secreted from cells has no significant effect on CXCL12 blood concentration. In contrast, blood can deliver CXCL12 *to* the portion of the tumor that we simulate because we cannot neglect the influence of CXCL12-secreting cells at sites far from the simulated tumor. We represent

the CXCL12 secreted by distant cells by assuming a bulk blood CXCL12 concentration. The CXCL12 secretion rate from cells is time-dependent while the blood fluctuation is simultaneously impressed on the system. The blood concentration varies temporally but not spatially within the vessel. The circadian variation takes the form $y = A\cos[\mathrm{B}(\mathrm{t} - (\mathrm{C} - \mathrm{D}))] + \mathrm{E}$, which allows us to characterize the amplitude, period, intercept, and time offset of the CXCL12 blood dynamics and cellular secretion rate according to:

$$X(t) = \left(\frac{X_{max} - X_{min}}{2}\right)\cos\left(2\pi f(t - (t_{start} - t_{max})\right) + \left(\frac{X_{max} + X_{min}}{2}\right) \quad (1)$$

where X is either the secretion rate or CXCL12 blood concentration, X_{max} and X_{min} are maximum and minimum values of X, f is the frequency, and t_{start} and t_{max} are the time of day to start the simulation and the time at which maximum CXCL12 secretion and blood levels are observed (25), respectively.

CXCL12 transport from blood to tissue occurs according to a mass transfer boundary condition as shown by:

$$\frac{dn}{dt} = pA(C_{blood} - C_{endo}) \quad (2)$$

where n is the moles of CXCL12 transported from blood to tissue, p is the vascular permeability to CXCL12, A is the surface area of the blood vessel seen by endothelial grid compartments, and C_{blood} and C_{endo} are the blood concentration and tissue concentration just outside the blood vessel wall, respectively.

4.3.5 3D tumor-like geometries

In order to simulate a tumor microenvironment, we place cells in geometries that are likely to occur *in vivo* (2,6,14–17). A blood vessel is centered on the grid and can deliver CXCL12 to the surrounding tissue. CXCL12-secreting cells are placed randomly throughout the grid. CXCR7+ cells fall into one of two classes: tissue (non-endothelial) CXCR7+ cells, which are scattered randomly throughout the grid, or endothelial CXCR7+ cells, which line the blood vessel wall. No cells are seeded inside the blood vessel. We use a baseline of 200 cells of each type unless otherwise specified. We assume no cell motion since CXCL12-secreting cells and CXCR7+ cells do not exhibit chemotactic mobility (17,34). Cells such as macrophages, lymphocytes and T cells that

are present in tumors are assumed to occupy any remaining grid compartments; our focus here is on cell types that most notably directly impact CXCL12 gradients. Because of the randomness in initial cell placement, we average our model outputs over five runs.

4.3.6 Model implementation

We study CXCL12 gradients using the model components described above. We use our model in two distinct setups.

In Setup 1 we examine CXCL12 isoform-specific gradients. CXCL12-secreting and CXCR7+ cells are placed in clusters 100 μm apart (Figure 4.1A). The clusters are confined to a cube region of side length equal to six cell diameters. We vary the number of cells and randomize their locations within each cluster while holding the confinement volume constant (bounded by black dotted lines in Figure 4.1A). The mechanisms in this setup are secretion, diffusion, extracellular degradation, and binding to ECM and CXCR7. There is no blood vessel and no circadian rhythm in these simulations; cells secrete at the baseline rate S (Appendix Table C4). When the simulation begins, CXCL12 gradients form and we track ligand concentrations throughout the grid. The outputs are the cell-derived CXCL12 gradient, the total amount of CXCL12 on the grid, and the time elapsed before steady state is reached. Steady state in this model setup is operationally defined as being reached when the cell-derived gradient changes by less than 0.1 nM/μm over 5 min.

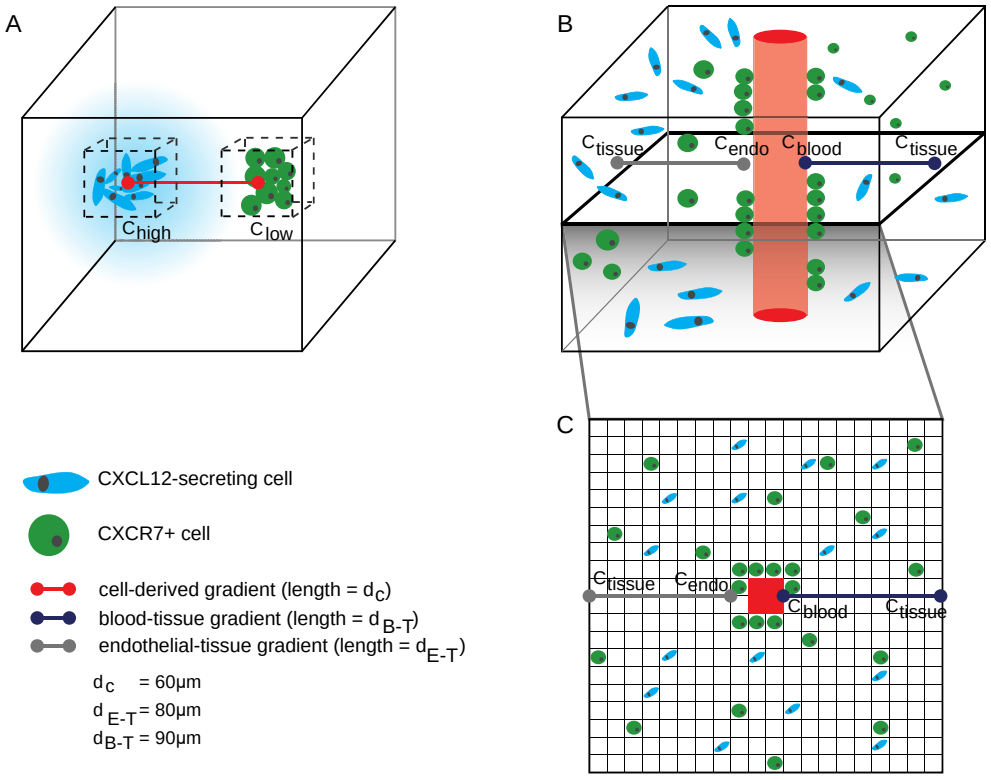

Figure 4.1 Model setups

(A) In Setup 1, we capture the cell-derived CXCL12 gradient along the red line formed in the presence of clusters of CXCL12-secreting cells and CXCR7+ cells to examine the characteristics of isoform-specific gradients. (B) In Setup 2, we simulate a section of a tumor and calculate the blood-tissue and endothelial-tissue gradients. All variables shown in figure are detailed in Appendix Table C5. (C) A cross-sectional slice of the grid used for Setup 2.

In Setup 2 we examine *in vivo*-like CXCL12 gradients in the disorganized tumor microenvironment. We simulate a centralized blood vessel, cells in 3D tumor-like geometries, and circadian fluctuations (Figure 4.1B). The blood vessel is modeled as a

rectangular prism with a cross-sectional area of 400 μm^2. The blood vessel spans the entire height of the simulation space. A 2D slice of the grid is shown in Figure 4.1C. There are two stages to this simulation. First, we initialize the grid with CXCL12 to mimic a snapshot of the tumor environment at a single time point. To do this, we place cells and simulate CXCL12 secretion, diffusion, degradation, binding to ECM and CXCR7, and transport from blood to tissue until steady state. Circadian fluctuations in cell secretion rate and blood levels are not modeled during this initialization stage because they occur at the slowest time scale, on the order of hours. Second, we introduce circadian fluctuations, both in the secretion rate from cells and the CXCL12 blood levels. The output using this model setup is the time-dependent magnitude and direction of the CXCL12 gradient. We arbitrarily define positive gradients as situations where the CXCL12 concentration is higher in the tissue than in the blood, and negative gradients as situations where the CXCL12 concentration is higher in the blood than the tissue.

The model is coded in C++ and all subsequent analyses are performed using in-house MATLAB scripts (The MathWorks, Inc., Natick, MA). All simulations were performed on the University of Michigan's HPC cluster.

4.3.7 CXCL12 measurements in mice

The University of Michigan IACUC approved all animal procedures. To determine the effect of endothelial CXCR7 on CXCL12 circadian rhythms, we measured CXCL12 levels in plasma, femur, and tibia from C57BL/6 mice (WT) and mice with conditional deletion of CXCR7 from vascular endothelium (SCL Cre+) (35). We collected 100 µL blood samples into tubes coated with 20mM EDTA. Samples were centrifuged at 16,100g for 10 minutes at 4°C to collect plasma. For the femur and tibia samples, we flushed each bone with 100 µL sterile PBS to harvest bone marrow. We centrifuged samples at 1,600g for 5 minutes to pellet bone marrow cells and collected the supernatant for ELISA. All samples were collected at the times indicated. The mice were housed with 12-hour light/dark cycle from 6am to 6pm. All samples were stored at

-80°C prior to ELISA for CXCL12 (R&D Systems), performed by the University of Michigan Cancer Center Immunology Core. Mice were euthanized with a CO_2 overdose.

4.4 Results

4.4.1 CXCL12-β and -γ are associated with longer gradient formation times, higher gradient magnitudes, and higher tissue concentrations than CXCL12-α

CXCL12 isoforms differ in their secretion rates from cells as well as their binding to ECM. We investigated how isoforms can differentially modulate gradients in a 3D environment. Using Setup 1, we placed a cluster of CXCL12-secreting cells and a cluster of CXCR7+ cells in our simulation (Figure 4.1A). We varied the CXCL12 secretion rate and CXCL12-ECM binding affinity to encompass known values for the α, β, and γ isoforms. As the secretion rate or the affinity increased, the cell-derived CXCL12 gradient magnitude increased (Figure 4.2A), consistent with published 2D simulations of a microfluidic source-sink device (22). In addition, the time to reach steady state also increased. CXCL12-γ was able to maintain higher concentrations near source cells because of the lower effective diffusivity caused by binding to the ECM (Figure 4.2B). For each isoform, greater numbers of scavenging cells decreased the total amount of CXCL12 on the grid (Figure 4.2C) but had little effect on the magnitude of the gradient between the clusters (Figure 4.2D). Because the binding affinity of CXCL12 for CXCR7 is high, just a few CXCR7+ cells can degrade nearly all of the nearby CXCL12, so additional CXCR7+ cells have little effect. As the number of CXCL12-secreting cells increased, the amount of CXCL12 on the grid and gradient magnitudes increased, indicating that the number of source cells can have a substantial impact on gradients (Figure 4.2C,D). Taken together, these data imply that cell-derived CXCL12-β and -γ within tumor tissue form stronger gradients and create environments richer in CXCL12 than cell-derived CXCL12-α.

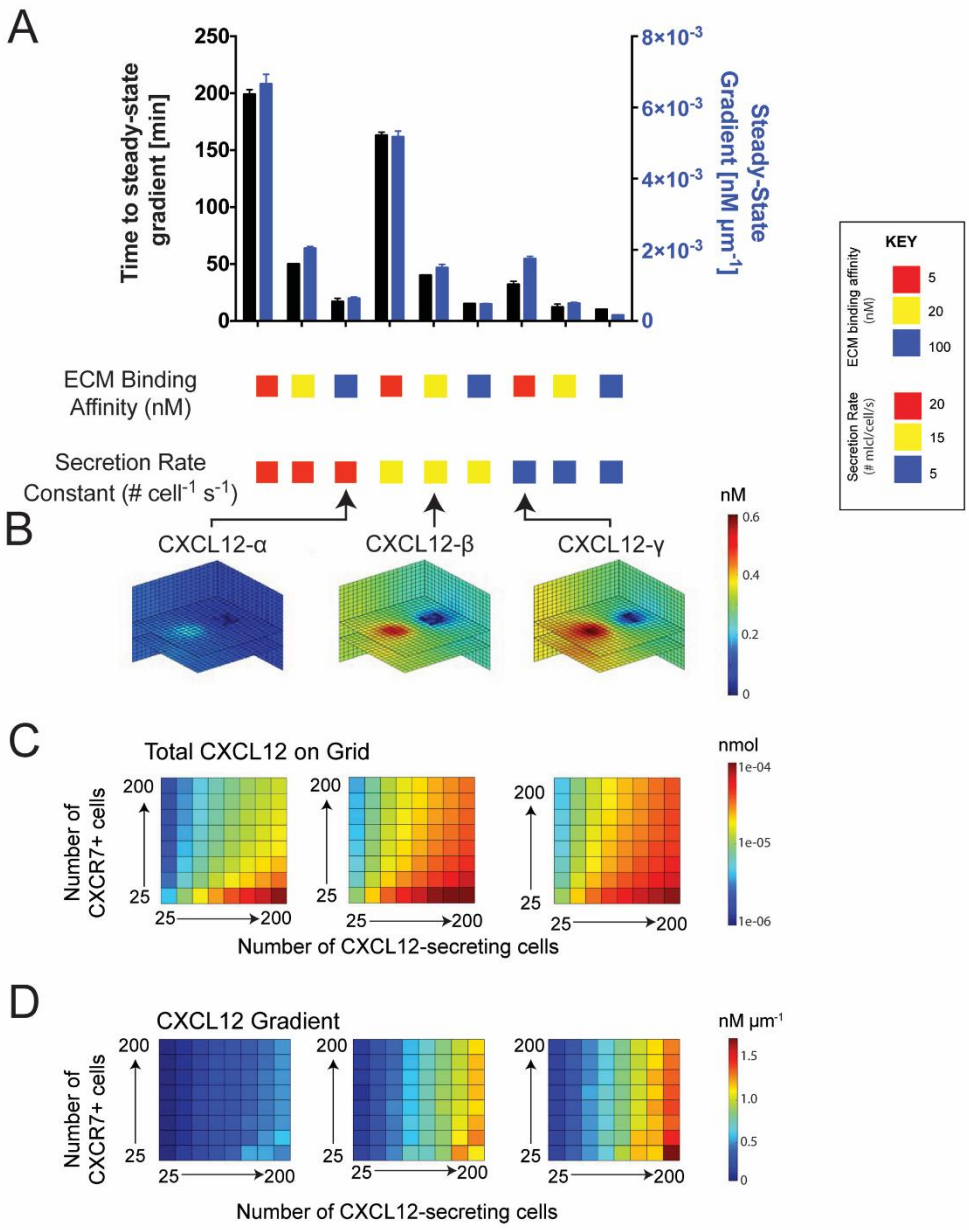

Figure 4.2 Cell-derived CXCL12 gradients are isoform-specific with regards to the time to steady state, gradient magnitude, and amount of CXCL12 in the proximate environment

(A) Higher ECM binding affinity and higher secretion rate correspond to a higher gradient magnitude, but a longer time to form it. Error bars represent SEM of 5 simulations. Both clusters contain 100 cells. Cell clusters are placed 100 µm apart. (B) CXCL12 gradients and total concentrations in the tissue vary with each isoform. Cell numbers were the same as in A. (C) CXCL12-β (center) and -γ (right) create microenvironments with higher CXCL12 concentrations than CXCL12-α (left). On each plot, the x- and y-axes correspond to the number of cells in each cluster: 25, 50, 75,

100, 125, 150, 175, 200. (D) The number of CXCL12-secreting cells in a cluster influences gradients, while the effect of the number of CXCR7+ cells is less pronounced. The x- and y-axes are the same as in C. For C and D, free and ECM-bound CXCL12 was summed. For all simulations in this figure, an average over 5 simulations is reported.

4.4.2 Endothelial CXCR7 decreases CXCL12 levels during circadian fluctuations

Before moving on to tumor microenvironment simulations, we wanted to understand the interdependence of circadian fluctuations in CXCL12 concentrations and endothelial CXCR7 cells. CXCL12 secreted from cells must bypass endothelial CXCR7 cells to enter the blood, and endothelial CXCR7 regulates systemic CXCL12 plasma levels (18). We questioned whether endothelial CXCR7 may disrupt circadian fluctuations. We measured CXCL12 levels at 5 am (0500) and 8 pm (2000) in WT and SCL Cre+ mice, from which we inducibly deleted CXCR7 from vascular endothelium. In the blood, femur, and tibia, CXCL12 levels were 2-fold higher at 8 pm compared to 5 am in both WT and SCL Cre+ mice, indicating circadian fluctuations are independent of endothelial CXCR7. As expected, SCL Cre+ mice showed higher levels of CXCL12 in the blood, femur, and tibia compared to WT (Figure 4.3A). Based on these data, we incorporated a 2-fold cosinusoidal variation in the CXCL12 blood level over 24-h according to Eq. (1) in our model. Our computational model is calibrated to human data rather than mice. We consulted literature to determine human CXCL12 levels (36). The amount of each CXCL12 isoform in the blood follows the same trend as the cellular secretion rate: CXCL12-α > CXCL12-β > CXCL12-γ. We use human time-dependent CXCL12 blood levels in our model (Figure 4.3B). Given these data, we are equipped to include circadian fluctuations and endothelial CXCR7+ cells in our model of the tumor microenvironment.

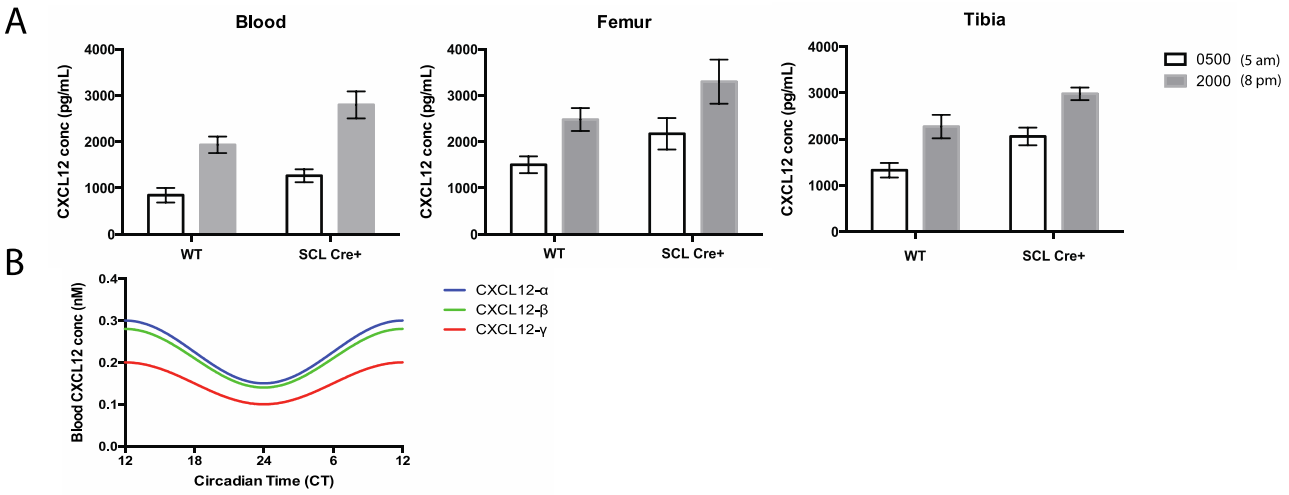

Figure 4.3 CXCL12 circadian fluctuations in CXCL12 concentration occur independent of endothelial CXCR7

(A) Blood (left), femur (center), and tibia (right) CXCL12 levels vary 2-fold between 5 am and 8 pm. Error bars represent SEM of 5 repeated measurements per group of mice. (B) CXCL12 isoform-specific human blood variations that we use in our model (Eq. (1)). CT 24 corresponds to 9 pm while CT 12 corresponds to 9 am. For humans, we offset the time at which the maximum and minimum blood levels occur in the mice by 12 hours because mice are nocturnal. Mice and humans exhibit CXCL12 blood level maxima at night and in the morning, respectively.

4.4.3 Endothelial CXCR7 influences CXCL12 gradient direction by regulating concentrations near but not far from the vasculature

Tumor-associated vasculature expresses endothelial CXCR7 that scavenges CXCL12. We investigated the ability of endothelial CXCR7 to control the direction of the CXCL12 gradient. We ran simulations of the tumor microenvironment (Setup 2, Figure 4.1B, C) for 24 hours and included two circadian sources of CXCL12: CXCL12 in the blood and CXCL12 secreted by cells within the tissue. We ran simulations both with and without endothelial CXCR7+ cells present and monitored the maximum endothelial-tissue gradient direction. When endothelial CXCR7+ cells were absent, the endothelial-tissue gradient was negative, indicating CXCL12 levels were higher near the vasculature than deeper in the tissue, and the gradient points towards the vasculature. In contrast, when endothelial CXCR7+ cells were present, the endothelial-tissue gradient was positive, indicating CXCL12 levels were higher deeper in the tissue than near the vasculature, and the gradient points into the tissue (Figure 4.4A). The magnitudes of the gradients were isoform-dependent. The isoforms with higher ECM binding affinity (CXCL12-β and -γ) maintained higher concentrations in the tissue, as anticipated from the results of Figure 4.2. The concentration profile from the vasculature through the tissue demonstrates that endothelial CXCR7+ cells regulate CXCL12 levels near the blood vessel, but they have a much smaller effect farther (90 μm) away (Figure 4.4B). From these data, we conclude that endothelial CXCR7 regulates gradient directions by scavenging CXCL12 near but not far from the vasculature.

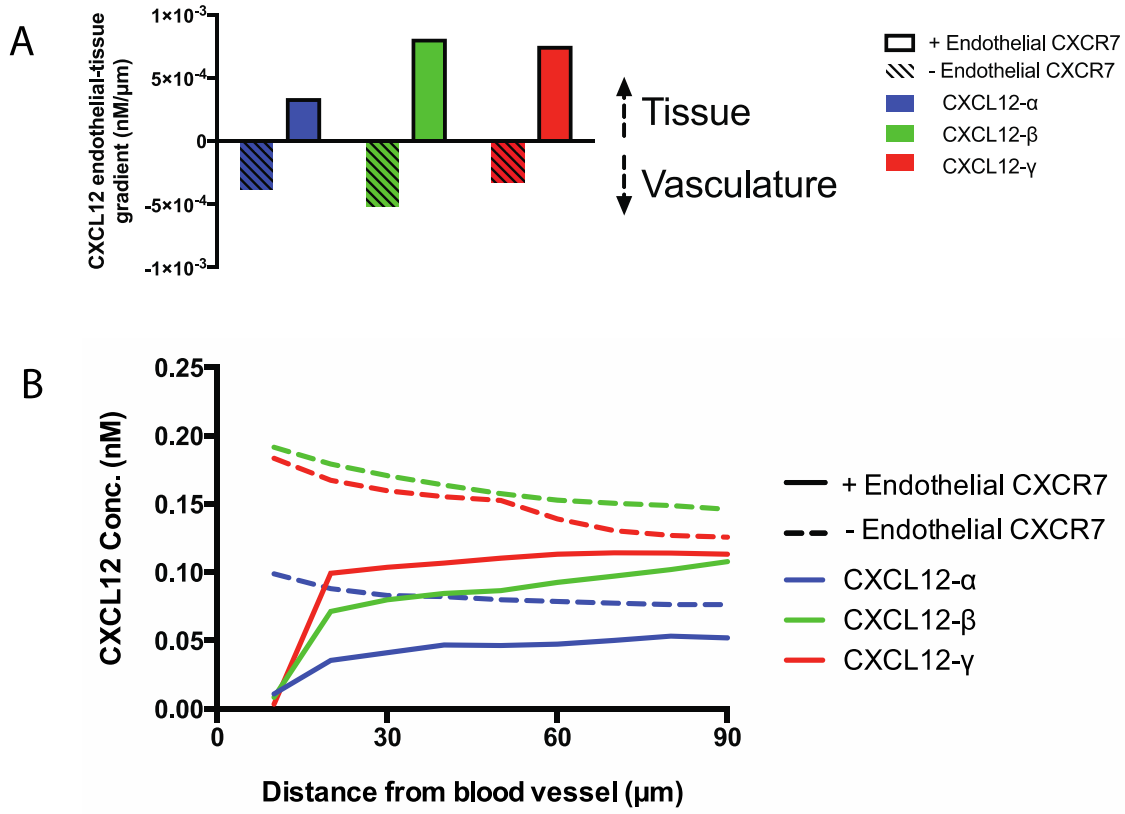

Figure 4.4 Endothelial CXCR7 influences CXCL12 gradient direction by controlling CXCL12 concentrations near but not far from the vasculature

200 endothelial CXCR7 cells (83% coverage of the blood vessel), 200 CXCL12-secreting cells, and 200 CXCR7+ cells in tissue were placed in the simulation. (A) Locally, endothelial CXCR7+ cells scavenge CXCL12 and influence the endothelial-tissue gradient direction. We arbitrarily define positive gradients as those that point from the vasculature to the tissue, and negative gradients point from the tissue to the vasculature. Maximum gradients over a 24-hour simulation are shown. (B) CXCL12 concentration profiles (corresponding to the maximum gradients shown in A) indicate endothelial CXCR7 significantly decreases concentrations near the blood vessel and

has a much lower effect far away. Curves begin at 10μm because this designates the first grid compartment next to the vasculature (Setup 2, Figure 4.1B,C).

4.4.4 Local tumor cellular composition influences both CXCL12 gradient magnitude and direction, while circadian fluctuations only influence gradient magnitude

Because endothelial CXCR7 influences CXCL12 gradients in tumors, we also questioned how CXCR7+ cells deeper within tissue influence gradient magnitude and direction. Using Setup 2 (Figure 4.1B,C), we varied the number of CXCL12-secreting and -scavenging cells (non-endothelial CXCR7+ cells) in the tumor simulation. In all cases, endothelial CXCR7+ cells were also present. Predicted CXCL12 blood-tissue gradients over a 24 hour period, both magnitude and direction, are shown in Figure 4.5. The maximum blood-tissue gradient observed over this time interval is depicted in Figure 4.5A. CXCL12-α gradients were mostly directed into the blood, except at high CXCL12-secreting and low CXCR7+ cell numbers (Figure 4.5A, left). CXCL12-γ gradients are somewhat more likely to be directed into the tissue (Figure 4.5A, right). CXCL12-β blood-tissue gradients lie between CXCL12-α and -γ (Figure 4.5A, center). Isoforms with higher ECM binding affinity can more easily form gradients directed into the tissue. Overall, these results demonstrate that the CXCL12 gradient direction and magnitude depend on the numbers of CXCL12-secreting and non-endothelial scavenging cells present as well as the CXCL12 isoform.

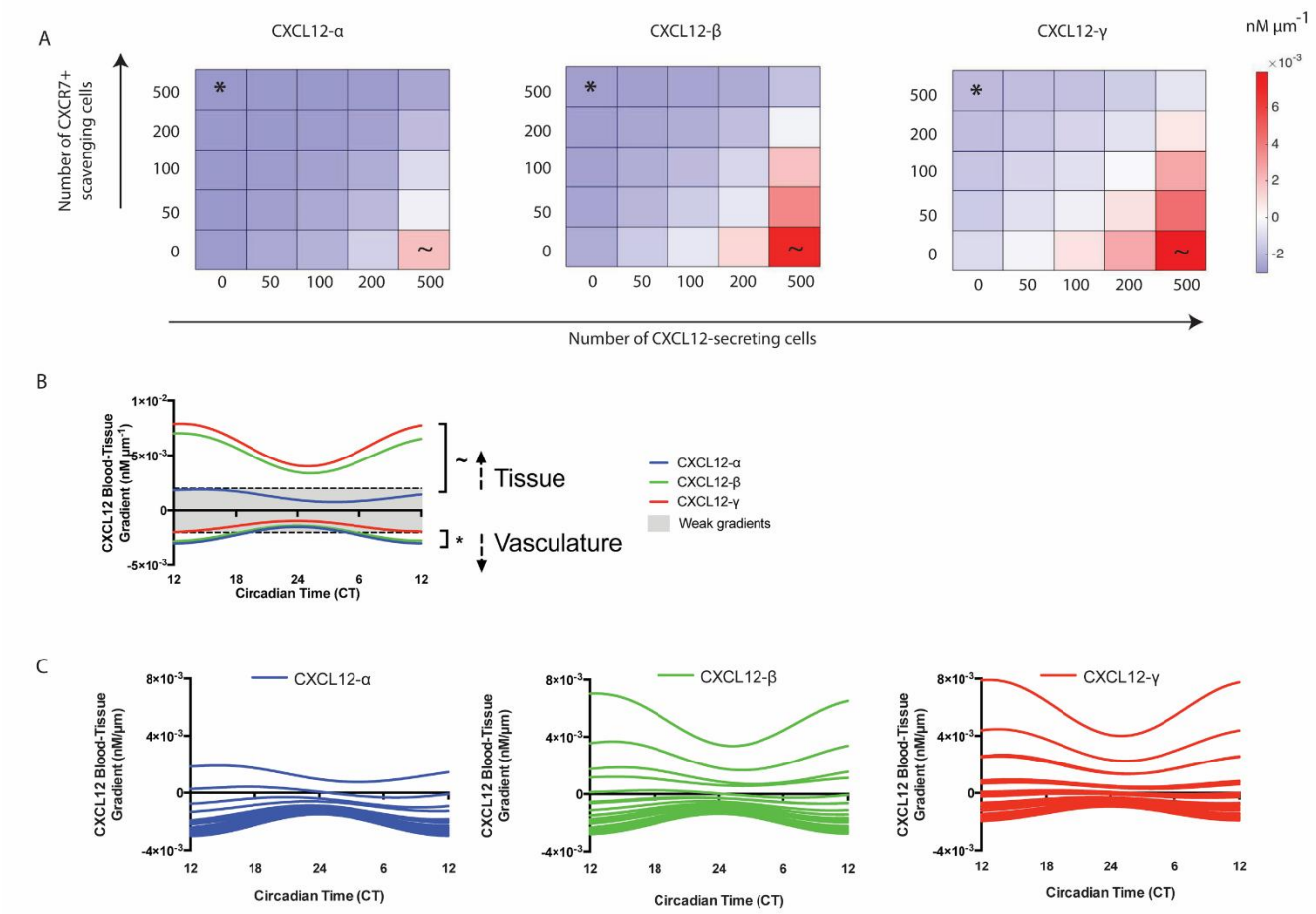

Figure 4.5 CXCL12-secreting and -scavenging cell numbers in the tumor microenvironment influence gradient direction and magnitude

(A) Maximum CXCL12-α (left), -β (center), and -γ (right) gradients over a 24-h period illustrate that gradients are dependent upon cellular makeup. The * and ~ show the strongest gradients into the blood and into the tissue, respectively, and correspond to the same symbols in B. Gradient magnitudes were averaged over 5 runs to account for potential variation in the randomization of cell placement in the model. In all simulations, 200 endothelial CXCR7+ cells were present. White squares designate a gradient of exactly 0. (B) Time-series of CXCL12 gradients demonstrate that gradients fluctuate according to circadian rhythm. Dotted lines represent the minimum gradient (0.002 nM/µm) that we determined to be necessary to trigger significant cell migration in a previous work (21). CT 24 corresponds to 9 pm while CT 12 corresponds to 9 am. Positive gradients correspond to higher CXCL12 tissue concentrations while negative gradients correspond to higher CXCL12 concentrations in the blood. C, Circadian fluctuations of all combinations of CXCL12-secreting and -scavenging cells shown in A.

To examine whether circadian fluctuations influence CXCL12 gradient magnitude and direction, we plot the 24-h time course (Figure 4.5B) of the simulations showing the

largest gradients (denoted by * and ~ in Figure 4.5A). We compare these gradients to those calculated in earlier work as likely to generate cell migration (22). At high CXCL12-secreting cell and low CXCR7+ cell numbers (denoted by ~), CXCL12-β and -γ force strong gradients away from the vasculature and into the tissue at all times of day. Substantial CXCL12-α gradients never form with the same tumor cellular composition. These results are in agreement with the data presented in Figure 4.2, which suggest that isoforms with higher ECM binding affinity form stronger cell-derived gradients. In contrast, when the CXCL12-secreting cell numbers are low and the CXCR7+ cell numbers are high (denoted by *), both CXCL12-α and -β gradients toward vasculature are predicted to be strong enough to elicit cell migration between about 3am and 3pm. CXCL12-γ gradients are minimal with this tumor cellular composition. Circadian fluctuations influenced gradient magnitudes but could not reverse the direction of the gradient, as shown by the lack of intersection of the curves with the x-axis. Additional simulations of combinations of secreting and scavenging cell numbers shown in Figure 4.5A similarly demonstrate that the circadian rhythm impacts gradient magnitude but not direction (Figure 4.5C). The amplitude of curves shown in Figure 4.5C decreases as the gradient magnitudes approaches 0, implying that weaker gradients vary less throughout the day than stronger ones (Figure C1). Although the circadian rhythm was unable to affect gradient direction, it is a critical regulator of the time-dependent gradient magnitude.

4.5 Discussion

Chemokine gradients may facilitate the migration of cancer cells from a primary tumor, a critical step in metastasis. In previous computational and experimental studies, we found that a CXCL12 gradient on the order of 0.002 nM/μm, which corresponds to a difference of 10-20 molecules across the cell diameter, may be large enough to drive cancer cell migration (37). Thus, a critical question is whether such gradients are likely to develop in tumors, and whether gradients point toward or away from the vasculature. Tumor spatial heterogeneity in the location and number of CXCR7+ cells as well as differences among CXCL12-α, -β, and -γ secretion rates and ECM binding may affect

the gradients. Here, we use a computational model to understand the generation of CXCL12 gradients and calculate both the magnitude and direction of those gradients in a tumor microenvironment over time.

We wondered whether circadian oscillations in CXCL12 levels, driven by periodic alterations in cellular secretion rates throughout the body and affecting blood concentrations, would generate gradients in tumor tissue. We hypothesized that perhaps the oscillations could even reverse the gradient direction in the tumor tissue, so the gradient could dynamically switch between being directed into the bulk tissue and directed into the vasculature over the course of 24 hours. However, we found that for a given tumor cellular composition, the gradient is unable to switch directions because the two competing sources of CXCL12, the blood and the secretion rate from cells in the tumor, vary in unison. As the blood level increases, the secretion rate in the tumor also increases, and the gradient does not reverse because both the blood and tissue are gaining CXCL12 simultaneously. Nevertheless, circadian fluctuations affect gradient magnitudes and are hence still important *in vivo*. In fact, circadian fluctuations may influence the dosing schedule of cancer therapeutics (38,39), especially those that target the CXCL12 gradient or signaling axis.

It is difficult to fathom how CXCL12 gradients can cause cancer cell migration into blood vessels because of the presence of endothelial CXCR7 on most tumor vasculature. Indeed, our simulations suggest that endothelial CXCR7 encourages the formation of gradients pointed into the tissue (Figure 4.4A,B). Yet, our work also predicts that tumor regions with low numbers of CXCL12-secreting cells and high numbers of CXCR7+ cells in the bulk tumor tissue, even in the presence of endothelial CXCR7+ cells, can allow the formation of gradients pointing into the vasculature. In these cases, a dominant source of chemokine is CXCL12 originating from distant sites in the body that is delivered to the tumor via the blood circulation. The notion that cancer cells within the tumor respond to gradients formed from chemokine delivered from outside the tumor as well as chemokine generated within the tumor has not been well studied. This potential mechanism for the formation of gradients directed into the vasculature is supported by a

statistical bioinformatics study of The Cancer Genome Atlas, which concluded that low CXCL12 levels in breast tumors correlated with more aggressive disease (20). Other recent work has shown that sustained CXCL12 expression in the primary tumor inhibits metastasis, and that elevated CXCR7 levels and lower CXCL12 expression were related to poor survival (40). Our data combined with these observations suggest that inhibiting CXCR7 may be crucial to preventing metastasis.

Our simulations show that endothelial and non-endothelial CXCR7+ cells both scavenge CXCL12 and thus regulate concentrations near and far from the blood vessel, respectively. In particular, endothelial CXCR7 is predicted to assist in maintaining CXCL12 gradients directed into the tissue (Figure 4.4). This is consistent with Stacer et al., who determined that endothelial CXCR7 is protective against metastasis (35). At the same time, our simulations suggest that non-endothelial CXCR7 levels also play an important role in gradient generation; as described earlier, high levels can result in gradients directed toward the vasculature. Additionally, CXCR7 plays a role in neo-angiogenesis (17,33,41). The multiple roles for CXCR7 should be considered when designing and administering inhibitors for this receptor.

Tumors are notoriously heterogeneous (42–44). There may exist “micro-regions” within a primary tumor that have a cellular composition that facilitates generation of strong gradients and therefore cell migration (Figure 4.6). Other areas of the same tumor without such conducive gradients would exhibit less cell migration (45). As depicted in Figure 4.5, CXCL12 gradients in the tumor microenvironment are isoform dependent; isoforms with higher ECM binding affinity more easily form gradients directed into the tissue, whereas isoforms with lower ECM binding affinity more easily form gradients directed toward the vasculature. We thus predict that cells located in the permissive “micro-regions” account for the most migratory cells in the tumor and should be targeted to reduce metastatic burden.

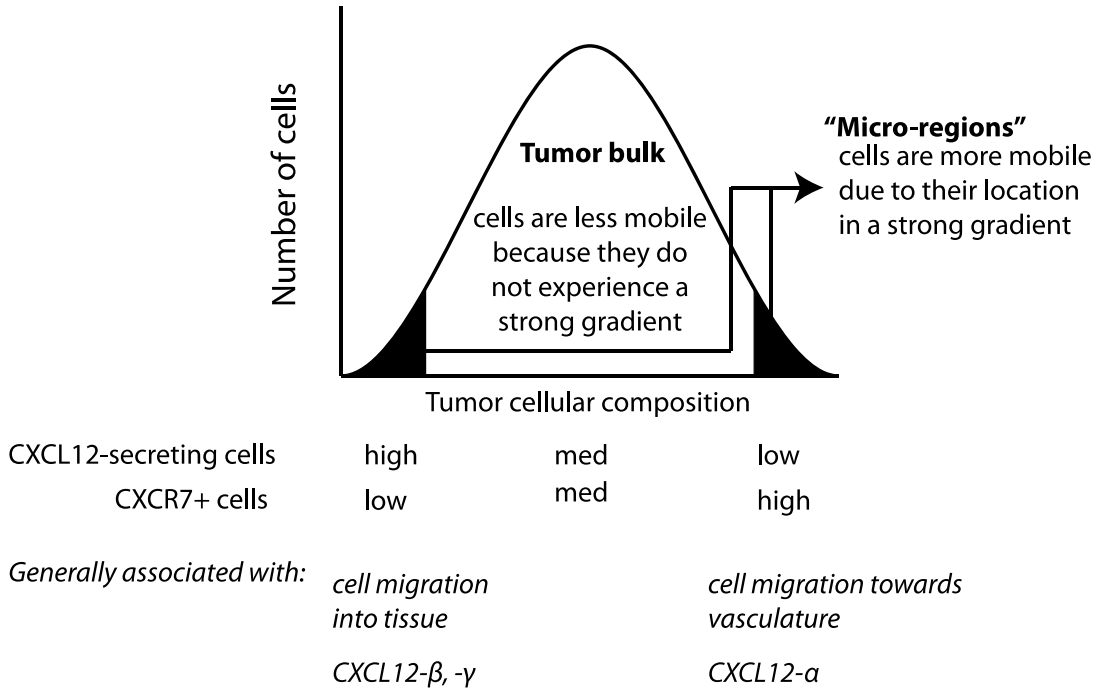

Figure 4.6 Cancer cells within "micro-regions" of the tumor containing either high or low ratios of CXCL12-secreting to non-endothelial CXCR7+ cells are more migratory than the tumor bulk

We assume tumors are mostly composed of immobile or weakly mobile cells due to a balance of CXCL12-secreting and CXCR7+ cells and a weak CXCL12 gradient. We predict that cancer cells located in environments containing a high number of CXCR7+ cells and few CXCL12-secreting cells will likely migrate towards vasculature, whereas cancer cells in environments with high secreting cell numbers and few CXCR7+ cells will likely migrate deeper into the tissue.

Although we and others have shown that cell-derived CXCL12-γ forms gradients of higher magnitude *in vitro* than the -α isoform due to its lower effective diffusivity (Figure 4.2D) (21,22,24), here we predict that CXCL12-α can form stronger gradients directed

toward the vasculature than the other isoforms *in vivo*. To explain this, consider a tumor region of high CXCR7+ cell and low CXCL12-secreting cell numbers. In this case, the blood is the dominant source of CXCL12, not cells in the tumor tissue. The blood concentration of CXCL12-α is noticeably higher than CXCL12-γ (Figure 4.3B). The high number of CXCR7+ cells in the tissue rapidly deplete CXCL12 regardless of isoform. Because the blood concentration of CXCL12-α is higher than CXCL12-γ and their tissue concentrations are nearly identical, the gradient directed into the vasculature is larger for CXCL12-α than -γ. This phenomenon is not seen in most *in vitro* chemotaxis studies because the specific *in vivo* setting, including the high ratio of scavenging to secreting cells, the large quantities of CXCL12 delivered from a separate source, and the relevant length scales, are necessary.

The predictions of our computational model suggest new *in vivo* experiments to study cancer cell migration and metastasis. We predict that mouse models containing tumors with CXCR4+ and CXCR7+ cells will cause more metastases than tumors containing only CXCR4+ cells (via analogy with Figure 4.6). As explained above, we also predict that CXCL12-α originating at distant sites far from the primary tumor will be better at forming gradients directed toward the vasculature than CXCL12-γ because of its higher blood concentration. By using our computational model to predict new experiments (46), we allow experimentalists to focus on studies with a high likelihood of revealing mechanisms of cancer cell migration and metastasis *in vivo*.

Our model predicts CXCL12 gradients *in vivo*, but has limitations. CXCL12 isoforms differ in their amino acid chain composition and length and therefore are likely differentially regulated by proteolytic degradation. When more quantitative information about the kinetics of these processes is available, the model can be used to assess any additional impact on CXCL12 gradients. In addition, CXCR4+ cells can influence the CXCL12 gradient, although minimally, and also signal differently through each isoform. Connell et. al found that CXCL12-γ binds sulfated tyrosine in N-terminus of CXCR4, which prevented CXCR4 activation (50). Isoform-specific signaling through CXCR4 likely has implications for cell migration, and should be incorporated in models which

include cell migration due to CXCL12 gradients.

As we learn more about the molecular-, cellular-, and tissue-scale mechanisms that drive the formation of CXCL12 gradients and presumably cancer metastasis, we will be more equipped to disrupt the process. The results of this study provide motivation that CXCL12 isoforms, the cellular composition of a tumor, and circadian rhythm fluctuations dynamically influence CXCL12 gradients. By providing an approach to define and analyze spatial and temporal dynamics of CXCL12 in tumors, we anticipate this research will help successfully advance CXCR7-targeted therapies into clinical oncology.

4.6 References

1. Sun X, Cheng G, Hao M, Zheng J, Zhou X, Zhang J, et al. CXCL12/CXCR4/CXCR7 chemokine axis and cancer progression. Cancer Metastasis Rev. 2010;29(4):709–722. doi:10.1007/s10555-010-9256-x.
2. Sun Y, Mao X, Fan C, Liu C, Guo A, Guan S, et al. CXCL12-CXCR4 axis promotes the natural selection of breast cancer cell metastasis. Tumor Biol. 2014;35:7765–7773. doi:10.1007/s13277-014-1816-1.
3. Müller A, Homey B, Soto H, Ge N, Catron D, Buchanan ME, et al. Involvement of chemokine receptors in breast cancer metastasis. Nature. 2001;410(6824):50–56. doi:10.1038/35065016.
4. Munson JM, Bellamkonda R V, Swartz MA. Interstitial Flow in a 3D Microenvironment Increases Glioma Invasion by a CXCR4-Dependent Mechanism. Cancer Res. 2013;73(5):1536–47.
5. Teicher BA, Fricker SP. CXCL12 (SDF-1)/CXCR4 Pathway in Cancer. Clin Cancer Res. 2010;16(11):2927–2931. doi:10.1158/1078-0432.CCR-09-2329.
6. Feig C, Jones JO, Kraman M, Wells RJB, Deonarine A, Chan DS, et al. Targeting CXCL12 from FAP-expressing carcinoma- associated fibroblasts synergizes with anti – PD-L1 immunotherapy in pancreatic cancer. Proc Natl Acad Sci. 2013;110(50):20212–20217. doi:10.1073/pnas.1320318110.
7. Taromi S, Kayser G, Catusse J, Elverfeldt D von, Reichardt W, Braun F, et al. CXCR4 antagonists suppress small cell lung cancer progression. Oncotarget. 2016;7(51):85185-85195. doi:10.18632/oncotarget.13238.
8. Liao Y, Fu Z, Zhou C, Shan L, Wang Z, Yin F, et al. AMD3100 reduces CXCR4-mediated survival and metastasis of osteosarcoma by inhibiting JNK and Akt, but not p38 or Erk1/2, pathways in in vitro and mouse experiments. Oncol Rep. 2015;34(1):33–42. doi:10.3892/or.2015.3992.
9. Sun X, Charbonneau C, Wei L, Yang W, Chen Q, Terek RM. CXCR4-Targeted Therapy Inhibits VEGF Expression and Chondrosarcoma Angiogenesis and Metastasis. Mol Cancer Ther. 2013;12(7):1163-1170. doi:10.1158/1535-7163.MCT-12-1092.
10. Horuk R. Chemokine receptors. Cytokine Growth Factor Rev. 2001;12:313–35.
11. Weitzenfeld P, Ben-baruch A. The chemokine system, and its CCR5 and CXCR4 receptors, as potential targets for personalized therapy in cancer. Cancer Lett. 2014;352(1):36–53. doi:10.1016/j.canlet.2013.10.006.
12. Luker KE, Steele JM, Mihalko LA, Ray P, Luker GD. Constitutive and Chemokine-dependent Internalization and Recycling of CXCR7 in Breast Cancer Cells to Degrade Chemokine Ligands. Oncogene. 2010;29(32):4599–4610. doi:10.1038/onc.2010.212.
13. Choi YH, Burdick MD, Strieter BA, Mehrad B, Strieter RM. CXCR4, but not CXCR7, discriminates metastatic behavior in non-small cell lung cancer cells. Mol Cancer Res. 2014;12(1):38–47. doi:10.1158/1541-7786.MCR-12-0334.
14. Luker KE, Lewin SA, Mihalko LA, Schmidt BT, Winkler JS, Coggins NL, et al. Scavenging of CXCL12 by CXCR7 promotes tumor growth and metastasis of CXCR4-positive breast cancer cells. Oncogene. 2012;31(45):4750–4758. doi:10.1038/onc.2011.633.

15. Costello CM, Mccullagh B, Howell K, Sands M, Belperio JA, Keane MP, et al. A role for the CXCL12 receptor, CXCR7, in the pathogenesis of human pulmonary vascular disease. Eur Respir J. 2012;39(6):1415–1424. doi:10.1183/09031936.00044911.
16. Tachibana K, Hirota S, Iizasa H, Yoshida H, Kawabata K, Kataoka Y, et al. The chemokine receptor CXCR4 is essential for vascularization of the gastrointestinal tract. Nature. 1998;393:591-594. doi:10.1038/31261.
17. Burns JM, Summers BC, Wang Y, Melikian A, Berahovich R, Miao Z, et al. A novel chemokine receptor for SDF-1 and I-TAC involved in cell survival, cell adhesion, and tumor development. J Exp Med. 2006;203(9):2201–2213. doi:10.1084/jem.20052144.
18. Berahovich RD, Zabel BA, Lewen S, Walters MJ, Wang Y, Jaen JC, et al. Endothelial expression of CXCR7 and the regulation of systemic CXCL12 levels. Immunology. 2014;141(1):111–122. doi:10.1111/imm.12176.
19. Yu L, Cecil J, Peng SB, Schrementi J, Kovacevic S, Paul D, et al. Identification and expression of novel isoforms of human stromal cell-derived factor 1. Gene. 2006;374:174–179. doi:10.1016/j.gene.2006.02.001.
20. Zhao S, Chang SL, Linderman JJ, Feng FY, Luker GD. A Comprehensive Analysis of CXCL12 Isoforms in Breast Cancer. Translational Oncology. 2014;7(3):429–348. doi:10.1016/j.tranon.2014.04.001.
21. Laguri C, Sadir R, Rueda P, Baleux F, Gans P, Arenzana-Seisdedos F, et al. The novel CXCL12gamma isoform encodes an unstructured cationic domain which regulates bioactivity and interaction with both glycosaminoglycans and CXCR4. PLoS One. 2007;2(10):e1110. doi:10.1371/journal.pone.0001110.
22. Chang SL, Cavnar SP, Takayama S, Luker GD, Linderman JJ. Cell, Isoform, and Environment Factors Shape Gradients and Modulate Chemotaxis. PLoS One. 2015;10(4):e0123450. doi:10.1371/journal.pone.0123450
23. Hoogewerf AJ, Kuschert GS, Proudfoot AE, Borlat F, Clark-Lewis I, Power CA et al. Glycosaminoglycans mediate cell surface oligomerization of chemokines. Biochemistry. 1997;36(44):13570–13578.
24. Cavnar SP, Ray P, Moudgil P, Chang SL, Luker KE, Linderman JJ, et al. Microfluidic source-sink model reveals effects of biophysically distinct CXCL12 isoforms in breast cancer chemotaxis. Integr Biol (Camb). 2014;6(5):564–576. doi:10.1039/c4ib00015c.
25. Méndez-Ferrer S, Lucas D, Battista M, Frenette PS. Haematopoietic stem cell release is regulated by circadian oscillations. Nature. 2008;452(7186):442-447. doi:10.1038/nature06685.
26. Ella K, Csépányi-Kömi R, Káldi K. Circadian regulation of human peripheral neutrophils. Brain Behav Immun. 2016;57:209–221. doi:10.1016/j.bbi.2016.04.016.
27. Department of Health and Human Services. National Institutes of Health. 2017. Available from: https://grants.nih.gov/grants/guide/rfa-files/RFA-CA-17-017.html.
28. Barakat H, Clark J. On the Solution of the Diffusion Equations by Numerical Methods. J. Heat Transfer. 1966;88(4):421–427. doi:10.1115/1.3691590.
29. Cilfone NA, Kirschner DE, Linderman JJ. Strategies for Efficient Numerical Implementation of Hybrid Multi-scale Agent-Based Models to Describe Biological

Systems. Cel. Mol. Bioeng. 2015;8:119–136. doi:10.1007/s12195-014-0363-6.
30. Coggins NL, Trakimas D, Chang SL, Ehrlich A, Ray P, Luker KE, et al. CXCR7 Controls Competition for Recruitment of β-Arrestin 2 in Cells Expressing Both CXCR4 and CXCR7. PLoS One. 2014;9(6):e98328. doi:10.1371/journal.pone.0098328.
31. Costantini S, Raucci R, De Vero T, Castello G, Colonna G. Common structural interactions between the receptors CXCR3, CXCR4 and CXCR7 complexed with their natural ligands, CXCL11 and CXCL12, by a modeling approach. Cytokine. 2013;64(1):316–321. doi:10.1016/j.cyto.2013.05.024.
32. Zhu B, Xu D, Deng X, Chen Q, Huang Y, Peng H, et al. CXCL12 Enhances Human Neural Progenitor Cell Survival Through a CXCR7- and CXCR4-Mediated Endocytotic Signaling Pathway. Stem Cells. 2012;30(11):2571–2583. doi:10.1002/stem.1239.
33. Hattermann K, Held-Feindt J, Lucius R, Müerköster SS, Penfold ME, Schall TJ, et al. The Chemokine Receptor CXCR7 Is Highly Expressed in Human Glioma Cells and Mediates Antiapoptotic Effects. Cancer Res. 2010;70(8):3299–3308. doi:10.1158/0008-5472.CAN-09-3642.
34. Hartmann TN, Grabovsky V, Pasvolsky R, Shulman Z, Buss EC, Spiegel A, et al. A crosstalk between intracellular CXCR7 and CXCR4 involved in rapid CXCL12-triggered integrin activation but not in chemokine-triggered motility of human T lymphocytes and CD34+ cells. J Leukoc Biol. 2008;84(4):1130–1140. doi:10.1189/jlb.0208088.
35. Stacer AC, Fenner J, Cavnar SP, Xiao A, Zhao S, Chang SL, et al. Endothelial CXCR7 regulates breast cancer metastasis. Oncogene. 2015;35(13):1716-1724. doi:10.1038/onc.2015.236.
36. Łukaszewicz-Zając M, Mroczko B, Kozłowski M, Szmitkowski M. The Serum Concentrations of Chemokine CXCL12 and Its Specific Receptor CXCR4 in Patients with Esophageal Cancer. Dis Markers. 2016;2016:7963895. doi:10.1155/2016/7963895.
37. Kim BJ, Hannanta-anan P, Chau M, Kim YS, Swartz MA, Wu M. Cooperative Roles of SDF-1α and EGF Gradients on Tumor Cell Migration Revealed by a Robust 3D Microfluidic Model. PLoS One. 2013;8(7):e68422. doi:10.1371/journal.pone.0068422.
38. Savvidis C, Koutsilieris M. Circadian Rhythm Disruption in Cancer Biology. Mol Med. 2012;18:1249–1260. doi:10.2119/molmed.2012.00077.
39. Lévi F, Focan C, Karaboué A, de la Valette V, Focan-Henrard D, Baron B, et al. Implications of circadian clocks for the rhythmic delivery of cancer therapeutics. Adv Drug Deliv Rev. 2007;59(9-10):1015–1035. doi:10.1016/j.addr.2006.11.001.
40. Yu PF, Huang Y, Xu CL, Lin LY, Han YY, Sun WH, et al. Downregulation of CXCL12 in mesenchymal stromal cells by TGFβ promotes breast cancer metastasis. Oncogene. 2017;36(6):840–849. doi:10.1038/onc.2016.252.
41. Maishi N, Ohga N, Hida Y, Akiyama K, Kitayama K, Osawa T, et al. CXCR7 : A novel tumor endothelial marker in renal cell carcinoma. Pathol Int. 2012;62(5):309–317. doi:10.1111/j.1440-1827.2012.02792.x.
42. Hanahan D, Weinberg RA. Hallmarks of Cancer: The Next Generation. Cell. 2011;144(5):646–674. doi:10.1016/j.cell.2011.02.013.

43. Keller PJ, Lin AF, Arendt LM, Klebba I, Jones AD, Rudnick JA, et al. Mapping the cellular and molecular heterogeneity of normal and malignant breast tissues and cultured cell lines. Breast Cancer Res. 2010;12(5):R87. doi:10.1186/bcr2755.
44. Campbell JJ, Husmann A, Hume RD, Watson CJ, Cameron RE. Development of three-dimensional collagen scaffolds with controlled architecture for cell migration studies using breast cancer cell lines. Biomaterials. 2017;114:34–43. doi:10.1016/j.biomaterials.2016.10.048.
45. Clark AG, Vignjevic DM. Modes of cancer cell invasion and the role of the microenvironment. Curr Opin Cell Biol. 2015;36:13–22. doi:10.1016/j.ceb.2015.06.004.
46. Bielekova B, Vodovotz Y, An G, Hallenbeck J. How implementation of systems biology into clinical trials accelerates understanding of diseases. Front Neurol. 2014;5(June):1–9.
47. Zervantonakis IK, Hughes-Alford SK, Charest JL, Condeelis JS, Gertler FB, Kamm RD. Three-dimensional microfluidic model for tumor cell intravasation and endothelial barrier function. Proc Natl Acad Sci. 2012;109(34):13515–13520. doi:10.1073/pnas.1210182109.
48. Lin F, Butcher EC. T cell chemotaxis in a simple microfluidic device. Lab Chip. 2006;6(11):1462–1469. doi:10.1039/b607071j.
49. Torisawa YS, Mosadegh B, Bersano-Begey T, Steele JM, Luker KE, Luker GD, et al. Microfluidic platform for chemotaxis in gradients formed by CXCL12 source-sink cells. Integr Biol (Camb). 2010;2(11-12):680–686. doi:10.1039/c0ib00041h.
50. Connell BJ, Sadir R, Baleux F, Laguri C, Kleman J, Luo L et al. Heparan sulfate differentially controls CXCL12α- and CXCL12γ-mediated cell migration through differential presentation to their receptor CXCR4. Sci Signal. 2016;9(452):ra107. doi:10.1126/scisignal.aaf1839.

Chapter 5 Conclusions

5.1 Summary of research findings

Cancer heterogeneity is arguably the major reason for the failure of cancer treatment today (1,2). The failure of both chemotherapeutic agents and targeted therapies is due to subpopulations of cells that are functionally distinct from the bulk of the tumor and drive progression of the disease. A better understanding of the mechanisms that drive cells to behave differently can inform the design of therapies which effectively target these subpopulations.

5.1.1 Cellular environment informs heterogeneous cell signaling outcomes

We hypothesize that signaling heterogeneity is generated from variable pre-existing cell states, described by extrinsic noise in key signaling molecules, and these signaling states are in constant flux in response to the intracellular and extracellular environment. We postulate this because cells must survive in spatiotemporally varying environments and are constantly being exposed to new stimuli (3). Cells *in vivo* can be subjected to various environmental or intracellular conditions such as pH, oxygen, growth factors, attachment stimuli, mutations, cell cycle cues, or energy levels (4–6). These stimuli have implications for downstream signaling to inform the cell when the timing is right to perform a task, such as migrate, divide, die, or become senescent. Our goal was to build a computational model that allows these environmental conditions to shape cell signaling through extrinsic noise in key signaling molecules.

We used the ERK and Akt signaling pathways in breast cancer cells to couple KTR experiments with a computational framework for understanding cell signaling heterogeneity. Not all seemingly-fit cells will respond to a ligand stimulus even in the most apt signaling conditions. We postulate that inhibitory mechanisms downstream of

the receptor-ligand interaction can restrain or completely prevent signaling, and the restraint mechanism is stronger in some cells than others due to their pre-existing state. ERK and Akt are activated downstream of both CXCR4, a G-protein coupled receptor implicated in cancer growth and metastasis (7,8), and epidermal growth factor receptor (EGFR), a receptor tyrosine kinase implicated in overactive cell proliferation (9,10). Our model predicted the paired ERK and Akt signaling behavior at various doses of the ligands for CXCR4 and EGFR (CXCL12 and EGF, respectively) in various breast cancer cell types. Our approach allows the interpretation of a continuum of cell signaling responses with the origin of heterogeneity stemming from not only mathematical inference, but also biological insights.

5.1.2 Method for explaining signaling heterogeneity

Our approach to understanding signaling heterogeneity is distinct from the common approach. The common approach involves estimating baseline parameters from data or literature, varying these parameters +/- a certain percentage of their baseline value, running the model for each parameter set, and analyzing the model outputs, such as dynamic signaling behaviors. For example, many studies incorporate extrinsic noise in their computational models by varying some or all parameters by a log-normal distribution, which allows a wide range of parameters to be sampled (11–13). This approach is useful in that it can enable the prediction of single-cell and population-scale signaling behaviors. However, how do these extrinsic noise parameters change as the environment of cells changes, as is the case in the tumor microenvironment? Our approach provides a framework for allowing single cells to adapt to changes in environment and thus subsequently edit signaling behaviors.

Our method, similar to the common approach, begins by using a baseline parameter set to describe the cell population. This parameter set accurately describes the behavior of the most common single-cell response within a population. However, to generate heterogeneity, we vary only specific parameters which set the pre-existing cell state. After running the model with all of these pre-existing cell state parameter sets and simulating a ligand dose, we compare model-predicted signaling behaviors with

experimental signaling behaviors to determine the pre-existing cell states of individual cells in experiments. Because the pre-existing state is necessarily independent of ligand and dose used to stimulate the cells, we can use the pre-existing state to predict responses in new contexts, such as different ligand doses.

5.1.3 Generating a heterogeneous signaling landscape

In our computational model, not only is it necessary to capture the heterogeneity seen in experiments based on pre-existing cell states, but the model must provide a framework which allows for editing of these states based on environmental cues. There is a rich ERK and Akt signaling literature, such that we were able to compile a reasonable mechanistic reaction scheme of both pathways (14–19). We built a system of ODEs connecting receptor-ligand interactions (both CXCR4-CXCL12 and EGFR-EGF) to downstream signaling effectors ERK and Akt, and then connected these activities to the kinetics of the ERK and Akt KTRs, such that our model predicts the exact same quantity as our experiments: the cytoplasmic to nuclear ratio of intensities of the KTRs. Our KTR experimental data indicated that in a population of MDA-MB-231 breast cancer cells, the entire range of ERK and Akt signaling possibilities could be explained by variation in three key signaling molecules: phosphatidylinositol-3-kinase (PI3K), Ras, and mammalian target of rapamycin complex 1 (mTORC1). PI3K and Ras are upstream activators of Akt and ERK, respectively. mTORC1 is a downstream negative regulator of both pathways. We chose to add extrinsic noise to these three components specifically because they are known to vary from cell-to-cell with environmental cues such as available mitogens, confluency, and metabolism. We employed extrinsic noise on these components in the signaling pathway by adding a first-order rate constant which converts the inactive form to the active form of these three signaling molecules in the absence of stimulating ligand (CXCL12 or EGF). These extrinsic noise parameters set the pre-existing cell state, which varies from cell-to-cell, and the pre-existing state deterministically controls ERK and Akt signaling.

In order for our model to capture both the signaling heterogeneity as well as the potential for editing of the pre-existing state, we simulate a library of possible responses

to a ligand stimulus by varying the PI3K, Ras, and mTORC1 extrinsic noise parameters combinatorically. For each of these three parameters, we vary the values from low to high, such that the active form of the given species prior to ligand stimulation covers the range of values from near zero to the maximum active concentration. The maximum active concentration is set by the initial condition for that species in the model, which would indicate that it exists entirely in the active form. By running the computational model at all combinations of these three extrinsic noise parameters, while holding the other rate parameters constant, we generate over 12,000 simulated ERK and Akt responses to a ligand stimulus as a function of the pre-existing cell state. We refer to the collection of the 12,000 simulated responses as the *model library*. The model library, when organized into a three-dimensional map by the pre-existing state which generates each single-cell output, is called the *signaling landscape*.

5.1.4 Modeling predicts the pre-existing state of cells in experiments

The model-predicted signaling landscape can be compared to single-cell KTR data to bin cells into pre-existing states that most closely match their signaling behaviors. We combined the predicted signaling landscape with single-cell KTR experimental data in breast cancer cells for ERK and Akt activity following CXCR4 or EGFR stimuli. Each KTR experiment and subsequent image analysis provides us with ~ 300-500 experimental cells, each containing a time-lapse of ERK and Akt activity following a ligand stimulus. We perform a least-square match between the ERK and Akt responses of each experimental cell and the responses of all predicted cells and organize these fitness scores into a fitness matrix. The fitness matrix shows how well each experimental cell response matched predicted cell responses. The pre-existing state of any given experimental cell is the pre-existing state of the predicted cell response from the signaling landscape to which the fitness score is the smallest. Once we have assigned the pre-existing state to cells, we can ask questions about the mechanisms that drive them to occupy that particular state and how we can control heterogeneity.

5.1.5 Cellular memory tunes CXCR4 signaling responses

In Chapter 2, we built a computational model of heterogeneous CXCR4-mediated signaling to Akt and ERK based on variable pre-existing cell states. Compared to control, when cells were stimulated with either fetal bovine serum (FBS) or epidermal growth factor (EGF) 4 hours before CXCL12, they demonstrated increased responsiveness to the CXCL12 stimulation. The model depicted that this increased responsiveness was due to a shift in cell states following FBS or EGF stimulation that shaped subsequent CXCR4-mediated signaling. The model was able to predict CXCR4 signaling responses in three breast cancer cell lines which contained activating mutations in the ERK pathway, Akt pathway, or both. The model also correctly predicted that clinically relevant kinase inhibitors trametinib, a MEK inhibitor, and ridaforolimus, an mTORC1 inhibitor, would potentiate pro-metastatic signaling in subsets of cells. This work demonstrated that cells hold a memory of previous signaling inputs and adapt to dynamic changes in environmental conditions by modifying subsequent signaling responses.

5.1.6 Pre-existing cell states explain heterogeneous signaling through EGFR and CXCR4

In Chapter 3, we expand upon the computational model from Chapter 2 by incorporating EGFR dynamics to test our model hypothesis on a new receptor system relevant to cancer. Our hypothesis that the entire range of signaling behaviors in Akt and ERK could be explained by variable pre-existing cell states, set by extrinsic noise in three pathway components, held true for EGFR as well as CXCR4 signaling. We tested the model on a range of doses of both EGF and CXCL12 in multiple breast cancer cell types, and model predictions matched experimental data. We used the model to predict that therapies targeting phosphatidylinositol-3-kinase (PI3K) would inadvertently increase the basal signaling level as well as responsiveness of ERK signaling to EGFR stimulation in a subset of SUM 159 breast cancer cells. By testing our core hypothesis on another receptor system, we add strength to the argument that signaling heterogeneity arises from deterministic, not stochastic, noise.

5.1.7 Isoforms, circadian rhythms, and tumor cellular composition control CXCL12 gradient direction and magnitude

In Chapter 4, we build a cellular-scale computational model to simulate the magnitude and direction of CXCL12 gradients in a primary tumor environment based on multiple known mechanisms of CXCL12 transport. The isoform-specific properties, such as the extracellular matrix (ECM) binding affinity and secretion rates from cells, edit the shape of CXCL12 gradients *in vivo*. Our findings indicate that CXCL12-β and CXCL12-γ form stronger gradients and confer larger overall CXCL12 concentrations despite being secreted slower than CXCL12-α. The circadian regulation of CXCL12 alters the magnitude of gradients formed by CXCL12 between the tissue and the vasculature. However, the direction of the gradient cannot easily flip because the time scale of diffusion is rapid with respect to the time scale of the circadian clock, forcing the gradient direction to remain steady in a given tumor cellular composition. However, heterogeneity in the spatial composition of the tumor can influence both gradient direction and magnitude. Primary tumors with high numbers of CXCR7-positive cells and very few CXCL12-secreting cells form environments with low levels of CXCL12 deep within tissue which can be supplied CXCL12 by diffusion from the blood. This scenario generates a region of a tumor conducive for CXCR4-positive cells to directionally migrate toward a blood vessel and metastasize. This work highlights how possibly a majority of the primary tumor is not prone to initiate metastasis, and just small regions of primary tumors, which are comprised of specific ratios of fibroblasts to CXCR7-positive cells, can act as sinks for cancer cells to metastasize. We postulate that CXCR7 may be an optimal target for prevention of cancer metastasis.

5.2 Future directions

5.2.1 Exact sources of signaling heterogeneity remain unclear

While our computational model in Chapters 2 and 3 captures the range of signaling behaviors in the population of breast cancer cells, we lump the many physiological sources of the heterogeneity into three extrinsic noise parameters that describe the pre-existing cell state. These physiological sources may include pH, confluency,

metabolism, or availability of mitogens, among others. The next step to uncovering how the environment shapes signaling responses is to tease apart the contributions from all of these potential sources to examine how they affect signaling individually. For example, we can couple information from metabolic imaging (20), that indicates the extent to which single cells are undergoing glycolysis versus oxidative phosphorylation, with KTR data to understand how the metabolic state regulates cell signaling. Deciphering how cells shape signaling behavior based on environmental stimuli can expose new treatment opportunities to abrogate oncogenic signaling in cancer cells.

5.2.2 Integration of ERK and Akt with other signaling networks

ERK and Akt are two well-studied kinases known to promote cancer phenotypes. Both the ERK and Akt signaling networks are known to communicate with a variety of other networks as well. For example, studies suggest that p38, a kinase implicated in the cell stress response, is negatively regulated by ERK (21). Evidence suggests that Akt contains crosstalk regulation with the NOTCH signaling pathway (22). The ability of intracellular kinases to be phosphorylated on multiple sites, and have differing roles based on which sites are phosphorylated, dramatically increases the functionality of a single kinase (23) and highlights how crosstalk mechanisms can add dimensionality to cell signaling responses.

5.2.3 Cell signaling is flexible, not hard-wired

Cell signaling diagrams are often depicted as arrows pointing from one kinase to the next to illustrate the cascade of phosphorylation reactions that activate downstream effectors. These diagrams may underplay the complexity of cell signaling by incorrectly implying that all cells within a population will respond to a stimulus by a hard-wired pathway. Just because a cell responded in one way to a stimulus does not mean it would always respond that way. We show how cell signaling networks retain connectivity from cell to cell, but heterogeneous signaling responses to a stimulus exist even in the most ideal, homogeneous conditions. We posit that cell signaling is a plastic, flexible, tunable process, and cell responses are dictated by the pre-existing

state which is constantly shifting to encode new information about the dynamic microenvironment. Future work should include experiments that more closely examine the mechanisms by which certain environmental conditions promote or inhibit signaling responses. For example, how do single cell signaling responses change when moving from 2D to 3D settings, such as in a spheroid or *in vivo* in a tumor? How does the availability of other nutrients, besides the growth factors we used in this thesis (fetal bovine serum and epidermal growth factor), affect signaling? By further examining how cell signaling processes are tunable rather than hard-wired, we learn how to better design targeted therapies in the context of cellular environment.

5.2.4 Cell signaling heterogeneity is extraordinarily robust

In our experiments, we found that signaling heterogeneity was robust because it existed in every experiment. The variability in pre-existing states in a given cell population was similarly robust, and we find the same pre-existing states by matching experimental data to predicted responses under various ligand and dosing conditions. We found no treatments on any breast cancer cell population that erased the heterogeneity of their pre-existing states. The robustness of the heterogeneity of cell signaling within a population suggests that cells work to actively maintain this heterogeneity, perhaps by communicating with extracellular vesicles (24). However, we are still left with the question: why does signaling heterogeneity exist? One interpretation of signaling heterogeneity is that it provides single cells with the ability to “hedge bets.” In this context, heterogeneity positions cells to respond differently to reduce risk of a bulk response to a noisy signal (12). Or, perhaps signaling heterogeneity provides diversity as a fitness advantage to the entire cell population such that the likelihood of some cells persevering through stressful conditions is higher (25). As we learn why cell signaling heterogeneity exists, we can begin to make better hypotheses about its true origins and exploit its tunability.

5.2.5 Leveraging cellular memory to tune signaling responses

We found that cell signaling responses are influenced by previous environmental cues, and this information is stored as memory inside the cell. While we showed that signaling is tunable because of this memory, further efforts to explore how we can minimize or erase signaling heterogeneity are warranted. For example, is there a treatment we can give cells *a priori*, be it a specific ligand or drug, which would predispose cells to die in the presence of a subsequent drug? Can we exploit the ability of cells to edit their states by administering treatments that decrease heterogeneity to prevent the emergence of Darwinian drug resistance? Recent work has uncovered how we can sync cell signaling patterns by providing pulsatile inputs, and cell responses were shaped by the rest period, frequency, and duration of the pulses. What if we could administer pulsatile inputs (26,27) to a tumor *in vivo* to sync up tumor cell signaling patterns, thereby shifting cell states to those in which a drug has maximal effect? This approach may diminish or erase signaling heterogeneity and decrease the probability of resistance to a drug. Once we have a fundamental understanding of how we can edit cell states to tune signaling responses, we can manipulate cell states such that targeted therapies have higher efficacy.

5.3 References

1. Rye I, Trinh A, Sætersdal A, Nebdal D, Lingjærde O, Almendro V, et al. Intratumor heterogeneity defines treatment-resistant HER2+breast tumors. Mol Oncol. 2018;12:1838–55.
2. Saunders NA, Simpson F, Thompson EW, Hill MM, Endo-Munoz L, Leggatt G, et al. Role of intratumoural heterogeneity in cancer drug resistance: Molecular and clinical perspectives. EMBO Mol Med. 2012;4:675–84.
3. Wang M, Zhao J, Zhang L, Wei F, Lian Y, Wu Y, et al. Role of tumor microenvironment in tumorigenesis. J Cancer. 2017;8:761–73.
4. Runa F, Hamalian S, Meade K, Shisgal P, Gray PC, Kelber JA. Tumor Microenvironment Heterogeneity: Challenges and Opportunities. Curr Mol Biol Reports. 2017;3:218–29.
5. Swietach P, Vaughan-Jones RD, Harris AL, Hulikova A. The chemistry, physiology and pathology of pH in cancer. Philos Trans R Soc L B Biol Sci. 2014;369(1638).
6. Sun XX, Yu Q. Intra-tumor heterogeneity of cancer cells and its implications for cancer treatment. Acta Pharmacol Sin. 2015;36:1219–27.
7. Hinton C V, Avraham S, Avraham HK. Role of the CXCR4/CXCL12 signaling axis in breast cancer metastasis to the brain. Clin Exp Metastasis. 2010;27(2):97–105.
8. Busillo JM, Benovic JL. Regulation of CXCR4 signaling. Biochim Biophys Acta - Biomembr. 2007;1768(4):952–63.
9. Sigismund S, Avanzato D, Lanzetti L. Emerging functions of the EGFR in cancer. Mol Oncol. 2018;12(1):3–20.
10. Sasaki T, Hiroki K, Yamashita Y. The role of epidermal growth factor receptor in cancer metastasis and microenvironment. Biomed Res Int. 2013;3.
11. Iwamoto K, Shindo Y, Takahashi K. Modeling Cellular Noise Underlying Heterogeneous Cell Responses in the Epidermal Growth Factor Signaling Pathway. PLoS Comput Biol. 2016;12(11):1–18.
12. Filippi S, Barnes CP, Kirk PDW, Kudo T, Kunida K, McMahon SS, et al. Robustness of MEK-ERK Dynamics and Origins of Cell-to-Cell Variability in MAPK Signaling. Cell Rep. 2016;15(11):2524–35.
13. Cheng Z, Taylor B, Ourthiague DR, Hoffmann A. Distinct single-cell signaling characteristics are conferred by the MyD88 and TRIF pathways during TLR4 activation. Sci Signal. 2015;8(385).
14. Tan WH, Popel AS, Mac Gabhann F. Computational Model of Gab1/2-Dependent VEGFR2 Pathway to Akt Activation. PLoS One. 2013;8(6):1–17.
15. Koh G, Fern H, Teong C, Hsu D, Thiagarajan PS. A decompositional approach to parameter estimation in pathway modeling: a case study of the Akt and MAPK pathways and their crosstalk. Bioinformatics. 2006;22(14):271–80.
16. Sedaghat AR, Sherman A, Quon MJ. A mathematical model of metabolic insulin signaling pathways. AmJPhysiol EndocrinolMetab. 2002;283(5):E1084–101.
17. Sonntag AG, Dalle Pezze P, Shanley DP, Thedieck K. A modelling-experimental approach reveals insulin receptor substrate (IRS)-dependent regulation of adenosine monosphosphate-dependent kinase (AMPK) by insulin. FEBS J. 2012;279(18):3314–28.

18. Fujita KA, Toyoshima Y, Uda S, Ozaki YI, Kubota H, Kuroda S. Decoupling of receptor and downstream signals in the Akt pathway by its low-pass filter characteristics. Sci Signal. 2010;3(132):1–11.
19. Rahman A, Haugh JM, Toker A. Kinetic Modeling and Analysis of the Akt/Mechanistic Target of Rapamycin Complex 1 (mTORC1) Signaling Axis Reveals Cooperative, Feedforward Regulation. J Biol Chem. 2017;292(7):2866–72.
20. Sanchez T, Zhang M, Needleman D, Seli E. Metabolic imaging via fluorescence lifetime imaging microscopy for egg and embryo assessment. Fertil Steril. 2018;111(2):212–8.
21. Xiao YQ, Malcolm K, Scott Worthen G, Gardai S, Schiemann WP, Fadok VA, et al. Cross-talk between ERK and p38 MAPK mediates selective suppression of pro-inflammatory cytokines by transforming growth factor-β. J Biol Chem. 2002;277(17):14884–93.
22. Cornejo MG, Mabialah V, Sykes SM, Khandan T, Lo Celso C, Lopez CK, et al. Crosstalk between NOTCH and AKT signaling during murine megakaryocyte lineage specification. Blood. 2011;118(5):1264–73.
23. Nishi H, Demir E, Panchenko AR. Crosstalk between signaling pathways provided by single and multiple protein phosphorylation sites. Vol. 427, Journal of Molecular Biology. 2015. p. 511–20.
24. Xu R, Rai A, Chen M, Suwakulsiri W, Greening DW, Simpson RJ. Extracellular vesicles in cancer — implications for future improvements in cancer care. Nat Rev Clin Oncol. 2018;15:617–38.
25. Levy SF. Cellular Heterogeneity: Benefits Besides Bet-Hedging. Vol. 26, Current Biology. 2016. p. R355–7.
26. Sumit M, Takayama S, Linderman JJ. New insights into mammalian signaling pathways using microfluidic pulsatile inputs and mathematical modeling. Integr Biol. 2017;9(1):6–21.
27. Sumit M, Neubig RR, Takayama S, Linderman JJ. Band-pass processing in a GPCR signaling pathway selects for NFAT transcription factor activation. Integr Biol. 2015;7:1378–86.

Appendices

Appendix A Supporting Information for Chapter 2

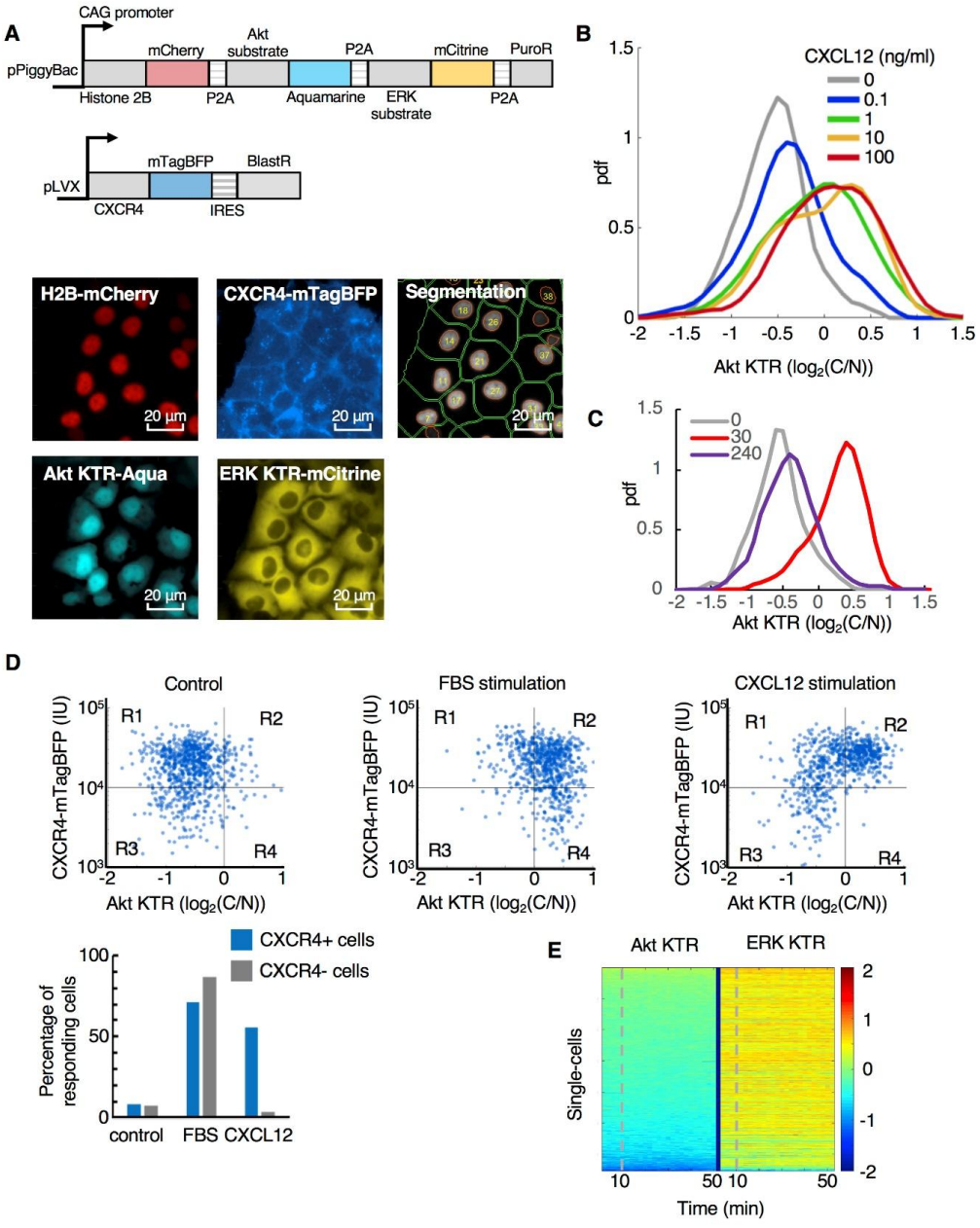

Figure A1 KTRs report concentration- and time-dependent CXCR4 signaling in response to FBS

(A) Reporter constructs for KTRs and histone 2B-mCherry nuclear marker in transposon vector and lentiviral vector with CXCR4-mTag blue fluorescent protein (BFP). Images show fluorescence channels in unstimulated MDA-MB-231 cells and representative watershed segmentation of cells. (B) CXCR4 signaling to Akt represented as probability density functions (pdf) of the distribution of Akt KTR values in CXCR4+ MDA-MB-231 cells after treatment for 30 minutes. All experiments included 300-500 cells for each group. No further increase in activation was seen above 10 ng/ml CXCL12. (C) Graph shows pdf of Akt KTR values for 300-500 cells for each group at the specified times in minutes after FBS treatment. (D) Scatter plots show distribution of Akt KTR values compared to CXCR4-BFP fluorescence intensity for single-cells under control conditioning and after incubation for 30 minutes with 10% FBS or 10 ng/ml CXCL12. (E) Akt or ERK signaling in MDA-MB-231 cells (N=631 cells) lacking CXCR4-mTagBFP and stimulated with CXCL12 at the 10 min timepoint.

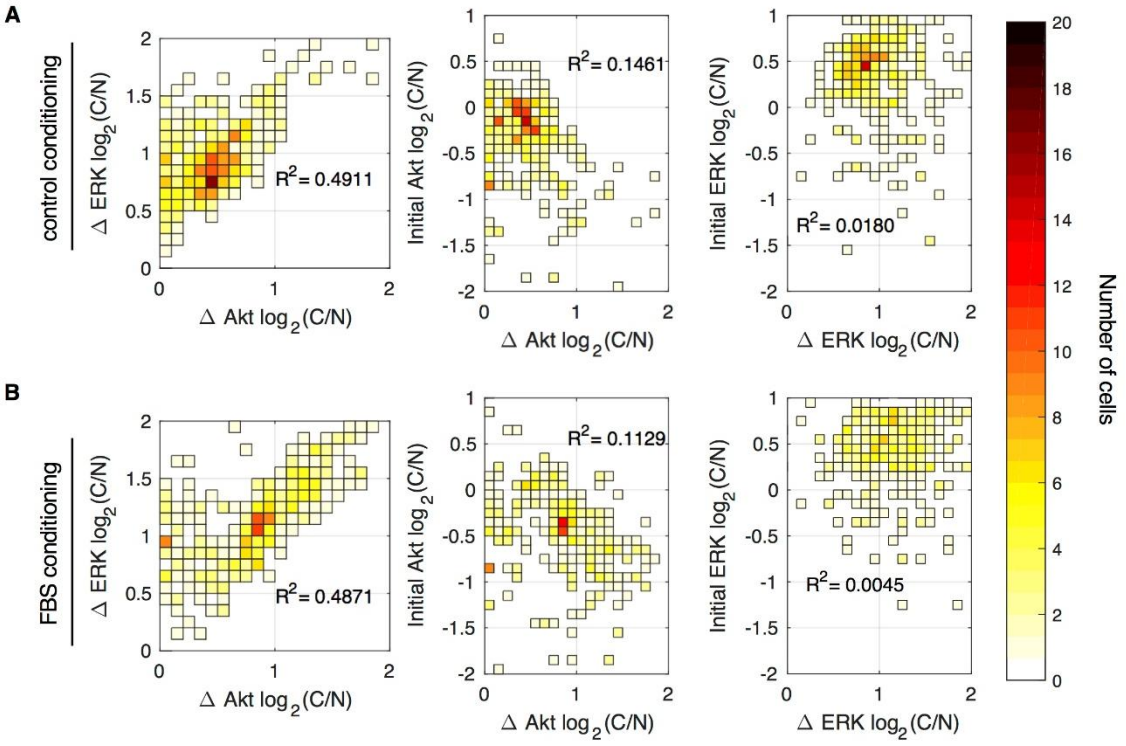

C

Observations from single-cell data	Relevance to the computational model
Basal signaling state and responsiveness are uncorrelated in Akt or ERK	Basal signaling state and responsiveness are regulated by separate species
Basal signaling states in Akt and ERK are heterogeneous among the cell population	Upstream activators of Akt and ERK are variable
Responsiveness in Akt and ERK are heterogeneous among the cell population	Regulators of Akt and ERK are variable
Akt and ERK responsiveness is correlated	Coordinate regulation of Akt and ERK by the same species

Figure A2 There is a trend between Akt responsiveness and ERK responsiveness, but initial Akt and ERK activity is poorly correlated with responsiveness in each respective kinase

(A) Akt and ERK responses to CXCR4 signaling with control conditioning (left panels). Initial levels of Akt (middle panels) and ERK (right panels) activities are also shown. (B) Akt and ERK responses to CXCR4 signaling with prior conditioning with FBS (right panels). Akt (middle panels) and ERK (right panels) activities are also shown. (C) Table relating observations from single-cell data to the computational model.

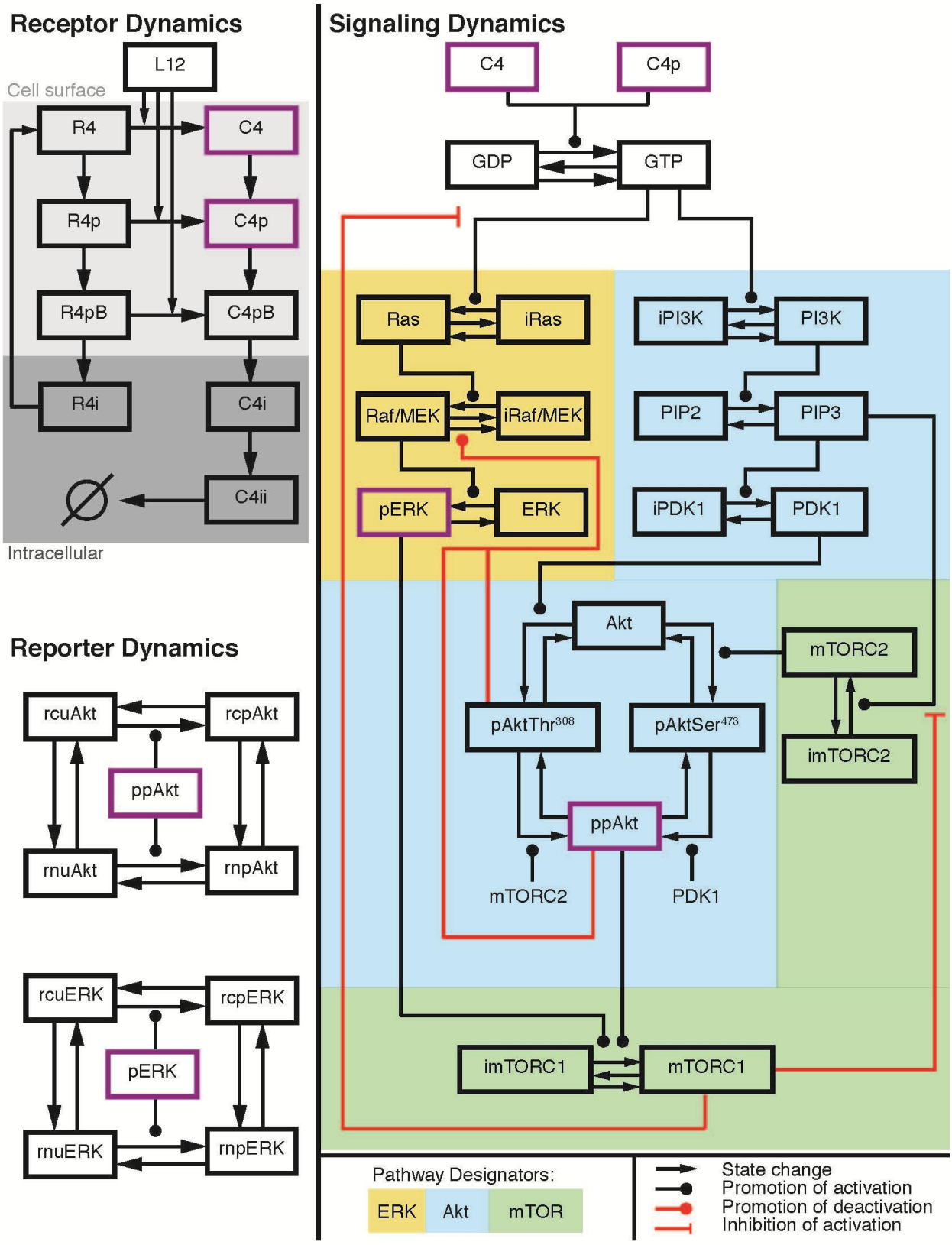
Receptor Dynamics
L12
Cell surface
R4
C4
R4p
C4p
R4pB
C4pB
R4i
C4i
C4ii
Intracellular
Reporter Dynamics
rcuAkt
rcpAkt
ppAkt
rnuAkt
rnpAkt
rcuERK
rcpERK
pERK
rnuERK
rnpERK
Signaling Dynamics
C4
C4p
GDP
GTP
Ras
iRas
iPI3K
PI3K
Raf/MEK
iRaf/MEK
PIP2
PIP3
pERK
ERK
iPDK1
PDK1
Akt
mTORC2
pAktThr308
pAktSer473
imTORC2
ppAkt
mTORC2
PDK1
imTORC1
mTORC1
Pathway Designators:
ERK
Akt
mTOR
State change
Promotion of activation
Promotion of deactivation
Inhibition of activation

Figure A3 CSM for CXCR4 signaling to ERK and Akt. The ordinary differential equation model consists of three modules that connect receptor, signaling, and reporter dynamics

Species outlined in purple link two modules. CXCR4 at the cell surface exists as unphosphorylated, phosphorylated, or phosphorylated and bound to β-arrestin. These three species can bind CXCL12. After binding CXCL12, these complexes internalize and are degraded, leading to a net decrease in available CXCR4 over time. The two complexes of CXCL12-CXCR4 not bound by β-arrestin can signal to G-proteins. G-proteins have a rate of basal activation in the absence of CXCR4 activation. G-proteins stimulate Ras and PI3K, which function as upstream activators of ERK and Akt, respectively. Ras promotes Raf/MEK scaffolding to activate ERK. PI3K converts phosphatidylinositol 4,5-bisphosphate (PIP_2) to phosphatidylinositol 3,4,5-triphosphate (PIP_3) at the cell surface. PIP3 drives activation of PDK1 and mTORC2, which subsequently activate Akt by phosphorylating Thr^{308} and Ser^{473}, respectively. A crosstalk mechanism allows Akt to deactivate the Raf/MEK complex. Activated ERK and Akt both promote the activation of mTORC1. mTORC1 acts as a restraint mechanism by inhibiting the activation of Ras and mTORC2. PI3K, Ras, and mTORC1 all have extrinsic noise that controls their activation in the absence of CXCR4-mediated signaling. KTRs for ERK and Akt follow the same mechanism and act independently. Without phosphorylation of a consensus motif, the reporter predominantly localizes to the nucleus. Activated kinase phosphorylates the reporter, causing translocation to the cytoplasm. KTRs provide a graded measure of kinase activity based on ratios of fluorescence in nucleus versus cytoplasm of individual cells.

$$\frac{d[PI3K]}{dt} = \frac{k_{G,actPI3K}[GTP][iPI3K]}{K_{M,actPI3K} + [iPI3K]} - k_{deactPI3K}[PI3K] + k_{PI3K}[iPI3K]$$

$$\frac{d[Ras]}{dt} = \frac{k_{G,actRas}[GTP][iRas]}{K_{M,actRas} + [iRas]\left(1 + \frac{[mTORC1]}{K_{I,inhibRas}}\right)} - k_{deactRas}[Ras] + k_{Ras}[iRas]$$

$$\frac{d[mTORC1]}{dt} = \frac{k_{ERK,actmTORC1}[pERK][imTORC1]}{K_{M,actmTORC1} + [imTORC1]} + \frac{k_{Akt,actmTORC1}[ppAkt][imTORC1]}{K_{M,actmTORC1} + [imTORC1]} - k_{deactmTORC1}[mTORC1] + k_{mTORC1}[imTORC1]$$

Conditional terms

Figure A4 Differential equations for the three species containing extrinsic noise terms in the computational model

In the CSM, PI3K, Ras, and mTORC1 contain terms driven by condition (conditional terms). Condition encompasses any driving force outside the scope of CXCR4 signaling, such as activation by mutation, metabolic state, confluency of cells, or other unknown forces. The conditional term carries the same form in all three species: a rate constant multiplied by the concentration of inactive species.

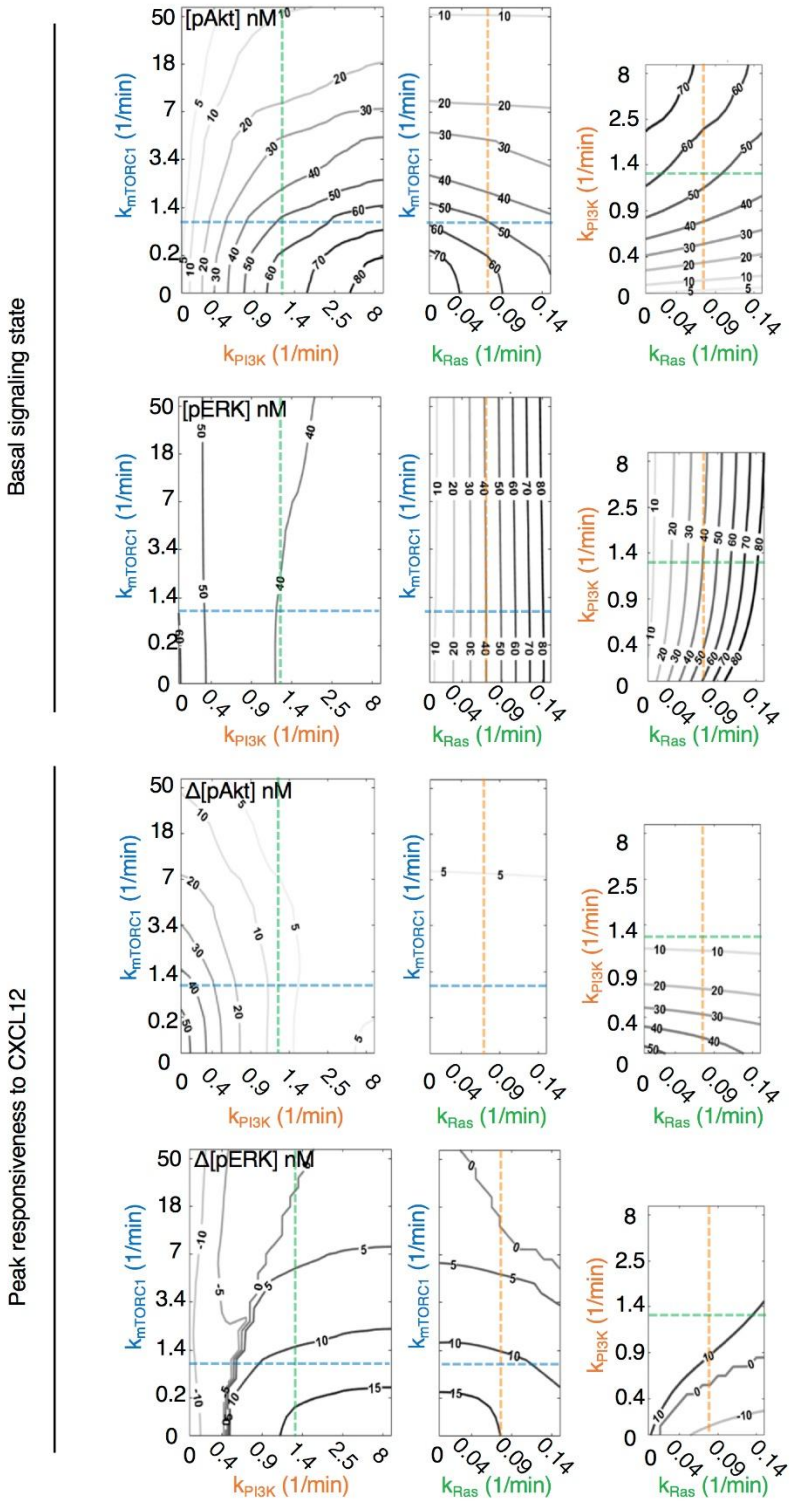
Basal signaling state
Peak responsiveness to CXCL12
[pAkt] nM
[pERK] nM
Δ[pAkt] nM
Δ[pERK] nM
k_mTORC1 (1/min)
k_PI3K (1/min)
k_Ras (1/min)
50
18
7
3.4
1.4
0.2
0
0.4
0.9
2.5
8
0.04
0.09
0.14
2.5

Figure A5 Extrinsic noise parameters for PI3K, Ras, and mTORC1 produce a highly differentiated signaling landscape of basal activity and CXCR4 responsiveness to ERK and Akt

Detail of 2D slices of the CSM for MDA-MB-231 cells shows the concentration (nM) of active Akt (pAkt) and active ERK (pERK). Time 0 (upper panels) shows basal equilibrium state of cells, whereas lower panels display the peak responsiveness through CXCR4 (either positive or negative change) upon CXCL12 stimulation.

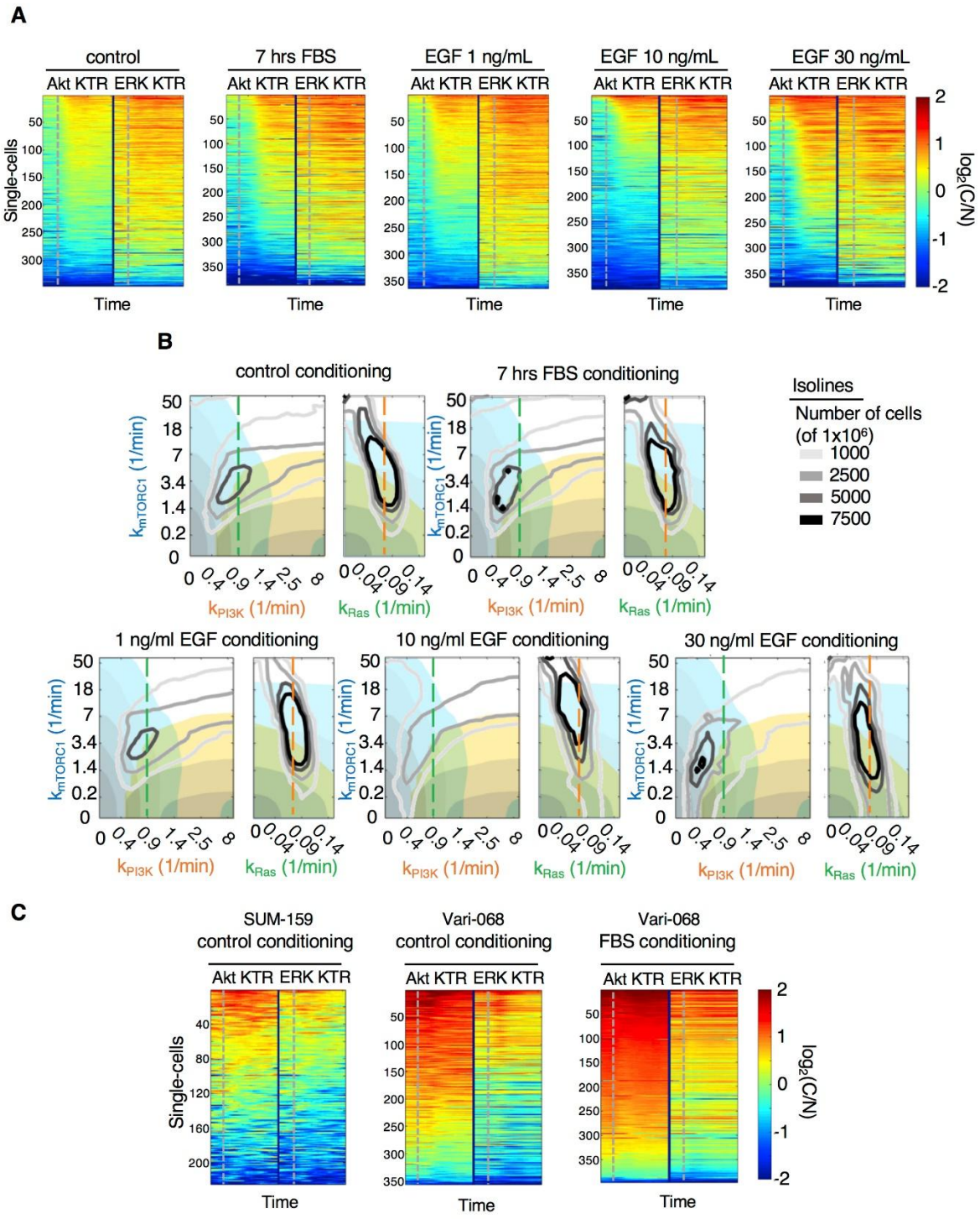
A
control
7 hrs FBS
EGF 1 ng/mL
EGF 10 ng/mL
EGF 30 ng/mL
Akt KTR ERK KTR
Single-cells
Time
log2(C/N)
B
control conditioning
7 hrs FBS conditioning
1 ng/ml EGF conditioning
10 ng/ml EGF conditioning
30 ng/ml EGF conditioning
Isolines
Number of cells
(of 1x10⁶)
1000
2500
5000
7500
kmTORC1 (1/min)
kPI3K (1/min)
kRas (1/min)
C
SUM-159
control conditioning
Vari-068
control conditioning
Vari-068
FBS conditioning
Akt KTR ERK KTR
Single-cells
Time
log2(C/N)

Figure A6 Conditional states of cells shift in the context of different conditioning times, stimuli, and genetic mutations

(A) Akt and ERK KTR responses in MDA-MB-231 CXCR4-mTagBFP cells conditioned with 7 hours of 10% FBS, 4 hours of listed concentrations of EGF, or control before imaging responses to 10 ng/ml CXCL12. Cells were imaged every 2 minutes for an hour with 4 images acquired before addition of 10 ng/ml CXCL12 (demarked by grey dashed line). The number of cells in each experiment is listed along the y-axes. (B) Occupancy maps, which illustrate probability of existing in conditional signaling states output from the CSM, for MDA-MB-231 cells shown in (A). (C) Akt and ERK KTR responses in control conditioned SUM-159 cells, control conditioned patient-derived Vari-068 cells, and Vari-068 cells conditioned with 10% FBS. The number of cells in each experiment is listed along the y-axes.

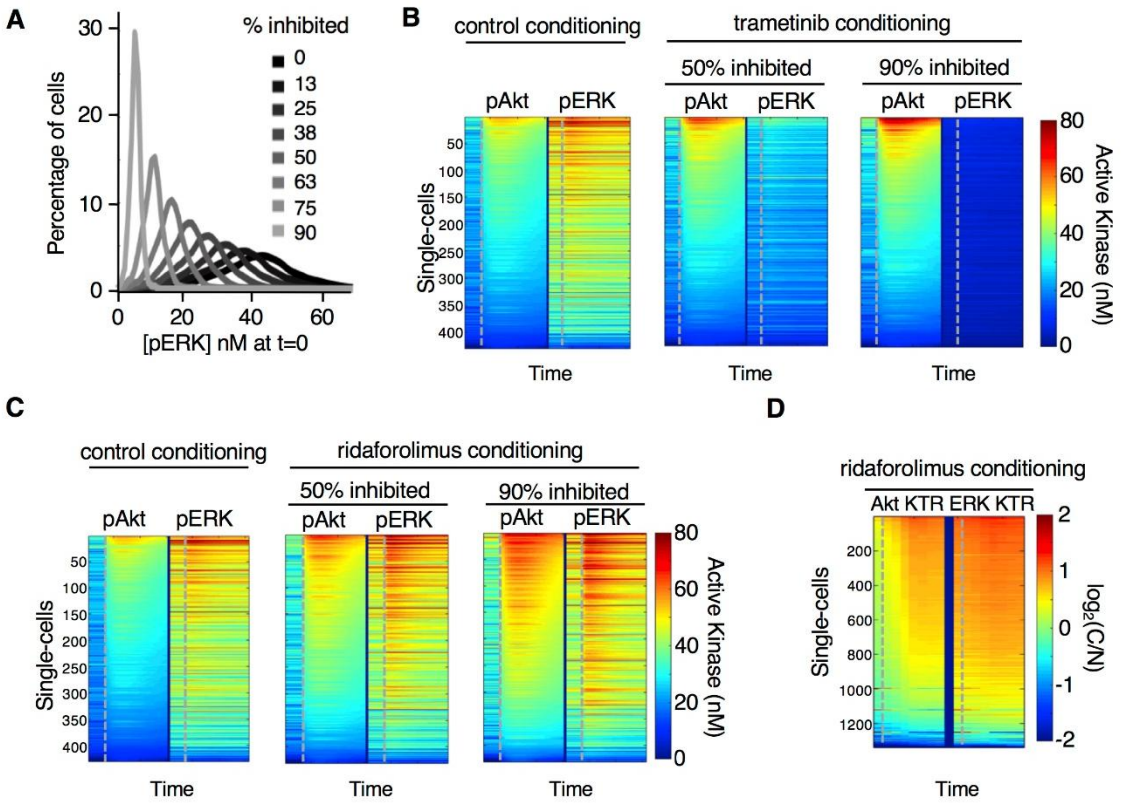
A
Percentage of cells
30
20
10
0
0
20
40
60
[pERK] nM at t=0
% inhibited
0
13
25
38
50
63
75
90
B
control conditioning
trametinib conditioning
50% inhibited
90% inhibited
pAkt
pERK
Single-cells
50
100
150
200
250
300
350
400
Time
80
60
40
20
0
Active Kinase (nM)
C
control conditioning
ridaforolimus conditioning
50% inhibited
90% inhibited
pAkt
pERK
Single-cells
Time
Active Kinase (nM)
D
ridaforolimus conditioning
Akt KTR ERK KTR
Single-cells
200
400
600
800
1000
1200
Time
2
1
0
-1
-2
log2(C/N)

Figure A7 Computational modeling of responses to the MEK inhibitor trametinib and the mTORC1 inhibitor ridaforolimus shows concentration-dependent, context-specific effects on the activation of Akt and ERK by CXCR4 in MDA-MB-231 cells

(A) Effect of the dose of simulated trametinib conditioning on distribution of active ERK at basal equilibrium in cells corresponding to the conditional signaling states when unconditioned. (B) CSM-predicted concentrations of active Akt and ERK upon CXCR4 stimulation in cells conditioned with trametinib doses that inhibit MEK activation of ERK by 0%, 50%, and 90%. The number of cells in each experiment is listed along the y-axes. (C) CSM-predicted concentrations of active Akt and ERK upon CXCR4 stimulation after conditioning with ridaforolimus when mTORC1 is 0%, 50%, and 90% inhibited. The number of cells in each experiment is listed along the y-axes. (D) Akt and ERK activity in MDA-MB-231 cells that received ridaforolimus for 4 hours before stimulation with CXCL12. Cells were imaged once before adding CXCL12, 2 minutes after adding CXCL12, and then every 8 minutes for an hour. The number of cells in each experiment is listed along the y-axes.

Table A1 CSM species descriptions and initial conditions

Species	Description	Initial Condition (nM)	Ref.
R4	Surface CXCR4	850	(1)
L12	Extracellular CXCL12	0	--
C4	Surface CXCL12-CXCR4 complex	0	--
R4p	Phosphorylated surface CXCR4	0	--
C4p	Phosphorylated surface CXCL12-CXCR4 complex	0	--
R4pB	Phosphorylated surface CXCR4 bound to β-arrestin	0	--
C4pB	Phosphorylated surface CXCL12-CXCR4 complex bound to β -arrestin	0	--
R4i	Internalized CXCR4	0	--
C4Bi	Internalized CXCL12-CXCR4 complex bound to B-arrestin	0	--
C4Bii	Internalized CXCL12-CXCR4 complex	0	--
GDP	Inactive G-protein	170	(2)
GTP	Active G-protein	0	--
iPI3K	Inactive PI3K	200	(3)
PI3K	Active PI3K	0	--
PIP_2	Phosphatidylinositol biphosphate (inactive)	1000	(4)
PIP_3	Phosphatidylinositol triphosphate (active)	0	--
iPDK1	Inactive PDK1	500	(5)
PDK1	Active PDK1	0	--
Akt	Inactive Akt	1000	(5)
$pAkt_{Thr}^{308}$	Akt phosphorylated only at the Threonine 308 site (kinase domain)	0	--
$pAkt_{Ser}^{473}$	Akt phosphorylated only at the Serine 473 site (regulatory domain)	0	--
ppAkt	Fully activated Akt phosphorylated at both the Thr^{308} and Ser^{473} site	0	--
imTORC1	Inactive mTORC1	800	(6)
mTORC1	Active mTORC1	0	--
imTORC2	Inactive mTORC2	800	(6)
mTORC2	Active mTORC2	0	--
iRas	Inactive Ras	3000	(5)
Ras	Active Ras	0	--
iRaf	Inactive Raf	1000	(5)
Raf	Active Raf	0	--
ERK	Inactive ERK	850	(7)
pERK	Active ERK	0	--
$r_{cu,Akt}$	Cytoplasmic unphosphorylated Akt KTR	0	(8)
$r_{nu,Akt}$	Nuclear unphosphorylated Akt KTR	200	(8)

$r_{cp,Akt}$	Cytoplasmic phosphorylated Akt KTR	200	(8)
$r_{np,Akt}$	Nuclear phosphorylated Akt KTR	0	(8)
$r_{cu,ERK}$	Cytoplasmic unphosphorylated ERK KTR	0	(8)
$r_{nu,ERK}$	Nuclear unphosphorylated ERK KTR	200	(8)
$r_{cp,ERK}$	Cytoplasmic phosphorylated ERK KTR	200	(8)
$r_{np,ERK}$	Nuclear phosphorylated ERK KTR	0	(8)

Table A2 CSM rate equations

Equation No.	Reaction reactant → product; modifiers	Reaction Rate
(1)	R4+L12↔C4	$v_{bLR4}=k_{f,L12,R4}*\left(R4*L12-K_{D,L12,R4}*C4\right)$
(2)	R4pB+L12↔C4pB	$v_{bLR4pB}=k_{f,L12,R4}*\left(R4pB*L12-K_{D,L12,R4pB}*C4pB\right)$
(3)	R4p+L12↔C4p	$v_{bLR4ph}=k_{f,L12,R4}*\left(R4p*L12-K_{D,L12,R4pB}*C4p\right)$
(4)	R4↔R4p	$v_{R4,phos}=k_{f,R4phos}*R4-k_{r,R4phos}*R4p$
(5)	C4↔C4p	$v_{C4phos}=k_{f,C4phos}*C4-k_{r,C4phos}*C4p$
(6)	R4p↔R4pB	$v_{bBR4ph}=k_{f,B,R4}*(R4p-K_{D,B,R4}*R4pB)$
(7)	C4p↔C4pB	$v_{bBC4ph}=k_{f,B,R4}*\left(C4p-K_{D,B,C4}*C4pB\right)$
(8)	C4pB→C4Bi	$v_{iC4pB}=k_{eC4pB}*C4pB$
(9)	C4Bi→C4Bii	$v_{off,C4Bi}=k_{off,B,R4}*C4Bi$
(10)	C4Bii→∅	$v_{deg,C4Bii}=k_{deg,C4Bii}*C4Bii$
(11)	R4pB→R4i	$v_{iR4pB}=k_{eR4pB}*R4pB$
(12)	R4i↔R4	$v_{recy,R4Bi}=k_{rec,R4Bi}*R4Bi$
(13)	GDP→GTP	$v_{actGC4}=k_{C4actG}*C4*GDP$
(14)	GDP→GTP	$v_{actGC4p}=k_{C4actG}*C4p*GDP$
(15)	GDP→GTP	$v_{actGC4p}=k_{basalActG}*GDP$
(16)	GTP→GDP	$v_{deactG}=k_{deactG\beta\gamma}*GTP$
(17)	iPI3K→PI3K; GTP	$v_{actPI3K}=k_{actPI3K}*GTP*\frac{iPI3K}{K_{M,actPI3K}+iPI3K}$
(18)	iPI3K→PI3K	$v_{extActPI3K}=k_{PI3K}*iPI3K$
(19)	PI3K→iPI3K	$v_{deactPI3K}=k_{deactPI3K}*PI3K$
(20)	PIP_2→PIP_3; PI3K	$v_{actPIP3}=k_{actPIP3}*PI3K*\frac{PIP_2}{K_{M,actPIP3}+PIP_2}$
(21)	PIP_3→PIP_2	$v_{deactPIP3}=k_{deactPIP3}*PIP_3$
(22)	iPDK1→PDK1; PIP_3	$v_{actPDK1}=k_{actPDK1}*PIP_3*\frac{iPDK1}{K_{M,actPDK1}+iPDK1}$
(23)	PDK1→iPDK1	$v_{deactPDK1}=k_{deactPDK1}*PDK1$

Equation No.	Reaction reactant → product; modifiers	Reaction Rate
(24)	$Akt \rightarrow pAkt_{T308}$; PDK1	$v_{Akt \rightarrow pAkt_{T308}} = k_{actAktT308} * PDK1 * \frac{Akt}{K_{M,actAktT308} + Akt}$
(25)	$pAkt_{S473} \rightarrow ppAkt$; PDK1	$v_{pAkt_{S473} \rightarrow ppAkt} = k_{actAktT308} * PDK1 * \frac{pAkt_{S473}}{K_{M,actAktT308} + pAkt_{S473}}$
(26)	$Akt \rightarrow pAkt_{S473}$; mTORC2	$v_{Akt \rightarrow pAkt_{S473}} = k_{actAktS473} * mTORC2 * \frac{Akt}{K_{M,actAktS473} + Akt}$
(27)	$pAkt_{T308} \rightarrow ppAkt$; mTORC2	$v_{pAkt_{T308} \rightarrow ppAkt} = k_{actAktS473} * mTORC2 * \frac{pAkt_{T308}}{K_{M,actAktS473} + pAkt_{T308}}$
(28)	$pAkt_{T308} \rightarrow Akt$	$v_{pAkt_{T308} \rightarrow Akt} = k_{deactAktT308} * pAkt_{T308}$
(29)	$pAkt_{S473} \rightarrow Akt$	$v_{pAkt_{S473} \rightarrow Akt} = k_{deactAktS473} * pAkt_{S473}$
(30)	$ppAkt \rightarrow pAkt_{T308}$	$v_{ppAkt \rightarrow pAkt_{T308}} = k_{deactAktS473} * ppAkt$
(31)	$ppAkt \rightarrow pAkt_{S473}$	$v_{ppAkt \rightarrow pAkt_{S473}} = k_{deactAktT308} * ppAkt$
(32)	imTORC2→mTORC2; PIP_3,mTORC1	$v_{actmTORC2} = k_{actmTORC2} * PIP_3 * \frac{imTORC2}{K_{M,actmTORC2} + imTORC2 \left(1 + \frac{mTORC1}{K_{I,mTORC1}}\right)}$
(33)	mTORC2→imTORC2	$v_{deactmTORC2} = k_{deactmTORC2} * mTORC2$
(34)	imTORC1→mTORC1	$v_{extActmTORC1} = k_{mTORC1} * imTORC1$
(35)	imTORC1→mTORC1; ppAkt	$v_{actmTORC1,Akt} = k_{actmTORC1,Akt} * ppAkt * \frac{imTORC1}{K_{M,actmTORC1,Akt} + imTORC1}$
(36)	imTORC1→mTORC1; pERK	$v_{actmTORC1,ERK} = k_{actmTORC1,ERK} * pERK * \frac{imTORC1}{K_{M,actmTORC1,ERK} + imTORC1}$
(37)	mTORC1→imTORC1	$v_{deactmTORC1} = k_{deactmTORC1} * mTORC1$
(38)	iRas→Ras; GTP, mTORC1	$v_{actRas} = k_{actRas} * GTP * \frac{iRas}{K_{M,actRas} + iRas \left(1 + \frac{mTORC1}{K_{I,Ras}}\right)}$
(39)	iRas→Ras	$v_{extActRas} = k_{Ras} * iRas$
(40)	Ras→iRas	$v_{deactRas} = k_{deactRas} * Ras$
(41)	iRaf→Raf; Ras	$v_{actRaf} = k_{actRaf} * Ras * \frac{iRaf}{K_{M,actRaf} + iRaf}$
(42)	iRaf→Raf	$v_{constActRaf} = k_{constActRaf} * iRaf$
(43)	Raf→iRaf; ppAkt	$v_{inhibRaf} = k_{inhibRaf} * ppAkt * \frac{Raf}{K_{M,inhibRaf} + Raf}$
(44)	Raf→iRaf	$v_{deactRaf} = k_{deactRaf} * Raf$

Equation No.	Reaction reactant → product; modifiers	Reaction Rate
(45)	ERK→pERK; Raf	$v_{actERK}=k_{actERK}*Raf*\frac{ERK}{K_{M,actERK}+ERK}$
(46)	pERK→ERK	$v_{deactERK}=k_{deactERK}*pERK$
(47)	$r_{cu,Akt}\rightarrow r_{cp,Akt}$; ppAkt	$v_{phos,cyto,AktKTR}=ppAkt*k_{cat}*\frac{r_{cu,Akt}}{r_{cu,Akt}+K_m}$
(48)	$r_{nu,Akt}\rightarrow r_{np,Akt}$; ppAkt	$v_{phos,nuc,AktKTR}=ppAkt*k_{cat}*\frac{r_{nu,Akt}}{r_{nu,Akt}+K_m}$
(49)	$r_{cu,ERK}\rightarrow r_{cp,ERK}$; pERK	$v_{phos,cyto,ERKKTR}=pERK*k_{cat}*\frac{r_{cu,ERK}}{r_{cu,ERK}+K_m}$
(50)	$r_{nu,ERK}\rightarrow r_{np,ERK}$; pERK	$v_{phos,nuc,ERKKTR}=pERK*k_{cat}*\frac{r_{nu,ERK}}{r_{nu,ERK}+K_m}$
(51)	$r_{cp,Akt}\rightarrow r_{cu,Akt}$	$v_{dephos,cyto,AktKTR}=k_{dc}*\frac{r_{cp,Akt}}{r_{cp,Akt}+K_{md}}$
(52)	$r_{np,Akt}\rightarrow r_{nu,Akt}$	$v_{dephos,nuc,AktKTR}=k_{dn}*\frac{r_{np,Akt}}{r_{np,Akt}+K_{md}}$
(53)	$r_{cp,ERK}\rightarrow r_{cu,ERK}$	$v_{dephos,cyto,ERKKTR}=k_{dc}*\frac{r_{cp,ERK}}{r_{cp,ERK}+K_{md}}$
(54)	$r_{np,ERK}\rightarrow r_{nu,ERK}$	$v_{dephos,nuc,ERKKTR}=k_{dn}*\frac{r_{np,ERK}}{r_{np,ERK}+K_{md}}$
(55)	$r_{cp,Akt}\rightarrow r_{np,Akt}$	$v_{phos,import,AktKTR}=k_{ip}*r_{cp,Akt}$
(56)	$r_{cu,Akt}\rightarrow r_{nu,Akt}$	$v_{unphos,import,AktKTR}=k_{iu}*r_{cu,Akt}$
(57)	$r_{np,Akt}\rightarrow r_{cp,Akt}$	$v_{phos,export,AktKTR}=k_{ep}*r_{np,Akt}$
(58)	$r_{nu,Akt}\rightarrow r_{cu,Akt}$	$v_{unphos,export,AktKTR}=k_{eu}*r_{nu,Akt}$
(59)	$r_{cp,ERK}\rightarrow r_{np,ERK}$	$v_{phos,import,ERKKTR}=k_{ip}*r_{cp,ERK}$
(60)	$r_{cu,ERK}\rightarrow r_{nu,ERK}$	$v_{unphos,import,ERKKTR}=k_{iu}*r_{cu,ERK}$
(61)	$r_{np,ERK}\rightarrow r_{cp,ERK}$	$v_{phos,export,ERKKTR}=k_{ep}*r_{np,ERK}$
(62)	$r_{nu,ERK}\rightarrow r_{cu,ERK}$	$v_{unphos,export,ERKKTR}=k_{eu}*r_{nu,ERK}$

Table A3 CSM differential equations

Receptor dynamics	$dR4/dt$	$= -v_{bLR4} - v_{R4,phos} + v_{recy,R4Bi}$
	$dC4/dt$	$= v_{bLR4} - v_{C4,phos}$
	$dR4p/dt$	$= v_{R4,phos} - v_{bLR4ph} - v_{bBR4ph}$
	$dC4p/dt$	$= v_{C4,phos} + v_{bLR4ph} - v_{bBC4ph}$
	$dL12/dt$	$= (-v_{bLR4} - v_{bLR4pB} - v_{bLR4ph} - v_{bLR4B}) * N_C/(V_{cell}/V_{media})$
	$dR4pB/dt$	$= -v_{bLR4pB} + v_{bBR4ph} - v_{iR4pB}$
	$dC4pB/dt$	$= v_{bLR4pB} + v_{bBC4ph} - v_{i,C4pB}$
	$dR4i/dt$	$= v_{iR4pB} - v_{recy,R4Bi}$
	$dC4Bi/dt$	$= v_{iC4pB} - v_{off,C4Bi}$
	$dC4Bii/dt$	$= v_{off,C4Bi} - v_{deg,C4Bii}$
Signaling dynamics	$dGTP/dt$	$= v_{actGC4} + v_{actGC4p} - v_{deactG}$
	$dPI3K/dt$	$= v_{actPI3K} + v_{basalActPI3K} - v_{deactPI3K}$
	$dPIP_3/dt$	$= v_{actPIP3} - v_{deactPIP3} - v_{actPDK1} + v_{deactPDK1}$
	$dPDK1/dt$	$= v_{actPDK1} - v_{deactPDK1}$
	$dmTORC1/dt$	$= v_{actmTORC1,Akt} + v_{actmTORC1,ERK} - v_{deactmTORC1}$
	$dmTORC2/dt$	$= v_{actmTORC2} - v_{deactmTORC2}$
	$dRas/dt$	$= v_{actRas} + v_{constActRas} - v_{inhibRas} - v_{deactRas}$
	$dRaf/dt$	$= v_{actRaf} + v_{constActRaf} - v_{inhibRaf} - v_{deactRaf}$
	$dpERK/dt$	$= v_{actERK} - v_{deactERK}$
	$dAkt/dt$	$= -v_{Akt\rightarrow pAktThr^{308}} - v_{Akt\rightarrow pAktSer^{473}} + v_{pAktThr^{308}\rightarrow Akt} + v_{pAktSer^{473}\rightarrow Akt}$
	$dpAkt_{Thr^{308}}/dt$	$= v_{Akt\rightarrow pAktThr^{308}} - v_{pAktThr^{308}\rightarrow Akt} - v_{pAktThr^{308}\rightarrow ppAkt} + v_{ppAkt\rightarrow pAktThr^{308}}$
	$dpAkt_{Ser^{473}}/dt$	$= -v_{pAktSer^{473}\rightarrow ppAkt} + v_{Akt\rightarrow pAktSer^{473}} + v_{ppAkt\rightarrow pAktSer^{473}} - v_{pAktSer^{473}\rightarrow Akt}$
	$dppAkt/dt$	$= v_{pAktSer^{473}\rightarrow ppAkt} + v_{pAktThr^{308}\rightarrow ppAkt} - v_{ppAkt\rightarrow pAktSer^{473}} - v_{ppAkt\rightarrow pAktThr^{308}}$
Reporter dynamics	$dr_{cu,Akt}/dt$	$= -v_{phos,cyto,Akt} + v_{dephos,cyto,Akt} - v_{unphos,import,Akt} + v_{unphos,export,Akt}$
	$dr_{nu,Akt}/dt$	$= -v_{phos,nuc,Akt} + v_{dephos,nuc,Akt} + k_v*(v_{unphos,import,Akt} - v_{unphos,export,Akt})$
	$dr_{cp,Akt}/dt$	$= v_{phos,cyto,Akt} - v_{dephos,cyto,Akt} - v_{phos,import,Akt} + v_{phos,export,Akt}$
	$dr_{np,Akt}/dt$	$= v_{phos,nuc,Akt} - v_{dephos,nuc,Akt} + k_v*(v_{phos,import,Akt} - v_{phos,export,Akt})$
	$dr_{cu,ERK}/dt$	$= -v_{phos,cyto,ERK} + v_{dephos,cyto,ERK} - v_{unphos,import,ERK} + v_{unphos,export,ERK}$
	$dr_{nu,ERK}/dt$	$= -v_{phos,nuc,ERK} + v_{dephos,nuc,ERK} + k_v*(v_{unphos,import,ERK} - v_{unphos,export,ERK})$
	$dr_{cp,ERK}/dt$	$= v_{phos,cyto,ERK} - v_{dephos,cyto,ERK} - v_{phos,import,ERK} + v_{phos,export,ERK}$
	$dr_{np,ERK}/dt$	$= v_{phos,nuc,ERK} - v_{dephos,nuc,ERK} + k_v*(v_{phos,import,ERK} - v_{phos,export,ERK})$

We assumed conservation of mass for all signaling reactions. The differential equation for the inactive form of each species in the signaling dynamics module is equal and opposite of the differential equation for the active form, ex: diPI3K/dt = -dPI3K/dt.

Table A4 CSM parameter values

Name	Description of event	Value	Unit	Ref
$k_{f,B,R4}$	β-arrestin binding to R4	2.04	$nM^{-1}\,min^{-1}$	(1,9,10)
$K_{D,B,R4}$	Dissociation of β-arrestin from R4	13.3	nM	(1,9,10)
$K_{D,B,C4}$	Dissociation of β-arrestin from C4	6.49×10^{-2}	nM	(1,9,10)
$k_{f,L12,R4}$	L12-R4 binding	8.79×10^{-2}	$nM^{-1}\,min^{-1}$	(1,9,10)
$K_{D,L12,R4}$	Dissociation of L12-R4	42.9	nM	(1,9,10)
$k_{e,R4pB}$	Endocytosis of phosphorylated R4	8.07×10^{-2}	min^{-1}	(1,9,10)
$k_{e,C4pB}$	Endocytosis of phosphorylated C4	0.169	min^{-1}	(1,9,10)
$k_{off,B,R4}$	β-arrestin removal from C4Bi	4.21×10^{-2}	min^{-1}	(1,9,10)
$k_{recy,R4Bi}$	Recycling of R4Bi to cell surface	3.64×10^{-3}	min^{-1}	(1,9,10)
$k_{deg,C4Bii}$	Degradation of internalized L12-C4 complex	9.15×10^{-3}	min^{-1}	(1,9,10)
$k_{f,C4phos}$	C4 phosphorylation	0.409	min^{-1}	(11)
$k_{f,R4phos}$	R4 phosphorylation	6.09×10^{-2}	min^{-1}	(11)
$k_{r,C4phos}$	C4 dephosphorylation	5.85×10^{-3}	min^{-1}	(11)
$k_{r,R4phos}$	R4 dephosphorylation	8.09×10^{-4}	min^{-1}	(11)
k_{C4actG}	GTP activation	0.200	$nM^{-1}\,min^{-1}$	(11)
$k_{basalActG}$	Basal GTP activation	0.200	min^{-1}	(11)
k_{deactG}	GTP deactivation	4.67	min^{-1}	(11)
$k_{actPI3K}$	PI3K activation	5.00	min^{-1}	(12,13)
$K_{M,actPI3K}$	PI3K activation (Michaelis constant)	20.00	nM	(13)
$k_{deactPI3K}$	PI3K deactivation	6.00	min^{-1}	(3,14)
k_{PI3K}	PI3K activity external to CXCR4 signaling	0.30 – 5.30	min^{-1}	--
$k_{actPIP3}$	PIP_3 activation	2.00×10^{2}	min^{-1}	(4,12,13)
$K_{M,actPIP3}$	PIP_3 activation (Michaelis constant)	1.00×10^{2}	nM	(13)
$k_{deactPIP3}$	PIP_3 deactivation	10.0	min^{-1}	(13)
$k_{actPDK1}$	PDK1 activation	50.0	min^{-1}	(13)
$K_{M,actPDK1}$	PDK1 activation (Michaelis constant)	2.00×10^{2}	nM	^
$k_{deactPDK1}$	PDK1 deactivation	53.3	min^{-1}	(13)
$k_{actAktThr}^{308}$	Akt Thr^{308} activation (kinase domain)	2.00	min^{-1}	(13)
$K_{M,actAktThr}^{308}$	Akt Thr^{308} (Michaelis constant)	2.00×10^{2}	nM	(6)
$k_{actAktSer}^{473}$	Akt Ser^{473} activation (regulatory	2.00	min^{-1}	(13,15)

	domain)			
$K_{M,actAktSer^{473}}$	Akt Ser^{473} (Michaelis constant)	2.00×10^2	nM	(6)
$k_{deactAktThr^{308}}$	Akt Thr^{308} deactivation	1.61	min^{-1}	(16,17)
$k_{deactAktSer^{473}}$	Akt Ser^{473} deactivation	3.00	min^{-1}	(16,17)
$k_{actmTORC1,ERK}$	mTORC1 activation by ERK	15.0	min^{-1}	(18)
$K_{M,actmTORC1,ERK}$	mTORC1 activation by ERK (Michaelis constant)	30.0	nM	(6)
$k_{actmTORC1,Akt}$	mTORC1 activation by Akt	5.00	min^{-1}	(6)
$K_{M,actmTORC1,Akt}$	mTORC1 activation by Akt (Michaelis constant)	30.0	nM	(6)
$k_{deactmTORC1}$	mTORC1 deactivation	22.5	min^{-1}	(19)
k_{mTORC1}	mTORC1 activity external to CXCR4 signaling	0 – 10.0	min^{-1}	--
$k_{actmTORC2}$	mTORC2 activation	0.100	min^{-1}	(15)
$K_{M,actmTORC2}$	mTORC2 activation (Michaelis constant)	10.0	nM	^
$K_{I,inhibmTORC2}$	mTORC2 inhibitory constant	50.0	nM	^
$k_{deactmTORC2}$	mTORC2 deactivation	0.197	min^{-1}	(15)
k_{actRas}	Ras activation	5.00	min^{-1}	(20)
$K_{M,actRas}$	Ras activation (Michaelis constant)	2.00×10^2	nM	(4)
k_{Ras}	Ras activity external to CXCR4 signaling	0 – 0.300	min^{-1}	--
$k_{deactRas}$	Ras deactivation	8.49	min^{-1}	(4)
$K_{I,inhibRas}$	Ras inhibitory constant	30.0	nM	^
k_{actRaf}	Raf activation	2.00	min^{-1}	(13)
$K_{M,actRaf}$	Raf activation (Michaelis constant)	1.00×10^3	nM	(4)
$k_{constActRaf}$	Raf constitutive activation due to mutation*	0.005	min^{-1}	^
$k_{inhibRaf}$	Raf inhibition	0.1	min^{-1}	(12)
$K_{M,inhibRaf}$	Raf inhibition (Michaelis constant)	50.0	nM	(12)
k_{actERK}	ERK activation	4.00	min^{-1}	(13)
$K_{M,actERK}$	ERK activation (Michaelis constant)	24.6	nM	(4)
$k_{deactERK}$	ERK deactivation	3.20	min^{-1}	(4)
k_{cat}	Reporter phosphorylation	20.0	min^{-1}	(8)
K_m	Reporter phosphorylation (Michaelis constant)	3.00×10^3	nM	(8)
k_{dc}	Reporter maximum dephosphorylation in cytoplasm	30.0	nM min^{-1}	(8)
K_{md}	Reporter dephosphorylation (Michaelis constant)	1.00×10^2	nM	(8)

k_{iu}	Unphosphorylated reporter import	0.3	min^{-1}	(8)
k_{eu}	Unphosphorylated reporter export	5.00×10^{-2}	min^{-1}	(8)
k_{dn}	Reporter maximum dephosphorylation in nucleus	30.0	nM min^{-1}	(8)
k_{ip}	Phosphorylated reporter import	5×10^{-2}	min^{-1}	(8)
k_{ep}	Phosphorylated reporter export	0.500	min^{-1}	(8)
k_v	Ratio of cytosolic volume to nuclear volume	4	unitless	(8)
N_C	Number of cells per imaging experiment	$2x10^5$	unitless	--

* For MDA-MB-231 cells. For SUM-159 and Vari-068 cells, this parameter is 0.
^ Estimated

We assumed that all biochemical reactions inside cells are governed by biophysical rate constants and do not vary from cell-to-cell, or from cell line to cell line. The only sources of variability in the CSM are the three external activation parameters for PI3K, Ras, and mTORC1, highlighted below. Parameters include rate constants, equilibrium dissociation constants, and Michaelis constants.

Table A5 CSM parameters for modeling kinase inhibition

Conditioning treatment	Altered Parameter(s)	Baseline	Inhibition value
trametinib (MEK inhibitor)	k_{actERK}	4.00 min^{-1}	2.00 min^{-1}
ridaforolimus (mTORC1 inhibitor)	$K_{I,inhibmTORC2}$ $K_{I,inhibRas}$	50 nM 30 nM	100 nM 60 nM

Appendix A References

1. Chang SL, Cavnar SP, Takayama S, Luker GD, Linderman JJ. Cell, Isoform, and Environment Factors Shape Gradients and Modulate Chemotaxis. PLoS One. 2015;10(4):e0123450.
2. Fallahi-Sichani M, Linderman JJ. Lipid raft-mediated regulation of G-protein coupled receptor signaling by ligands which influence receptor dimerization: A computational study. PLoS One. 2009;4(8).
3. Tan WH, Popel AS, Mac Gabhann F. Computational Model of Gab1/2-Dependent VEGFR2 Pathway to Akt Activation. PLoS One. 2013;8(6):1–17.
4. Jain P, Bhalla US. Signaling logic of activity-triggered dendritic protein synthesis: An mTOR gate but not a feedback switch. PLoS Comput Biol. 2009;5(2).
5. Adlung L, Kar S, Wagner M, She B, Chakraborty S, Bao J, et al. Protein abundance of AKT and ERK pathway components governs cell type- specific regulation of proliferation. Mol Syst Biol. 2017;13(1):904.
6. Borisov N, Aksamitiene E, Kiyatkin A, Legewie S, Berkhout J, Maiwald T, et al. Systems-level interactions between insulin-EGF networks amplify mitogenic signaling. Mol Syst Biol. 2009;5(256):1–15.
7. Iwamoto K, Shindo Y, Takahashi K. Modeling Cellular Noise Underlying Heterogeneous Cell Responses in the Epidermal Growth Factor Signaling Pathway. PLoS Comput Biol. 2016;12(11):1–18.
8. Regot S, Hughey JJ, Bajar BT, Carrasco S, Covert MW. High-sensitivity measurements of multiple kinase activities in live single cells. Cell. 2014;157(7):1724–34.
9. Coggins NL, Trakimas D, Chang SL, Ehrlich A, Ray P, Luker KE, et al. CXCR7 Controls Competition for Recruitment of β-Arrestin 2 in Cells Expressing Both CXCR4 and CXCR7. PLoS One. 2014;9(6):e98328.
10. Spinosa PC, Luker KE, Luker GD, Linderman JJ. The CXCL12/CXCR7 signaling axis, isoforms, circadian rhythms, and tumor cellular composition dictate gradients in tissue. PLoS One. 2017;12(11).
11. Chang SL. Mechanistic and statistical models to understand CXCL12/CXCR4/CXCR7 in breast cancer. 2015.
12. Hatakeyama M, Kimura S, Naka T, Kawasaki T, Yumoto N, Ichikawa M, et al. A computational model on the modulation of mitogen-activated protein kinase (MAPK) and Akt pathways in heregulin-induced ErbB signalling. Biochem J. 2003;373(2):451–63.
13. Koh G, Fern H, Teong C, Hsu D, Thiagarajan PS. A decompositional approach to parameter estimation in pathway modeling: a case study of the Akt and MAPK pathways and their crosstalk. Bioinformatics. 2006;22(14):271–80.
14. Sedaghat AR, Sherman A, Quon MJ. A mathematical model of metabolic insulin signaling pathways. AmJPhysiol EndocrinolMetab. 2002;283(5):E1084–101.
15. Sonntag A, Pezze Dalle P, Shanley DP TK. A modelling–experimental approach reveals insulinreceptor substrate (IRS)-dependent regulation of adenosinemonosphosphate-dependent kinase (AMPK) by insulin.pdf. FEBS J. 2012;
16. Pezze PD, Ruf S, Sonntag AG, Langelaar-Makkinje M, Hall P, Heberle AM, et al.

A systems study reveals concurrent activation of AMPK and mTOR by amino acids. Nat Commun. 2016;7:1–19.
17. Fujita KA, Toyoshima Y, Uda S, Ozaki YI, Kubota H, Kuroda S. Decoupling of receptor and downstream signals in the Akt pathway by its low-pass filter characteristics. Sci Signal. 2010;3(132):1–11.
18. Rahman A, Haugh JM, Toker A. Kinetic Modeling and Analysis of the Akt/Mechanistic Target of Rapamycin Complex 1 (mTORC1) Signaling Axis Reveals Cooperative, Feedforward Regulation. J Biol Chem. 2017;292(7):2866–72.
19. Krishnan P, Vinod U, Viswanath K. Quantification of the effect of amino acids on an integrated mTOR and insulin signaling pathway w. Mol Biosyst. 2009;5:1163–73.
20. Faratian D, Goltsov A, Lebedeva G, Sorokin A, Moodie S, Mullen P, et al. Systems Biology Reveals New Strategies for Personalizing Cancer Medicine and Confirms the Role of PTEN in Resistance to Trastuzumab. Cancer Res. 2009;69(16):6713–21.

Appendix B Supporting Information for Chapter 3

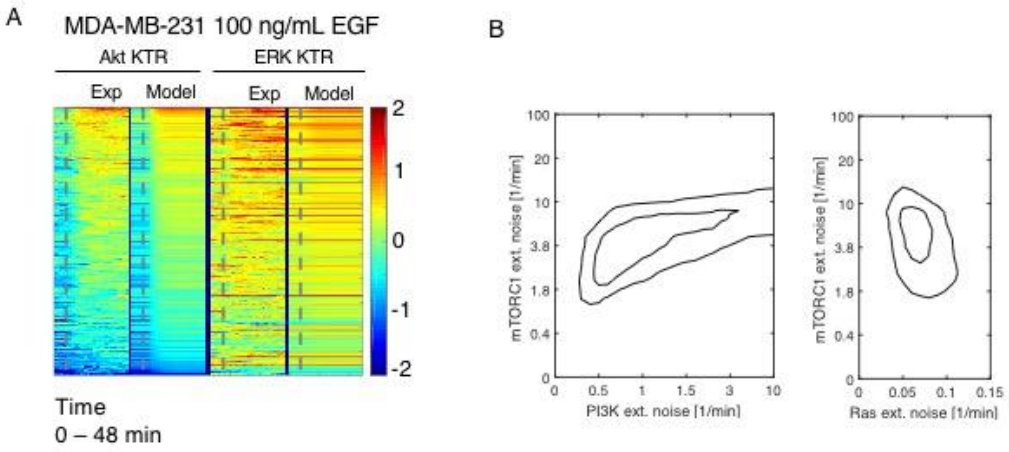

Figure B1 The computational model combined with KTR imaging experiments allows us to calculate the pre-existing states in MDA-MB-231 cells

(A) MDA-MB-231 cells from the KTR imaging experiments stimulated with 100 ng/mL EGF match model-predicted paired Akt and ERK dynamics. (B) These cells match in a region of the model with moderate PI3K, Ras, and mTORC1 extrinsic noise values, distinguishing them from the pre-existing states of SUM 159 cells.

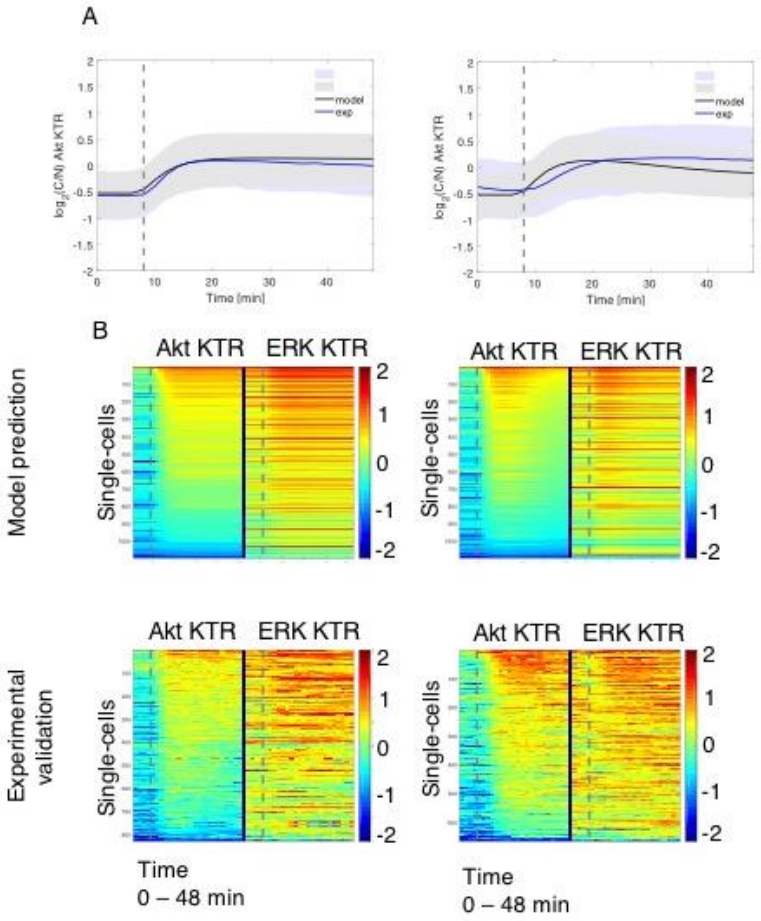

Figure B2 The CSM predicts MDA-MB-231 cell Akt and ERK responses to EGF and CXCL12 at new doses given the calculated pre-existing states of these cells

(A) The median, 10^{th}, and 90^{th} percentile of the $\log_2$(C/N) of Akt dynamics predicted from the model for these cells stimulated with 300 ng/mL EGF (left) and 30 ng/mL CXCL12 (right) match experimental validation. (B) Single-cell time tracks of the predicted (top) and experimental (bottom) Akt and ERK dynamics illustrate that the model captures the entire continuum of responses to EGF (left) and CXCL12 (right) stimulation seen in experiments.

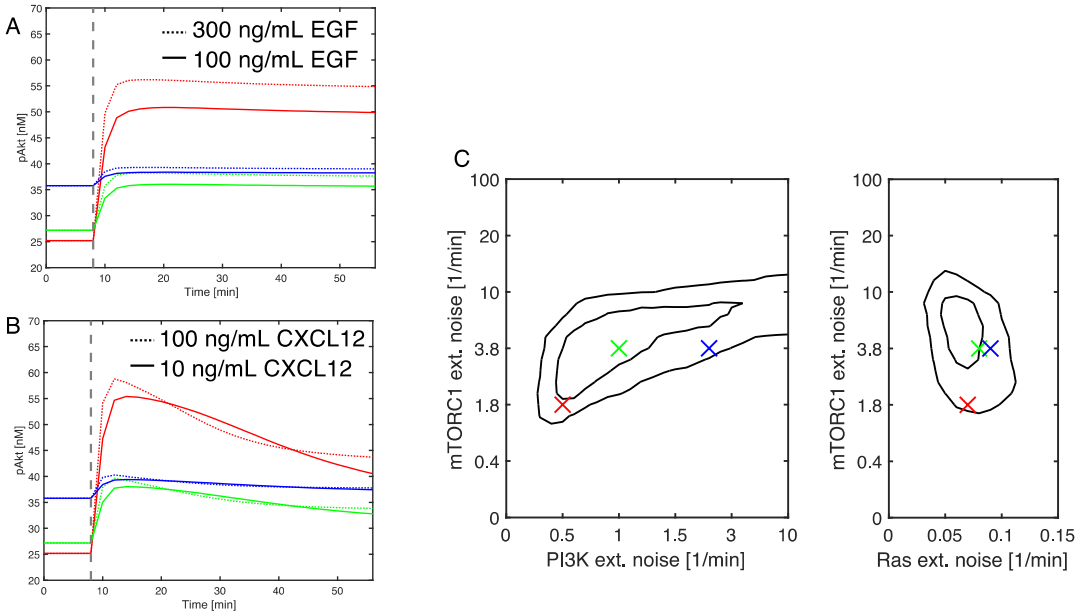

Figure B3 The model predicts Akt concentrations following doses of EGFR or CXCR4 stimulation

(A) MDA-MB-231 cells stimulated with 100 ng/mL (solid line) or 300 ng/mL (dotted line) EGF show heterogeneous predicted Akt responses. Line colors correspond to those in B and C. (B) MDA-MB-231 cells stimulated with 10 ng/mL (solid line) or 100 ng/mL (dotted line) CXCL12 show heterogeneous predicted Akt responses. Line colors correspond to those in A and C. (C). Contour map illustrating the pre-existing states occupied by MDA-MB-231 cells with colored x's indicating the pre-existing states shown in A and B. The contours represent the 2D projected occupancy map of the experimental cells after being matched in the 3D model library space. The outer and inner contours represent 90 and 50 percent of experimental cells, respectively.

Table B1 CSM species descriptions and initial conditions

Species	Description	Initial Condition (nM)	Ref.
R4	Surface CXCR4	850	(1)
L12	Extracellular CXCL12	0	--
C4	Surface CXCL12-CXCR4 complex	0	--
R4p	Phosphorylated surface CXCR4	0	--
C4p	Phosphorylated surface CXCL12-CXCR4 complex	0	--
R4pB	Phosphorylated surface CXCR4 bound to β-arrestin	0	--
C4pB	Phosphorylated surface CXCL12-CXCR4 complex bound to β -arrestin	0	--
R4i	Internalized CXCR4	0	--
C4Bi	Internalized CXCL12-CXCR4 complex bound to B-arrestin	0	--
C4Bii	Internalized CXCL12-CXCR4 complex	0	--
EGFR	Surface EGFR	$1x10^4$	(2)
EGF	Extracellular EGF	0	--
EGF-EGFR	Surface EGF-EGFR complex	0	--
EGF-EGFRi	Internalized EGF-EGFRi complex	0	--
EGFRi	Internalized EGFR	0	--
GDP	Inactive G-protein	170	(3)
GTP	Active G-protein	0	--
iPI3K	Inactive PI3K	200	(4)
PI3K	Active PI3K	0	--
PIP_2	Phosphatidylinositol biphosphate (inactive)	1000	(5)
PIP_3	Phosphatidylinositol triphosphate (active)	0	--
iPDK1	Inactive PDK1	500	(6)
PDK1	Active PDK1	0	--
Akt	Inactive Akt	1000	(6)
$pAkt_{T308}$	Akt phosphorylated only at the Threonine 308 site (kinase domain)	0	--
$pAkt_{S473}$	Akt phosphorylated only at the Serine 473 site (regulatory domain)	0	--
ppAkt	Fully activated Akt phosphorylated at both the T308 and S473 site	0	--
mTOR	Uncomplexed mTOR	800	(7)
mTORC1	Active mTORC1	0	--
mTORC2	Active mTORC2	0	--
iRas	Inactive Ras	3000	(6)
Ras	Active Ras	0	--
iRaf	Inactive Raf	1000	(6)
Raf	Active Raf	0	--

ERK	Inactive ERK	850	(8)
pERK	Active ERK	0	--
$r_{cu,Akt}$	Cytoplasmic unphosphorylated Akt KTR	0	(9)
$r_{nu,Akt}$	Nuclear unphosphorylated Akt KTR	200	(9)
$r_{cp,Akt}$	Cytoplasmic phosphorylated Akt KTR	200	(9)
$r_{np,Akt}$	Nuclear phosphorylated Akt KTR	0	(9)
$r_{cu,ERK}$	Cytoplasmic unphosphorylated ERK KTR	0	(9)
$r_{nu,ERK}$	Nuclear unphosphorylated ERK KTR	200	(9)
$r_{cp,ERK}$	Cytoplasmic phosphorylated ERK KTR	200	(9)
$r_{np,ERK}$	Nuclear phosphorylated ERK KTR	0	(9)

Table B2 CSM rate equations

Equation No.	Reaction *reactant → product; modifiers*	Reaction Rate
(1)	R4+L12↔C4	$v_{bLR4}=k_{f,L12,R4}*(R4*L12-K_{D,L12,R4}*C4)$
(2)	R4pB+L12↔C4pB	$v_{bLR4pB}= k_{f,L12,R4}*(R4pB*L12-K_{D,L12,R4pB}*C4pB)$
(3)	R4p+L12↔C4p	$v_{bLR4ph}=k_{f,L12,R4}*(R4p*L12-K_{D,L12,R4pB}*C4p)$
(4)	R4↔R4p	$v_{R4,phos}=k_{f,R4phos}*R4-k_{r,R4phos}*R4p$
(5)	C4↔C4p	$v_{C4phos}=k_{f,C4phos}*C4-k_{r,C4phos}*C4p$
(6)	R4p↔R4pB	$v_{bBR4ph}=k_{f,B,R4}*(R4p-K_{D,B,R4}*R4pB)$
(7)	C4p↔C4pB	$v_{bBC4ph}=k_{f,B,R4}*(C4p-K_{D,B,C4}*C4pB)$
(8)	C4pB→C4Bi	$v_{iC4pB}=k_{eC4pB}*C4pB$
(9)	C4Bi→C4Bii	$v_{off,C4Bi}=k_{off,B,R4}*C4Bi$
(10)	C4Bii→∅	$v_{deg,C4Bii}=k_{deg,C4Bii}*C4Bii$
(11)	R4pB→R4i	$v_{iR4pB}=k_{eR4pB}*R4pB$
(12)	R4i→R4	$v_{recy,R4Bi}=k_{rec,R4Bi}*R4Bi$
(13)	GDP→GTP	$v_{actGC4}=k_{C4actG}*C4*GDP$
(14)	GDP→GTP	$v_{actGC4p}=k_{C4actG}*C4p*GDP$
(15)	GDP→GTP	$v_{actGC4p}=k_{basalActG}*GDP$
(16)	GTP→GDP	$v_{deactG}=k_{deactG\beta\gamma}*GTP$
(17)	iPI3K→PI3K; GTP	$v_{actPI3K}=k_{actPI3K}*G_{\beta\gamma}*\frac{iPI3K}{K_{M,actPI3K}+iPI3K}$
(18)	iPI3K→PI3K	$v_{extActPI3K}=k_{PI3K}*iPI3K$
(19)	PI3K→iPI3K	$v_{deactPI3K}=k_{deactPI3K}*PI3K$
(20)	PIP_2→PIP_3; PI3K	$v_{actPIP3}=k_{actPIP3}*PI3K*\frac{PIP_2}{K_{M,actPIP3}+PIP_2}$

(21)	$PIP_3 \rightarrow PIP_2$	$v_{deactPIP3} = k_{deactPIP3} * PIP_3$
(22)	$iPDK1 \rightarrow PDK1$; PIP_3	$v_{actPDK1} = k_{actPDK1} * PIP_3 * \frac{iPDK1}{K_{M,actPDK1} + iPDK1}$
(23)	$PDK1 \rightarrow iPDK1$	$v_{deactPDK1} = k_{deactPDK1} * PDK1$
(24)	$Akt \rightarrow pAkt_{T308}$; PDK1	$v_{Akt \rightarrow pAkt_{T308}} = k_{actAktT308} * PDK1 * \frac{Akt}{K_{M,actAktT308} + Akt}$
(25)	$pAkt_{S473} \rightarrow ppAkt$; PDK1	$v_{pAkt_{S473} \rightarrow ppAkt} = k_{actAktT308} * PDK1 * \frac{pAkt_{S473}}{K_{M,actAktT308} + pAkt}$
(26)	$Akt \rightarrow pAkt_{S473}$; mTORC2	$v_{Akt \rightarrow pAkt_{S473}} = k_{actAktS473} * mTORC2 * \frac{Akt}{K_{M,actAktS473} + Ak}$
(27)	$pAkt_{T308} \rightarrow ppAkt$; mTORC2	$v_{pAkt_{T308} \rightarrow ppAkt} = k_{actAktS473} * mTORC2 * \frac{pAkt_{T308}}{K_{M,actAktS473} + pAkt_{T308}}$
(28)	$pAkt_{T308} \rightarrow Akt$	$v_{pAkt_{T308} \rightarrow Akt} = k_{deactAktT308} * pAkt_{T308}$
(29)	$pAkt_{S473} \rightarrow Akt$	$v_{pAkt_{S473} \rightarrow Akt} = k_{deactAktS473} * pAkt_{S473}$
(30)	$ppAkt \rightarrow pAkt_{T308}$	$v_{ppAkt \rightarrow pAkt_{T308}} = k_{deactAktS473} * ppAkt$
(31)	$ppAkt \rightarrow pAkt_{S473}$	$v_{ppAkt \rightarrow pAkt_{S473}} = k_{deactAktT308} * ppAkt$
(32)	$mTOR \rightarrow mTORC2$; PIP_3,mTORC1	$v_{actmTORC2} = k_{actmTORC2} * PIP_3 * \frac{mTOR}{K_{M,actmTORC2} + mTOR\left(1 + \frac{mTORC1}{K_{I,inhibmTORC2}}\right)}$
(33)	$mTORC2 \rightarrow mTOR$	$v_{deactmTORC2} = k_{deactmTORC2} * mTORC2$
(34)	$mTOR \rightarrow mTORC1$	$v_{extActmTORC1} = k_{mTORC1} * mTOR$
(35)	$mTOR \rightarrow mTORC1$; ppAkt	$v_{actmTORC1,Akt} = k_{actmTORC1,Akt} * ppAkt * \frac{mTOI}{K_{M,actmTORC1,A}}$
(36)	$mTOR \rightarrow mTORC1$; pERK	$v_{actmTORC1,ERK} = k_{actmTORC1,ERK} * pERK * \frac{mT}{K_{M,actmTORC}}$

(37) mTORC1→mTOR $v_{deactmTORC1}=k_{deactmTORC1}*mTORC1$

(38) iRas→Ras; GTP, mTORC1 $v_{actRas}=k_{actRas}*GTP*\frac{iRas}{K_{M,actRas}+iRas\left(1+\frac{mTORC1}{K_{I,inhib,Ras}}\right.}$

(39) iRas→Ras $v_{extActRas}=k_{Ras}*iRas$

(40) Ras→iRas $v_{deactRas}=k_{deactRas}*Ras$

(41) iRaf→Raf; Ras $v_{actRaf}=k_{actRaf}*Ras*\frac{iRaf}{K_{M,actRaf}+iRaf}$

(42) iRaf→Raf $v_{constActRaf}=k_{constActRaf}*iRaf$

(43) Raf→iRaf; ppAkt $v_{inhibRaf}=k_{inhibRaf}*ppAkt*\frac{Raf}{K_{M,inhibRaf}+Raf}$

(44) Raf→iRaf $v_{deactRaf}=k_{deactRaf}*Raf$

(45) ERK→pERK; Raf $v_{actERK}=k_{actERK}*Raf*\frac{ERK}{K_{M,actERK}+ERK}$

(46) pERK→ERK $v_{deactERK}=k_{deactERK}*pERK$

(47) $r_{cu,Akt}\rightarrow r_{cp,Akt}$; ppAkt $v_{phos,cyto,AktKTR}=ppAkt*k_{cat}*\frac{r_{cu,Akt}}{r_{cu,Akt}+K_m}$

(48) $r_{nu,Akt}\rightarrow r_{np,Akt}$; ppAkt $v_{phos,nuc,AktKTR}=ppAkt*k_{cat}*\frac{r_{nu,Akt}}{r_{nu,Akt}+K_m}$

(49) $r_{cu,ERK}\rightarrow r_{cp,ERK}$; pERK $v_{phos,cyto,ERKKTR}=pERK*k_{cat}*\frac{r_{cu,ERK}}{r_{cu,ERK}+K_m}$

(50) $r_{nu,ERK}\rightarrow r_{np,ERK}$; pERK $v_{phos,nuc,ERKKTR}=pERK*k_{cat}*\frac{r_{nu,ERK}}{r_{nu,ERK}+K_m}$

(51) $r_{cp,Akt}\rightarrow r_{cu,Akt}$ $v_{dephos,cyto,AktKTR}=k_{dc}*\frac{r_{cp,Akt}}{r_{cp,Akt}+K_{md}}$

(52) $r_{np,Akt}\rightarrow r_{nu,Akt}$ $v_{dephos,nuc,AktKTR}=k_{dn}*\frac{r_{np,Akt}}{r_{np,Akt}+K_{md}}$

(53) $r_{cp,ERK}\rightarrow r_{cu,ERK}$ $v_{dephos,cyto,ERKKTR}=k_{dc}*\frac{r_{cp,ERK}}{r_{cp,ERK}+K_{md}}$

(54) $r_{np,ERK} \rightarrow r_{nu,ERK}$ $v_{dephos,nuc,ERKKTR} = k_{dn} * \frac{r_{np,ERK}}{r_{np,ERK} + K_{md}}$

(55) $r_{cp,Akt} \rightarrow r_{np,Akt}$ $v_{phos,import,AktKTR} = k_{ip} * r_{cp,Akt}$

(56) $r_{cu,Akt} \rightarrow r_{nu,Akt}$ $v_{unphos,import,AktKTR} = k_{iu} * r_{cu,Akt}$

(57) $r_{np,Akt} \rightarrow r_{cp,Akt}$ $v_{phos,export,AktKTR} = k_{ep} * r_{np,Akt}$

(58) $r_{nu,Akt} \rightarrow r_{cu,Akt}$ $v_{unphos,export,AktKTR} = k_{eu} * r_{nu,Akt}$

(59) $r_{cp,ERK} \rightarrow r_{np,ERK}$ $v_{phos,import,ERKKTR} = k_{ip} * r_{cp,ERK}$

(60) $r_{cu,ERK} \rightarrow r_{nu,ERK}$ $v_{unphos,import,ERKKTR} = k_{iu} * r_{cu,ERK}$

(61) $r_{np,ERK} \rightarrow r_{cp,ERK}$ $v_{phos,export,ERKKTR} = k_{ep} * r_{np,ERK}$

(62) $r_{nu,ERK} \rightarrow r_{cu,ERK}$ $v_{unphos,export,ERKKTR} = k_{eu} * r_{nu,ERK}$

(63) EGF+EGFR↔EGF-EGFR $v_{b,EGF,EGFR} = k_{f,EGF,EGFR} * (EGF * EGFR - K_{D,EGF,EGFR} * EGF\text{-}EGFR)$

(64) EGFR→EGFRi $v_{i,EGFR} = k_{e,EGFR} * EGFR$

(65) EGFRi→EGFR $v_{recy,EGFRi} = k_{rec,EGFR} * EGFRi$

(66) EGF-EGFR→EGF-EGFRi $v_{i,EGF\text{-}EGFR} = k_{e,EGF\text{-}EGFR} * EGF\text{-}EGFR$

(67) EGF-EGFRi→EGF-EGFR $v_{recy,EGF\text{-}EGFRi} = k_{rec,EGF\text{-}EGFRi} * EGF\text{-}EGFRi$

(68) EGF-EGFRi→∅ $v_{deg,EGF\text{-}EGFRi} = k_{deg,EGF\text{-}EGFRi} * EGF\text{-}EGFRi$

(69) iPI3K→PI3K; EGF-EGFR,I $v_{actPI3K,EGF} = k_{actPI3K,EGF} * (EGF\text{-}EGFR + EGF\text{-}EGFRi) * PI3K$

(70) iRas→Ras; EGF-EGFR,E($v_{actRas,EGF} = k_{actRas,EGF} * (EGF\text{-}EGFR + EGF\text{-}EGFRi)^{2} * \frac{iRas}{K_{M,actRas,EGF} + iRas\left(1 + \frac{mTORC1}{K_{I,inhibRas,EGFR}}\right)}$

Table B3 CSM differential equations

Receptor dynamics	$dR4/dt$	$= -v_{bLR4} - v_{R4,phos} + v_{recy,R4Bi}$
	$dC4/dt$	$= v_{bLR4} - v_{C4,phos}$
	$dR4p/dt$	$= v_{R4,phos} - v_{bLR4ph} - v_{bBR4ph}$
	$dC4p/dt$	$= v_{C4,phos} + v_{bLR4ph} - v_{bBC4ph}$
	$dL12/dt$	$= (-v_{bLR4} - v_{bLR4pB} - v_{bLR4ph} - v_{bLR4B}) * N_C/(V_{cell}/V_{media})$
	$dR4pB/dt$	$= -v_{bLR4pB} + v_{bBR4ph} - v_{iR4pB}$
	$dC4pB/dt$	$= v_{bLR4pB} + v_{bBC4ph} - v_{i,C4pB}$
	$dR4i/dt$	$= v_{iR4pB} - v_{recy,R4Bi}$
	$dC4Bi/dt$	$= v_{iC4pB} - v_{off,C4Bi}$
	$dC4Bii/dt$	$= v_{off,C4Bi} - v_{deg,C4Bii}$
	$dEGFR/dt$	$= -v_{b,EGF\text{-}EGFR} - v_{i,EGFR} + v_{recy,EGFRi}$
	$dEGF\text{-}EGFR/dt$	$= v_{b,EGF\text{-}EGFR} - v_{i,EGF\text{-}EGFR} + v_{recy,EGF\text{-}EGFRi}$
	$dEGF/dt$	$= -v_{b,EGF\text{-}EGFR} * N_C/(V_{cell}/V_{media})$
	$dEGFRi/dt$	$= v_{i,EGFR} - v_{recy,EGFRi}$
	$dEGF\text{-}EGFRi/dt$	$= v_{i,EGF\text{-}EGFR} - v_{recy,EGF\text{-}EGFRi} - v_{deg,EGF\text{-}EGFRi}$
Signaling dynamics	$dGTP/dt$	$= v_{actGC4} + v_{actGC4p} - v_{deactG}$
	$dPI3K/dt$	$= v_{actPI3K} + v_{basalActPI3K} - v_{deactPI3K} - v_{actPI3K,EGF}$
	$dPIP_3/dt$	$= v_{actPIP3} - v_{deactPIP3} - v_{actPDK1} + v_{deactPDK1}$
	$dPDK1/dt$	$= v_{actPDK1} - v_{deactPDK1}$
	$dmTORC1/dt$	$= v_{actmTORC1,Akt} + v_{actmTORC1,ERK} - v_{deactmTORC1}$
	$dmTORC2/dt$	$= v_{actmTORC2} - v_{deactmTORC2}$
	$dRas/dt$	$= v_{actRas} + v_{constActRas} - v_{inhibRas} - v_{deactRas} - v_{actRas,EGF}$
	$dRaf/dt$	$= v_{actRaf} + v_{constActRaf} - v_{inhibRaf} - v_{deactRaf}$
	$dpERK/dt$	$= v_{actERK} - v_{deactERK}$
	$dAkt/dt$	$= -v_{Akt\rightarrow pAkt_{T308}} - v_{Akt\rightarrow pAkt_{S473}} + v_{pAkt_{T308}\rightarrow Akt} + v_{pAkt_{S473}\rightarrow Akt}$
	$dpAkt_{T308}/dt$	$= v_{Akt\rightarrow pAkt_{T308}} - v_{pAkt_{T308}\rightarrow Akt} - v_{pAkt_{T308}\rightarrow ppAkt} + v_{ppAkt\rightarrow pAkt_{T308}}$
	$dpAkt_{S473}/dt$	$= -v_{pAkt_{S473}\rightarrow ppAkt} + v_{Akt\rightarrow pAkt_{S473}} + v_{ppAkt\rightarrow pAkt_{S473}} - v_{pAkt_{S473}\rightarrow Akt}$
	$dppAkt/dt$	$= v_{pAkt_{S473}\rightarrow ppAkt} + v_{pAkt_{T308}\rightarrow ppAkt} - v_{ppAkt\rightarrow pAkt_{S473}} - v_{ppAkt\rightarrow pAkt_{T308}}$
Reporter dynamics	$dr_{cu,Akt}/dt$	$= -v_{phos,cyto,Akt} + v_{dephos,cyto,Akt} - v_{unphos,import,Akt} + v_{unphos,export,Akt}$
	$dr_{nu,Akt}/dt$	$= -v_{phos,nuc,Akt} + v_{dephos,nuc,Akt} + k_v*(v_{unphos,import,Akt} - v_{unphos,export,Akt})$
	$dr_{cp,Akt}/dt$	$= v_{phos,cyto,Akt} - v_{dephos,cyto,Akt} - v_{phos,import,Akt} + v_{phos,export,Akt}$
	$dr_{np,Akt}/dt$	$= v_{phos,nuc,Akt} - v_{dephos,nuc,Akt} + k_v*(v_{phos,import,Akt} - v_{phos,export,Akt})$
	$dr_{cu,ERK}/dt$	$= -v_{phos,cyto,ERK} + v_{dephos,cyto,ERK} - v_{unphos,import,ERK} + v_{unphos,export,ERK}$
	$dr_{nu,ERK}/dt$	$= -v_{phos,nuc,ERK} + v_{dephos,nuc,ERK} + k_v*(v_{unphos,import,ERK} - v_{unphos,export,ERK})$
	$dr_{cp,ERK}/dt$	$= v_{phos,cyto,ERK} - v_{dephos,cyto,ERK} - v_{phos,import,ERK} + v_{phos,export,ERK}$
	$dr_{np,ERK}/dt$	$= v_{phos,nuc,ERK} - v_{dephos,nuc,ERK} + k_v*(v_{phos,import,ERK} - v_{phos,export,ERK})$

We assumed conservation of mass for all signaling reactions. The differential equation

for the inactive form of each species in the signaling dynamics module is equal and opposite of the differential equation for the active form, ex: diPI3K/dt = -dPI3K/dt.

Table B4 CSM parameter values

Name	Description of event	Value	Unit	Ref
$k_{f,B,R4}$	β-arrestin binding to R4	2.04	$nM^{-1}\,min^{-1}$	(1,10,11)
$K_{D,B,R4}$	Dissociation of β-arrestin from R4	13.3	nM	(1,10,11)
$K_{D,B,C4}$	Dissociation of β-arrestin from C4	6.49×10^{-2}	nM	(1,10,11)
$k_{f,L12,R4}$	L12-R4 binding	8.79×10^{-2}	$nM^{-1}\,min^{-1}$	(1,10,11)
$K_{D,L12,R4}$	Dissociation of L12-R4	42.9	nM	(1,10,11)
$k_{e,R4pB}$	Endocytosis of phosphorylated R4	8.07×10^{-2}	min^{-1}	(1,10,11)
$k_{e,C4pB}$	Endocytosis of phosphorylated C4	0.169	min^{-1}	(1,10,11)
$k_{off,B,R4}$	β-arrestin removal from C4Bi	4.21×10^{-2}	min^{-1}	(1,10,11)
$k_{recy,R4Bi}$	Recycling of R4Bi to cell surface	3.64×10^{-3}	min^{-1}	(1,10,11)
$k_{deg,C4Bii}$	Degradation of internalized L12-C4 complex	9.15×10^{-3}	min^{-1}	(1,10,11)
$k_{f,C4phos}$	C4 phosphorylation	0.409	min^{-1}	(12)
$k_{f,R4phos}$	R4 phosphorylation	6.09×10^{-2}	min^{-1}	(12)
$k_{r,C4phos}$	C4 dephosphorylation	5.85×10^{-3}	min^{-1}	(12)
$k_{r,R4phos}$	R4 dephosphorylation	8.09×10^{-4}	min^{-1}	(12)
$k_{f,EGF,EGFR}$	EGF binding to EGFR**	2.05	nM^{-1} min^{-1}	(2)
$K_{D,EGF,EGFR}$	Dissociation of EGF from EGFR***	0.01	nM	(2)
$k_{e,EGFR}$	Endocytosis of EGFR	6.6×10^{-2}	min^{-1}	(2)
$k_{rec,EGFRi}$	Recycling of EGFRi to cell surface	3.23×10^{-3}	min^{-1}	(2)
$k_{e,EGF\text{-}EGFRi}$	Endocytosis of EGF-EGFR complex	0.134	min^{-1}	(2)
$k_{rec,EGF\text{-}EGFRi}$	Recycling of EGF-EGFRi to cell surface	1.48×10^{-2}	min^{-1}	(2)
$k_{deg,EGF\text{-}EGFRi}$	Degradation of internalized EGF-EGFR complex	0.213	min^{-1}	(2)
k_{C4actG}	GTP activation	0.200	$nM^{-1}\,min^{-1}$	(12)
$k_{basalActG}$	Basal GTP activation	0.200	min^{-1}	(12)
k_{deactG}	GTP deactivation	4.67	min^{-1}	(12)
$k_{actPI3K}$	PI3K activation	5.00	min^{-1}	(13,14)
$K_{M,actPI3K}$	PI3K activation (Michaelis constant)	20.00	nM	(14)
$k_{actPI3K,EGF}$	PI3K activation by EGF	6.89×10^{-3}	$nM^{-1}\,min^{-1}$	^
$k_{deactPI3K}$	PI3K deactivation	6.00	min^{-1}	(4,15)
k_{PI3K}	PI3K activity external to CXCR4 signaling	0.30 – 5.30	min^{-1}	--
$k_{actPIP3}$	PIP_3 activation	2.00×10^{2}	min^{-1}	(5,13,14)
$K_{M,actPIP3}$	PIP_3 activation (Michaelis constant)	1.00×10^{2}	nM	(14)
$k_{deactPIP3}$	PIP_3 deactivation	10.0	min^{-1}	(14)
$k_{actPDK1}$	PDK1 activation	50.0	min^{-1}	(14)
$K_{M,actPDK1}$	PDK1 activation (Michaelis constant)	2.00×10^{2}	nM	^
$k_{deactPDK1}$	PDK1 deactivation	53.3	min^{-1}	(14)
$k_{actAktT308}$	Akt T308 activation (kinase domain)	2.00	min^{-1}	(14)
$K_{M,actAktT308}$	Akt T308 (Michaelis constant)	2.00×10^{2}	nM	(7)
$k_{actAktS473}$	Akt S473 activation (regulatory domain)	2.00	min^{-1}	(14,16)
$K_{M,actAktS473}$	Akt S473 (Michaelis constant)	2.00×10^{2}	nM	(7)

$k_{deactAktT308}$	Akt T308 deactivation	1.61	min^{-1}	(17,18)
$k_{deactAktS473}$	Akt S473 deactivation	3.00	min^{-1}	(17,18)
$k_{actmTORC1,ERK}$	mTORC1 activation by ERK	1.22	min^{-1}	^
$K_{M,actmTORC1,ERK}$	mTORC1 activation by ERK (Michaelis constant)	27.7	nM	^
$k_{actmTORC1,Akt}$	mTORC1 activation by Akt	3.39	min^{-1}	^
$K_{M,actmTORC1,Akt}$	mTORC1 activation by Akt (Michaelis constant)	23.4	nM	^
$k_{deactmTORC1}$	mTORC1 deactivation	41.6	min^{-1}	(19)
k_{mTORC1}	mTORC1 activity external to CXCR4 signaling	0 – 10.0	min^{-1}	--
$k_{actmTORC2}$	mTORC2 activation	0.60	min^{-1}	(16)
$K_{M,actmTORC2}$	mTORC2 activation (Michaelis constant)	26.2	nM	^
$K_{I,inhibmTORC2}$	mTORC2 inhibitory constant	20.3	nM	^
$k_{deactmTORC2}$	mTORC2 deactivation	1.13	min^{-1}	(16)
k_{actRas}	Ras activation	5.00	min^{-1}	(20)
$K_{M,actRas}$	Ras activation (Michaelis constant)	2.00×10^{2}	nM	(5)
$k_{actRas,EGF}$	Ras activation by EGF	1.44×10^{3}	min^{-1}	^
$K_{M,actRas,EGF}$	Ras activation by EGF (Michaelis constant)	443	nM	^
k_{Ras}	Ras activity external to CXCR4 signaling	0 – 0.300	min^{-1}	--
$k_{deactRas}$	Ras deactivation	8.49	min^{-1}	(5)
$K_{I,inhibRas}$	Ras inhibitory constant	14	nM	^
$K_{I,inhibRas,EGF}$	Ras inhibitory constant for EGF	0.011	nM	^
k_{actRaf}	Raf activation	2.00	min^{-1}	(14)
$K_{M,actRaf}$	Raf activation (Michaelis constant)	1.00×10^{3}	nM	(5)
$k_{constActRaf}$	Raf constitutive activation due to mutation*	0.005	min^{-1}	^
$k_{inhibRaf}$	Raf inhibition	0.1	min^{-1}	(13)
$K_{M,inhibRaf}$	Raf inhibition (Michaelis constant)	50.0	nM	(13)
k_{actERK}	ERK activation	4.00	min^{-1}	(14)
$K_{M,actERK}$	ERK activation (Michaelis constant)	24.6	nM	(5)
$k_{deactERK}$	ERK deactivation	3.20	min^{-1}	(5)
k_{cat}	Reporter phosphorylation	20.0	min^{-1}	(9)
K_m	Reporter phosphorylation (Michaelis constant)	3.00×10^{3}	nM	(9)
k_{dc}	Reporter maximum dephosphorylation in cytoplasm	30.0	nM min^{-1}	(9)
K_{md}	Reporter dephosphorylation (Michaelis constant)	1.00×10^{2}	nM	(9)
k_{iu}	Unphosphorylated reporter import	0.3	min^{-1}	(9)
k_{eu}	Unphosphorylated reporter export	5.00×10^{-2}	min^{-1}	(9)
k_{dn}	Reporter maximum dephosphorylation in nucleus	30.0	nM min^{-1}	(9)
k_{ip}	Phosphorylated reporter import	5×10^{-2}	min^{-1}	(9)
k_{ep}	Phosphorylated reporter export	0.500	min^{-1}	(9)
k_v	Ratio of cytosolic volume to nuclear	4	unitless	(9)

	volume			
N_C	Number of cells per imaging experiment	$2x10^5$	unitless	--

We assumed that all biochemical reactions inside cells are governed by biophysical rate constants and do not vary from cell-to-cell, nor from cell line to cell line. The only sources of variability in the CSM are the three external activation parameters for PI3K, Ras, and mTORC1, highlighted below. Parameters include rate constants, equilibrium dissociation constants, and Michaelis constants.

* For MDA-MB-231 cells. For SUM-159 and Vari-068 cells, this parameter is 0.
** For SUM 159 cells. For MDA-MB-231 cells, this parameter is 6.3×10^{-2}.
*** For SUM 159 cells. For MDA-MB-231 cells, this parameter is 50.
^ Estimated

Table B5 CSM parameters for modeling kinase inhibition

Conditioning treatment	Altered Parameter(s)	Baseline	Inhibition value
PI3K inhibitor	$k_{actPIP3}$	200 min^{-1}	20 min^{-1}

Appendix B References

1. Chang SL, Cavnar SP, Takayama S, Luker GD, Linderman JJ. Cell, Isoform, and Environment Factors Shape Gradients and Modulate Chemotaxis. PLoS One. 2015;10(4):e0123450.
2. Hendriks BS, Opresko LK, Wiley HS, Lauffenburger D. Coregulation of Epidermal Growth Factor Receptor/Human Epidermal Growth Factor Receptor 2 (HER2) Levels and Locations: Quantitative Analysis of HER2 Overexpression Effects. Cancer Res. 2003;63:1130–7.
3. Fallahi-Sichani M, Linderman JJ. Lipid raft-mediated regulation of G-protein coupled receptor signaling by ligands which influence receptor dimerization: A computational study. PLoS One. 2009;4(8).
4. Tan WH, Popel AS, Mac Gabhann F. Computational Model of Gab1/2-Dependent VEGFR2 Pathway to Akt Activation. PLoS One. 2013;8(6):1–17.
5. Jain P, Bhalla US. Signaling logic of activity-triggered dendritic protein synthesis: An mTOR gate but not a feedback switch. PLoS Comput Biol. 2009;5(2).
6. Adlung L, Kar S, Wagner M, She B, Chakraborty S, Bao J, et al. Protein abundance of AKT and ERK pathway components governs cell type-specific regulation of proliferation. Mol Syst Biol. 2017;13(1):904.
7. Borisov N, Aksamitiene E, Kiyatkin A, Legewie S, Berkhout J, Maiwald T, et al. Systems-level interactions between insulin-EGF networks amplify mitogenic signaling. Mol Syst Biol. 2009;5(256):1–15.
8. Iwamoto K, Shindo Y, Takahashi K. Modeling Cellular Noise Underlying Heterogeneous Cell Responses in the Epidermal Growth Factor Signaling Pathway. PLoS Comput Biol. 2016;12(11):1–18.
9. Regot S, Hughey JJ, Bajar BT, Carrasco S, Covert MW. High-sensitivity measurements of multiple kinase activities in live single cells. Cell. 2014;157(7):1724–34.
10. Coggins NL, Trakimas D, Chang SL, Ehrlich A, Ray P, Luker KE, et al. CXCR7 Controls Competition for Recruitment of β-Arrestin 2 in Cells Expressing Both CXCR4 and CXCR7. PLoS One. 2014;9(6):e98328.
11. Spinosa PC, Luker KE, Luker GD, Linderman JJ. The CXCL12/CXCR7 signaling axis, isoforms, circadian rhythms, and tumor cellular composition dictate gradients in tissue. PLoS One. 2017;12(11).
12. Chang SL. Mechanistic and statistical models to understand CXCL12/CXCR4/CXCR7 in breast cancer. 2015.
13. Hatakeyama M, Kimura S, Naka T, Kawasaki T, Yumoto N, Ichikawa M, et al. A computational model on the modulation of mitogen-activated protein kinase (MAPK) and Akt pathways in heregulin-induced ErbB signalling. Biochem J. 2003;373(2):451–63.
14. Koh G, Fern H, Teong C, Hsu D, Thiagarajan PS. A decompositional approach to parameter estimation in pathway modeling: a case study of the Akt and MAPK pathways and their crosstalk. Bioinformatics. 2006;22(14):271–80.
15. Sedaghat AR, Sherman A, Quon MJ. A mathematical model of metabolic insulin signaling pathways. AmJPhysiol EndocrinolMetab. 2002;283(5):E1084–101.
16. Sonntag A, Pezze Dalle P, Shanley DP TK. A modelling–experimental approach

reveals insulinreceptor substrate (IRS)-dependent regulation of adenosinemonosphosphate-dependent kinase (AMPK) by insulin.pdf. FEBS J. 2012;
17. Pezze PD, Ruf S, Sonntag AG, Langelaar-Makkinje M, Hall P, Heberle AM, et al. A systems study reveals concurrent activation of AMPK and mTOR by amino acids. Nat Commun. 2016;7:1–19.
18. Fujita KA, Toyoshima Y, Uda S, Ozaki YI, Kubota H, Kuroda S. Decoupling of receptor and downstream signals in the Akt pathway by its low-pass filter characteristics. Sci Signal. 2010;3(132):1–11.
19. Krishnan P, Vinod U, Viswanath K. Quantification of the effect of amino acids on an integrated mTOR and insulin signaling pathway w. Mol Biosyst. 2009;5:1163–73.
20. Faratian D, Goltsov A, Lebedeva G, Sorokin A, Moodie S, Mullen P, et al. Systems Biology Reveals New Strategies for Personalizing Cancer Medicine and Confirms the Role of PTEN in Resistance to Trastuzumab. Cancer Res. 2009;69(16):6713–21.

Appendix C Supporting Information for Chapter 4

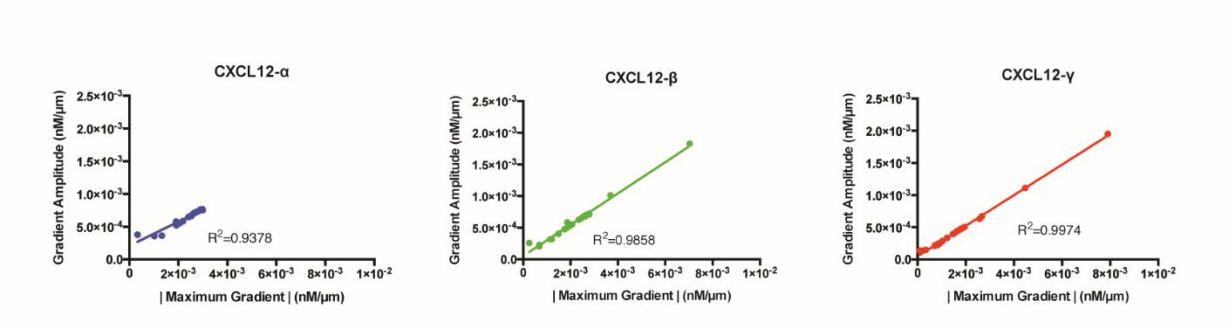

Figure C1 Correlation between the amplitude of the time-dependent blood-tissue gradient and the maximum observed gradient

We ran our computational model of the tumor microenvironment and varied the number of CXCL12-secreting and CXCR7+ cells in tissue using the same values as in Figure 4.5A. We found that the amplitude of the blood-tissue gradient curve over 24 hours correlated with the maximum gradient in a linear trend for all isoforms.

Table C1 Molecular species involved in CXCR7-CXCL12 binding and trafficking events

CXCR7 Species	Description
R_7 (#/cell)	Free cell-surface CXCR7
L_{12} (nM)	Free extracellular CXCL12
B_e (#/cell)	Free endogenous β-arrestin 2
R_{7Be} (#/cell)	R_7 bound to B_e
C_7 (#/cell)	R_7 bound to L_{12}
C_{7Be} (#/cell)	R_{7Be} bound to L_{12}
R_{7Bei} (#/cell)	Intracellular R_{7Be}
C_{7Bei} (#/cell)	Intracellular C_{7Be}
R_{7Beii} (#/cell)	R_{7Bei} after B_e dissociation
C_{7Beii} (#/cell)	C_{7Bei} after trafficking to late endosomes
C_{7Bpii} (#/cell)	C_{7Bpi} after trafficking to late endosomes
L_{12i} (#/cell)	Intracellular L_{12}

Table C2 Parameters describing CXCR7-CXCL12 binding and trafficking events

Parameter	Description	Value
$k_{f,L12,7}$ ($nM^{-1}s^{-1}$)	Forward rate constant of L_{12} binding R_7 /R_{7Be}	1.4 x10^{-3}
$k_{f,B,7}$ ((#/cell)$^{-1}s^{-1}$)	Forward rate constant of B_e binding R_7/C_7	1.4 x10^{-8}
$K_{D,R7,L12}$ (nM)	Equilibrium dissociation constant of L_{12} binding R_7	0.84
$K_{D,R7,B}$ (#/cell)	Equilibrium dissociation constant of B_e from R_7	2.3 x10^{6}
$K_{D,C7,B}$ (#/cell)	Equilibrium dissociation constant of B_e from C_7	6.5 x10^{5}
$k_{e,R7B}$ (s^{-1})	R_{7Be} internalization rate constant	3.9 x10^{-3}
$k_{e,C7B}$ (s^{-1})	C_{7Be} internalization rate constant	2.1 x10^{-3}
$k_{off,B,7}$ (s^{-1})	Dissociation rate constant of B_e from R_{7Bei}	2.5 x10^{-3}
$k_{e,C7Bi}$ (s^{-1})	Rate constant of trafficking of C_{7Bei} to late endosomes	5.5 x10^{-4}
$k_{rec,R7Bii}$ (s^{-1})	R_{7Beii} recycling rate constant	1.1 x10^{-3}
$k_{rec,C7Bii}$ (s^{-1})	C_{7Beii} recycling rate constant	2.8 x10^{-4}
$k_{deg,L12i}$ (s^{-1})	L_{12i} degradation rate constant	1.0 x10^{-4}

Table C3 Ordinary differential equations which govern CXCR7-CXCL12 binding and trafficking events.

Ligand binding to free receptors	$v_2 = k_{f,L_{12},7}([R_7][L_{12}] - K_{D,R_7,L_{12}}[C_7])$
Ligand binding to receptor-β-arrestin complexes	$v_4 = k_{f,L_{12},7}([R_{7B_e}][L_{12}] - K_{D,R_{7B},L_{12}}[C_{7B_e}])$
β-arrestin binding to free receptors	$v_8 = k_{f,B,7}([R_7][B_e] - K_{D,R_7,B}[R_{7B_e}])$
β-arrestin binding to ligand-bound receptors	$v_{12} = k_{f,B,7}([C_7][B_e] - K_{D,C_7,B}[C_{7B_e}])$
Internalization of cell surface receptor-β-arrestin complexes	$v_{16} = k_{e,R_{7B}}[R_{7B_e}]$
	$v_{20} = k_{e,C_{7B}}[C_{7B_e}]$
Dissociation of β-arrestin from internalized receptor-β-arrestin complexes	$v_{25} = k_{off,B,4}[C_{4B_ei}]$
Trafficking of internalized receptor-β-arrestin complexes to late endosomes	$v_{27} = k_{e,C_{7Bi}}[C_{7B_ei}]$
Recycling of internalized receptors	$v_{30} = k_{rec,R_{7Bii}}[R_{7B_eii}]$
	$v_{33} = k_{rec,C_{7Bii}}[C_{7B_eii}]$
Degradation of L_{12i}	$v_{37} = k_{deg,L_{12i}}[L_{12i}]$

$$\frac{d[R_7]}{dt} = -v_2 - v_8 - v_{10} + v_{30} + v_{32} + v_{33} + v_{34}$$

$$\frac{d[R_{7B_e}]}{dt} = +v_8 - v_4 - v_{16}$$

$$\frac{d[C_7]}{dt} = +v_2 - v_{12} - v_{14}$$

$$\frac{d[C_{7B_e}]}{dt} = +v_4 + v_{12} - v_{20}$$

$$\frac{d[R_{7B_ei}]}{dt} = +v_{16} - v_{23}$$

$$\frac{d[C_{7B_ei}]}{dt} = +v_{20} - v_{27}$$

$$\frac{d[C_{7B_eii}]}{dt} = +v_{27} - v_{33}$$

$$\sim \frac{d[L_{12}]}{dt} = (-v_2 - v_4 - v_6) \times \frac{10^9 \frac{nmol}{mol}}{V_{cell} \times N_{Av}}$$

$$\frac{d[L_{12i}]}{dt} = +v_{20} + v_{22} - v_{37}$$

$$\frac{d[B_e]}{dt} = -v_8 - v_{12} + v_{23} + v_{33}$$

$$\frac{d[R_{7B_eii}]}{dt} = +v_{23} - v_{30}$$

~ Units are nM/s
V_{cell} = volume of a cell, $1x10^{-12}$ L
N_{AV} = Avogadro's Number, $6.022x10^{23}$ mlcl / mol

Nomenclature, parameters, and equations shown in S1 Tables 3, 4, and 5 are taken from:

Chang SL, Cavnar SP, Takayama S, Luker GD, Linderman JJ. Cell, Isoform, and Environment Factors Shape Gradients and Modulate Chemotaxis. PLoS One. 2015;10(4):e0123450. doi:10.1371/journal.pone.0123450

Table C4 Model Parameters

Category	Symbol	Description	Value	Units	Ref.
Blood	p	CXCL12 permeability through blood vessel wall	4.08×10^{-5}	cm s^{-1}	(1)
	A	surface area of blood vessel bordering each endothelial compartment	100	μm^2	
	t_{max}	time of day of maximum CXCL12 blood concentration	9am, converted to military time		(2), this work
	t_{start}	time of day to start the simulation	arbitrary		
	$C_{CXCL12,max}$	maximum CXCL12 concentration in blood during circadian fluctuation	0.30 (CXCL12-α) 0.28 (CXCL12-β) 0.20 (CXCL12-γ)	nM	(3)
	$C_{CXCL12,min}$	minimum CXCL12 concentration in blood during circadian fluctuation	0.15 (CXCL12-α) 0.14 (CXCL12-β) 0.10 (CXCL12-γ)	nM	(2)
	f	frequency of circadian rhythm	24	h^{-1}	
Initialization thresholds	$BTIS_{threshold}$	blood-tissue interface stability threshold	1×10^{-5}		
	$GS_{threshold}$	gradient stability threshold	1×10^{-5}		
Isoform-specific parameters	K_D	binding affinity of CXCL12 for ECM	100 (CXCL12-α) 20 (CXCL12-β) 5 (CXCL12-γ)	nM	(4)
	S	baseline	20 (CXCL12-α)	# (cell	(4)

		CXCL12 secretion rate from cells (Setup 1)	15 (CXCL12-β) 5 (CXCL12-γ)	s)$^{-1}$	
	S_{max}	maximum CXCL12 secretion rate from cells during circadian fluctuation (Setup 2)	20 (CXCL12-α) 15 (CXCL12-β) 5 (CXCL12-γ)	# (cell s)$^{-1}$	(4)
	S_{min}	minimum CXCL12 secretion rate from cells during circadian fluctuation (Setup 2)	10 (CXCL12-α) 7.5 (CXCL12-β) 2.5 (CXCL12-γ)	# (cell s)$^{-1}$	(2)
Timesteps	t_d	timestep for diffusion	0.1	s	(4)
	t_m	timestep for receptor-ligand dynamics	0.01	s	(4)
Other	Φ	number of CXCL12 binding sites on ECM	$6.63x10^{4}$	# compartment^{-1}	(4)
	k_{deg}	Extracellular CXCL12 degradation rate	$2.05x10^{-5}$	s^{-1}	(4)
	D	CXCL12 diffusivity	$1.5x10^{-6}$	cm^2 s^{-1}	(5,6)
	k_{on}	on-rate of CXCL12 to ECM	0.001	s^{-1}	(4,7)

Table C5 Model Equations

Name	Equation	Symbols
Cell-derived CXCL12 gradient (G_C)	$G_C = \frac{C_{high} - C_{low}}{d_c}$	- C_{high} and C_{low} shown in Fig 1 - d_c = distance between clusters (100 μm)
Endothelial-tissue CXCL12 gradient (G_{E-T})	$G_{E-T} = \frac{C_{tissue} - C_{endo}}{d_{E-T}}$	- C_{tissue} and C_{endo} shown in Fig 1 - d_{E-T} = horizontal distance from endothelium to edge of simulation space (80 μm)
Blood-tissue CXCL12 gradient (G_{B-T})	$G_{B-T} = \frac{C_{tissue} - C_{blood}}{d_{B-T}}$	- C_{tissue} and C_{blood} shown in Fig 1 - d_{B-T} = horizontal distance from blood to edge of simulation space (90 μm)
Nonspecific CXCL12 binding to ECM	$\frac{dB}{dt} = k_{on}([CXCL12][\phi] - K_D[B])$	- B = CXCL12 bound to ECM - k_{on} = on-rate of CXCL12 to ECM - K_D = binding affinity of CXCL12 for ECM - Φ = empty sites on ECM

Appendix C References

1. Zervantonakis IK, Hughes-Alford SK, Charest JL, Condeelis JS, Gertler FB, Kamm RD. Three-dimensional microfluidic model for tumor cell intravasation and endothelial barrier function. Proc Natl Acad Sci. 2012;109(34):13515–13520. doi:10.1073/pnas.1210182109.
2. Méndez-Ferrer S, Lucas D, Battista M, Frenette PS. Haematopoietic stem cell release is regulated by circadian oscillations. Nature. 2008;452(7186):442-447. doi:10.1038/nature06685.
3. Łukaszewicz-Zając M, Mroczko B, Kozłowski M, Szmitkowski M. The Serum Concentrations of Chemokine CXCL12 and Its Specific Receptor CXCR4 in Patients with Esophageal Cancer. Dis Markers. 2016;2016:7963895. doi:10.1155/2016/7963895.
4. Chang SL, Cavnar SP, Takayama S, Luker GD, Linderman JJ. Cell, Isoform, and Environment Factors Shape Gradients and Modulate Chemotaxis. PLoS One. 2015;10(4):e0123450. doi:10.1371/journal.pone.0123450
5. Lin F, Butcher EC. T cell chemotaxis in a simple microfluidic device. Lab Chip. 2006;6(11):1462–1469. doi:10.1039/b607071j.
6. Torisawa YS, Mosadegh B, Bersano-Begey T, Steele JM, Luker KE, Luker GD, et al. Microfluidic platform for chemotaxis in gradients formed by CXCL12 source-sink cells. Integr Biol (Camb). 2010;2(11-12):680–686. doi:10.1039/c0ib00041h.
7. Laguri C, Sadir R, Rueda P, Baleux F, Gans P, Arenzana-Seisdedos F, et al. The novel CXCL12gamma isoform encodes an unstructured cationic domain which regulates bioactivity and interaction with both glycosaminoglycans and CXCR4. PLoS One. 2007;2(10):e1110. doi:10.1371/journal.pone.0001110.